Master's thesis

NTNU
Norwegian University of Science and Technology
Faculty of Natural Sciences
Department of Materials Science and Engineering

Inger Fygle

Production of Titanium alloys via aluminothermic reduction

Master's thesis in Materials Science and Engineering
Supervisor: Gabriella Tranell
July 2020

NTNU
Norwegian University of
Science and Technology

Inger Fygle

Production of Titanium alloys via aluminothermic reduction

Master's thesis in Materials Science and Engineering
Supervisor: Gabriella Tranell
July 2020

Norwegian University of Science and Technology
Faculty of Natural Sciences
Department of Materials Science and Engineering

NTNU
Kunnskap for en bedre verden

Preface

The following thesis is the result of a five-year master's program at The Norwegian University of Science and Technology at the Department of Materials Science and Engineering, written during the spring of 2020.

Firstly, I would like to thank my supervisor professor Gabriella Tranell for excellent help, motivation, and guidance along the way. In addition, the insights from Dr.Ing. Mertol Gökelma are appreciated.

I want to thank Dmitry Slizovskiy for helping me with equipment, slag making, and always being available. Further, I would like to thank Ivar Andre Ødegård for helping me with the vacuum induction furnace, Morten Peder Raanes for conducting EPMA analyses, Torill Sørløkk for performing the XRF analyses and Laurentius Tijhuis for performing the XRD analyses for me. Also, the help from Kai Erik Ekstrøm with FactSage calculations is highly appreciated.

Last but not least, I wish to thank my fellow student Safia Hassan, for all the support, conversations, discussions, and always being there, especially during this COVID-19 period. I could not have done this without you.

Abstract

Titanium metal has been produced and manufactured on a commercial scale since the early 1950s for its unique set of properties: (i) high strength-to-weight ratio, (ii) elevated melting point, and (iii) excellent corrosion resistance in various harsh chemical environments. Titanium sponge is produced industrially worldwide by the Kroll process, which consists of the metallothermic reduction of gaseous titanium tetrachloride with pure magnesium metal. Even if the Kroll process has been improved since its first industrial production, it still exhibits several drawbacks. Like the ineffective contact between reactants and the use of the volatile and corrosive titanium tetrachloride as the dominant feed. As a result, easier and cheaper production methods have been studied since the early 1970s. One of the alternative processes that has been considered and is showing potential is the aluminothermic reduction of TiO_2. In this study, the use of an aluminothermic reduction process to produce titanium alloys from titania-silica containing slags has been studied.

Two different slags were made in an induction furnace, 18 wt%CaO-82 wt%TiO_2 and 50 wt%CaO-25 wt%SiO_2-25 wt%TiO_2, while the aluminothermic reduction experiments were performed in a vacuum induction furnace. 12 experiments were performed in total, 6 for each slag. Holding time for the aluminothermic reduction was 1 h for all the experiments, while two different holding temperatures were used, 1550 °C and 1650 °C respectively. The aluminium added was varied between 80 %, 100 % and 120 % stoichiometric with respect to the amount of TiO_2 and SiO_2 in the slag with the intention of reducing all TiO_2 and SiO_2. After cooling in the furnace, the reacted slag and metal were cut, cast, and then characterized and analyzed with scanning electron microscopy (SEM), energy dispersive spectroscopy (EDS), electron probe micro-analyzer (EPMA), x-ray powder diffraction (XRD) and inductively coupled plasma mass spectrometry (ICP-MS).

Results from the reacted metal and slag from the experiments with the binary slag showed that there was none or minimal amount of Ti in the metal. In contrast, the amount of TiO_2 in the reacted slag was high. XRD analysis showed the formation of TixOy in the reacted slag, which explained why no Ti was detected in the reacted metal.

Results from the reacted metal and slag from the experiments with the ternary slag showed high concentrations of both Ti and Si in the metal while the amount of TiO_2 was close to 0 wt% in the reacted slag. The concentration of Ti in the reacted metal decrease with increased addition of Al, while a corresponding increase in the concentration of Al in the metal was observed. Observations of SiO_2 in the slag combined with the concentration of Si in the metal being lower than the concentration of Ti implied that the thermodynamic priority of reduction by Al is TiO_2>SiO_2.

Sammendrag

Titan metall har blitt produsert og fremstilt på kommersiell skala siden begynnelsen av 1950-tallet på grunn av dets unike egenskaper: (i) høyt styrke-til-vekt forhold, (ii) forhøyet smeltepunkt, og (iii) utmerket korrosjonsbestandighet i forskjellige tøffe kjemiske miljø. Titan sponge produseres industrielt over hele verden med Kroll prosessen, som består av metallotermisk reduksjon av $TiCl_4$(g) med rent magnesium metal. Selv om denne prosessen er forbedret siden den første industriproduksjonen, har den fortsatt flere ulemper som den ineffektive kontakten mellom reaktantene og bruken av det flyktige og etsende $TiCl_4$. Som et resultat av dette har enklere og billiger produksjonsmetoder blitt studert siden tidlig 1970. En av de alternative metodene som har blitt studert og viser potensial er aluminotermisk reduksjon av TiO_2. I dette studiet har bruken av aluminotermisk reduksjons prosess for å produsere Ti-legeringer fra TiO_2-og SiO_2 holdig slag blitt studert.

To ulike slagger ble laget i en induksjonsovn, 18 wt%CaO-82 wt%TiO_2 og 50 wt%CaO-25 wt%SiO_2-25 wt%TiO_2, mens eksperimentene med aluminotermisk reduksjon ble utført i en vakuuminduksjonsovn. 12 forsøk ble utført total, 6 med hver slag. Holdetiden for reduksjonen var 1 time for alle eksperimentene, mens to ulike holdetemperaturer ble brukt, henholdsvis 1550 °C og 1650 °C. Mengden aluminium tilsatt ble variert mellom 80 %, 100 % og 120 % støkiometrisk med hensyn til mengde TiO_2 og SiO_2 i slaggen med tanke på å redusere all TiO_2 og SiO_2. Etter sakte avkjøling i ovn ble den reagerte slaggen og det reagerte metallet kuttet, støpt og deretter karakterisert og analyser med SEM, EDS, EPMA, XRD og ICP-MS.

Resultatene fra det reagerte metallet og slaggen fra forsøkene med den binære slaggen viste at det var litt eller svært lite titan i metallet, mens mengden TiO_2 i slaggen var høy. XRD analyser av slaggen viste dannelse av Ti_2O_3 og TiO noe som forklarte hvorfor det ikke ble observert noe Ti i metallet.

Resultatene fra det reagerte metallet og slaggen fra forsøkene med ternær slaggen viste nesten 100 wt% av Ti og Si i metallet, mens mengden TiO_2 i slaggen var svært liten. Innholdet av Ti i metallet minket med økende mengde av tilsatt Al, og en tilsvarende økning i innholdet av Al i metallet ble observert. Observasjon av SiO_2 i slaggen, kombinert med at innholdet av Si i metallet var lavere enn Ti implementerer at den termodynamiske prioritering av reduksjon med Al er TiO_2>SiO_2.

Nomenclature

at% Atomic Percent

EDS Energy Dispersive Spectroscopy

EPMA Electron probe micro analyzer

FFC Fray-Farthing-Chen

ICP-MS Inductively coupled plasma mass spectrometry

mass% Mass Percent

mol% Mole Percent

OM Optical Microscopy

OS Ono-Suzuki

ppm Parts per Million

PPR Preform reduction process

SEM Scanning Electron Microscopy

wt% Weight Percent

XRD X-ray powder diffraction

XRF X-ray fluorescence

Contents

List of Figures

List of Tables

Chapter 1

Introduction

1.1 Titanium

Titanium is a durable, light metal that is as strong as steel and twice as strong as aluminium. It is crucial as an alloying agent, with metals including aluminium and iron, mainly used in aircraft, spacecraft, and missiles because of their low density and ability to withstand extreme temperatures [1]. Titanium is currently produced by the Kroll method which, includes several steps, the reduction of purified $TiCl_4$ by magnesium, as well as the electrolysis of $MgCl_2$ generated by the reduction to produce metallic Mg and chlorine [2]. The overall reaction is seen in Eq. (1.1). Even if the Kroll process has been improved since its first industrial production, it still exhibits several drawbacks. As a result, more accessible and cheaper production methods have been studied, including calcio- and aluminothermic reduction, to produce high-purity and low-cost titanium powder or ingots for metallurgical applications.

$$\mathrm{TiCl_4}(l) + 2\,\mathrm{Mg}(l) \rightarrow \mathrm{Ti}(s) + 3\,\mathrm{MgCl_2}(l) \tag{1.1}$$

Research and development focus has been directed towards developing a continuous process to produce high-purity and low-cost titanium powder or ingots for metallurgical applications. Alternative processes that have been studied include: (i) gaseous and plasma reduction, (ii) tetraiodide decomposition, (iii) calcio- and aluminothermic reduction, (iv) disproportionation of $TiCl_3$ and $TiCl_2$, (v) carbothermic reduction, and (vi) electrowinning in molten salts [3]. Metallothermic reduction processes have showed potential and have been studied by among others Ono and Suzuki [4] and at RWTH Aachen University [5][6][7][8]. In this study, the focus has been on the aluminothermic reduction process.

1.1.1 Ti-Si-Al alloys

Aluminium is by far the most important alloying element regarding titanium alloys. These alloys are characterized by low density, high strength, excellent corrosion resistance, and oxidation resistance, and are developed for high-temperature applications in the aerospace and automotive industries.

Ti-Si alloys have excellent casting properties, including a low melting point and good fluidity. The melting temperature of pure titanium lowers with an increase in the amount of silicon, facilitating the casting process.
Ti-Al(Si) alloys are characterized by low density, good resistance against oxidation at 600 °C to 800 °C[9], good thermal stability, high specific strength at high temperatures[10][11], and a favourable ratio of mechanical properties to density.

1.2 Aluminothermic reduction

An aluminothermic reduction is defined as the reduction of a metal compound in which aluminium is used as a reducing agent [8]. The feasibility of the reaction is given when aluminium has a greater affinity for the non-metal of the compound than the desired metal, and the greater the difference in oxygen affinity of aluminium and metal oxide, the higher the ease of reaction [8]. This method is industrially important for the production of many metals and alloys and provides a cost-reduced production method for titanium and titanium alloys. The process involves high heating rates, high temperatures, and short reaction times. A general equation for an aluminothermic reduction is seen in Eq. (1.2).

$$Aluminium + Oxide = AluminiumOxide + Metal + Heat \tag{1.2}$$

1.3 Aim of work

In this master thesis, the aim is to study an aluminothermic reduction of two different slags using aluminium as a reducing agent. The goal is to find an alternative method to produce titanium alloys. The aim is to get a Ti-Al alloy and Ti-Si-Al alloy.

The reacted slag and metal will be studied and analyzed to see if the TiO_2 and SiO_2 have been reduced. The amount of aluminium added will also be varied to see how this affects the resulting metal/alloy, and two different holding temperatures will be applied to see how the temperature affects the reduction reaction. The results will be compared to see how well the reduction goes. The reacted slag and metal will be studied with EDS, EPMA, ICP-MS and XRD. The results will as well be compared to theoretical data and calculations from FactSage.

Chapter 2

Theory and Literature

2.1 Titanium and its alloys

Titanium is the ninth most abundant element in the earth's crust and fourth among structural metals. It has three unique properties: high specific strength, it is the most biocompatible metal, and is the most corrosion-resistant common metal. These properties make Ti a natural selection for biomedical implants and an ideal choice for maritime applications and airspace [1]. In addition titanium has low density ($4.5\,\mathrm{g\,cm^{-3}}$), high fracture toughness, fatigue strength and resistance to crack propagation [12]. In 2019, an estimated 80 % of titanium metal was used in aerospace applications. The remaining 20 % was used in armor, chemical processing, marine hardware, medical implants, power generation, and consumer and other applications [13, p. 174]. About 62 000 t of titanium scrap metal was consumed in 2019, 50 000 t by the titanium industry, 10 000 t by the steel industry, 500 t by the superalloy industry and the remainder in other industries [13, p. 174].

Titanium would also be an ideal structural metal to replace steel in vehicles, but compared to carbon steel, and stainless steel, titanium is at least 20 times more expensive and 4-5 times more expensive, respectively. The root cause of the high cost of titanium is its very strong affinity for oxygen, and thus, it is stable in its highest oxidation state, Ti^{4+}. Among other common metals, only Al, Mg, and Ca form more stable oxides than Ti. The total costs to obtain conventional titanium components are shared: 38 % on obtaining the sponge through the Kroll process, 15 % on refining the sponge by metallurgical processes, and a final 47 % on the machining work [7]. Compared with the steel production, the manufacturing of the titanium sheet is up to 80 times more expensive. By analyzing Table 2.1, it can be concluded with that any effort to reduce the titanium price must be focused on two different directions, (i) achieving a process cheaper than the currently employed one and/or (ii) the development or improvement of inexpensive techniques for the fabrication of final components [7]. In Table 2.2, some of the new methods to produce titanium metals or its powder are presented.

Table 2.1: Cost of titanium, a comparison with the production costs of steel, aluminium, and magnesium products taken from Bolivar et al.[2019][7].

	Cost	($ per pound contained)		
	Steel	Aluminium	Magnesium	Titanium
Ore	0.02	0.10	0.01	0.30
Metal	0.10	0.68	0.54	2.00
Ingot	0.15	0.70	0.60	4.50
Sheet	0.30-0.60	1.00-5.00	4.00-9.00	8.00-50.00

Table 2.2: Processes investigated in the last 10 years to synthesize titanium powder [7].

Name/Company	Country	Type of process
Idaho titanium technologies	USA	Plasma quench process
ADMA	Ukrainian/USA	Chemical and HDH
TiRo/CSIRO	Australia	Chemical
Armstrong/ITP	USA	Chemical
Peruke Ltd	South Africa	Chemical
Vartech	USA	Chemical
FFC/U. Cambridge	UK and USA	Electrolysis
MER Corp	USA	Electrolysis
CSRI International	USA	Chemical
PRP/Tokyo University	Japan	Calciothermic reduction
OS Process/Kyoto University	Japan	Calciothermic reduction

Fig. 2.1 illustrates the major steps of existing methods of producting Ti sponge from ilmenite ore. About 89 % of global titanium reserves is in the form of ilmenite (~45 % to 65 % TiO_2 equivalent), with only 10 % occurring as natural rutile (~95 % TiO_2) [13]. Ilmenite can be smelted using a carbothermal process to yield pig iron and Ti-slag [14]. The main component of Ti-slag is ~80 % Ti-based oxides which are bonded with other metals in the form of metal titanates, including Fe, Mg, Ca, Al, Si, and other transition metals [15].

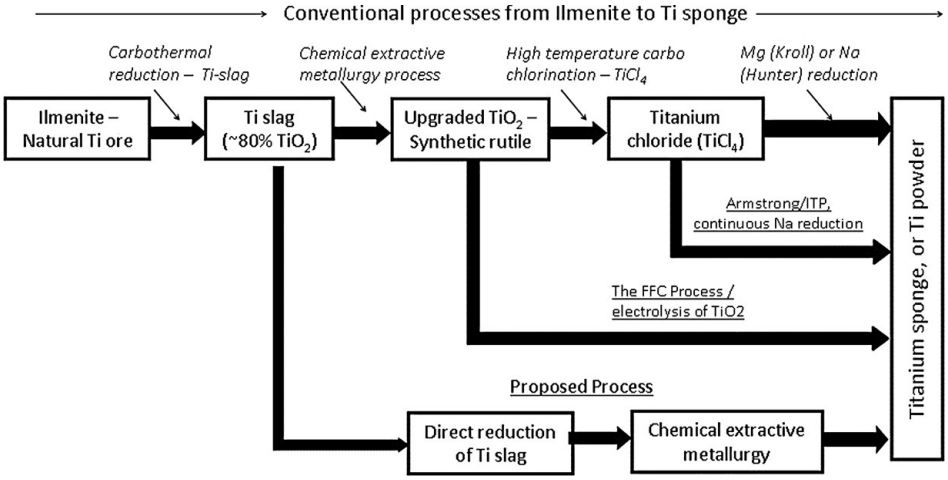

Figure 2.1: Comparison of conventional and developing processes for production of Ti sponge or Ti powder [15].

2.1.1 Application Areas

The chemical industry and aerospace industries are the largest titanium users because of its excellent corrosion-resistance and due to its elevated temperature capabilities and weight savings due to its high strength and low-density [16]. Titanium tends to form oxides instantly upon exposure to air, and this is the reason for the excellent corrosion resistance [16]. Titanium and its alloys are extremely resistant to pitting attack in seawater and have excellent resistance under most oxidizing and neutral reducing conditions. It is corrosion-resistant within the human body and has excellent biocompatibility, which has resulted in use for prosthetic devices. Worldwide utilization of titanium products in the industrial market was approximately 26 000 t in 2016 [7]. Fig. 2.2 shows an industrial titanium demand forecast projected until the year 2020, estimated for the year 2016 to the year 2020, while a summary of some applications of titanium is given in Table 2.3 [7][17].

Table 2.3: Summary of applications of titanium [17].

Industry	Specific uses
Aerospace	Jet engine parts, airplane bodies, rockets, satellites, landing gear, fuel tanks
Chemical	Electric tanks, reactors, distillation towers, separators, plastics, metallurgy
Vessels	Propellers, water jets, vessel pumps, valves, pipes
Ocean engineering	Desalination pipes, offshore oil drilling pumps, valves, pipes
Medical	Dental implants, orthodontics, pacemakers, surgical instruments
Automotive	Exhaust systems, silencer systems, connecting rods, bolts

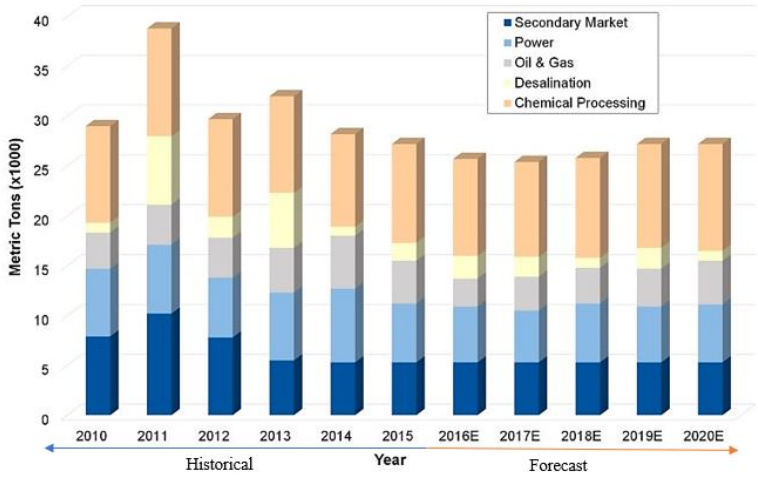

Figure 2.2: Worldwide titanium mill products shipments [18].

Aerospace

As mentioned, the high strength and low density of titanium (~40 % lower than steel) provide many opportunities for weight saving that are utilized in the aerospace industry. The best example of this is its use on the landing gear of the Boeing 777 and 787 aircraft and the Airbus A380 [16]. Fig. 2.3 shows the landing gear on the Boeing 777 aircraft, and all of the labeled parts are fabricated from Ti–10 V–2 Fe–3 Al. This alloy is used in the replacement of high-strength low-alloy steel. This substitution resulted in weight savings of over 580 kg. The alloy used in Boeing 787 is Ti–5 Al–5 V–5 Mo–3 Cr, which has slightly higher strength. The new Boeing 787 Dreamliner is estimated to use 15 % titanium by weight, 5 % more than steel, as can be seen in Fig. 2.4, and is an example for the increased used of titanium in commercial aircraft manufacturing [17].

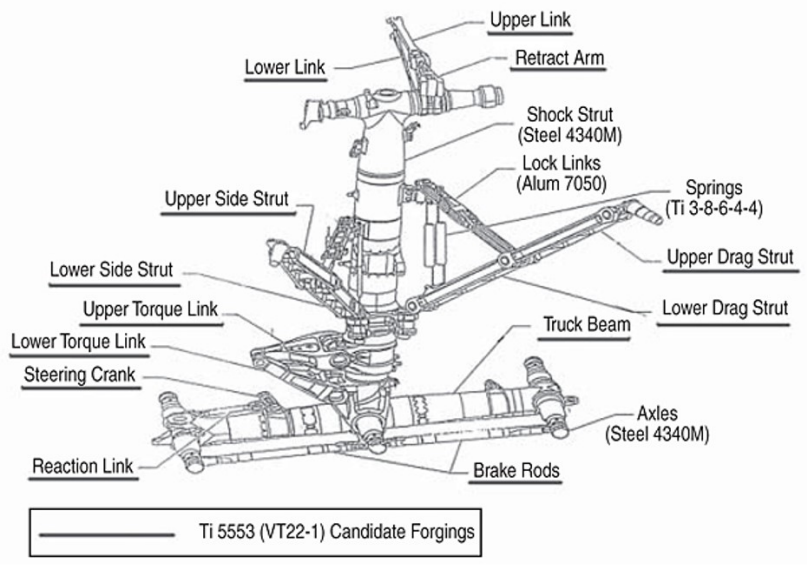

Figure 2.3: Boeing 777 main landing gear. All of the labeled parts are Ti–10 V–2 Fe–3 Al [16].

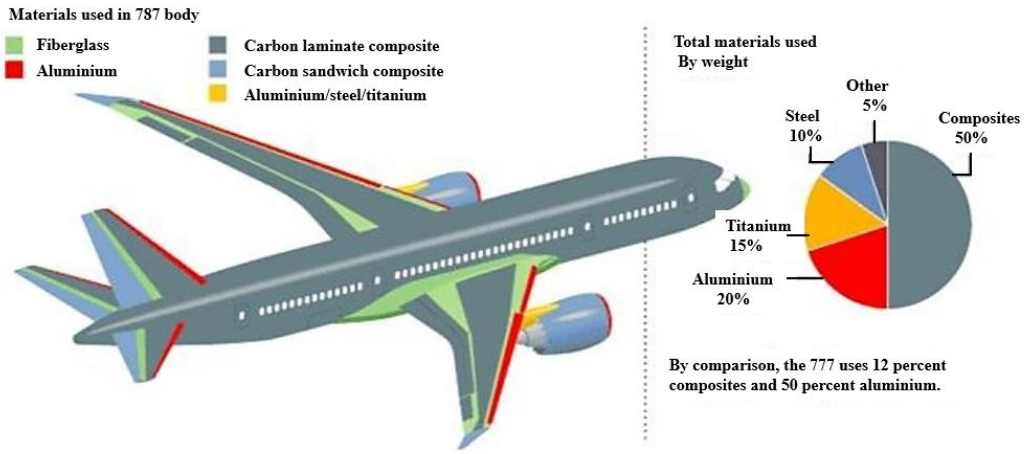

Figure 2.4: Materials used in Boeing 787 body [17].

Military Applications

Titanium has as well an excellent ballistic resistance and combined with 15 % to 35 % weight savings compared to steel or aluminium armor for the same protection and areal densities. This has resulted in substantial weight savings on military ground combat vehicles [16]. Lighter vehicles have better transportability and maneuverability. For overall ballistic performance, Ti–6 Al–4 V that contains mixtures

of α and β phases is well established as the preferred titanium alloy for armor applications and is the benchmark against which all other titanium alloys are compared [19]. The aluminium is an α stabilizer, which stabilizes the α phase to higher temperatures. The vanadium is a β stabilizer, which stabilizes the β phase to lower temperatures. α-β alloys are of interest for armor applications because they are generally weldable, can be heat-treated, and offer moderate to high strength [20]. However, β titanium alloys also have mechanical, physical, and ballistic properties that are of potential interest in a variety of nonaerospace military applications. Fanning [19] compared some β titanium alloys with the Ti−6 Al−4 V alloy, and the conclusion was that as monolithic armor the ballistic performance of β alloys is generally less than of Ti−6 Al−4 V. However, the higher strength and hardness of β alloys may offer advantages in certain types of armor systems for armor-piercing (AP) projectiles. Comparison of Ti−6 Al−4 V with the U.S rolled homogeneous armor (RHA) steel, which is used as the baseline for most ballistic comparisons, has been done by Gooch [20] with the results seen in Table 2.4. As can be seen in Table 2.4, titanium has similar strength, hardness, and elongation to ballistic steel, while the density is 43 % less. This strength to density ratio is the primary factor in the greater performance of titanium over ballistic steel [20].

Table 2.4: Typical Titanium and RHA Mechanical Properties [20].

Material	Source	Density $\mathrm{g\,cm^{-3}}$	Tensile strength MPa	Hardness	Elongation %
Ti−6 Al−4 V	MIL-T-9046J	4.45	>896	302-364HB	>10
RHA	MIL-A-12560	7.85	794-951	241-331HB	11-21

2.1.2 Titanium alloys

Titanium alloys are widely used in high-temperature structural applications in the aerospace or automotive industry. Due to their excellent corrosion resistance, low density, and promising mechanical properties at high temperatures they are applied, especially in aircraft and aircraft engines [8]. Titanium alloys are made by adding elements such as vanadium, molybdenum, aluminium, and others. Titanium alloys can be classified into the following types depending on their influence on the heat-treating temperature and the alloying elements [21][12]:

1. The alpha (α) alloys
2. Alpha-beta (α-β) titanium alloys
3. Beta (β) titanium alloys
4. Ti-Al intermetallic compounds

The alpha (α) alloys contain a large amount of α-stabilizing alloying elements such as aluminium, oxygen, nitrogen, or carbon. Aluminium is by far the most important alloying element. The limitation of these alloys is that they are not heat treatable, but they have good ductility and excellent properties at cryogenic temperatures. They have medium strength but good creep resistance. Typical alloys are Ti−5 Al−2.5 Sn and Ti−6 Al−2 Sn−4 Zr−2 Mo and they are primarily used in the chemical and process engineering industry [22].

The alpha-beta (α-β) titanium alloys contain 4 % to 6 % of β-phase stabilizer elements such as molybdenum, silicon, tantalum, tungsten and vanadium. These alloys are heat treatable and strengthened by precipitation hardening. Besides, they have high fatigue strength, high corrosion resistance, and high creep resistance. Typical alloys are Ti–6 Al–4 V and Ti–6 Al–2 Sn–4 Zr–6 Mo. The Ti–6 Al–4 V is by far the most popular titanium alloy and was one of the first titanium alloys to be made.

Beta (β) titanium alloys contain one or more of the following β stabilizing elements: molybdenum, vanadium, niobium, tantalum, zirconium, manganese, iron, chromium, cobalt, nickel and copper. These alloys exhibit the BCC allotropic form of titanium, and they have excellent formability and can be easily welded. Besides, they have large strength to modulus of elasticity ratios. Typical alloys are Ti–13 V–11 Cr–3 Al and Ti–15 Ta–5 Cr–3 Al–3 Ni.

TixAl intermetallic compounds with x = 1 or 3 have attracted much attention for high-temperature aerospace and automobile applications because of their attractive properties, low density, high strength, high stiffness, and good corrosion, creep, and oxidation resistance [23]. Due to their high specific strength, these alloys have the potential to increase the thrust-to-weight ratio of aircraft engines. However, the TiAl-based alloys have poor toughness and plastic property at room temperature, which make their processing and machining difficult and thereby restraining their wider applications [24]. Typical alloys are Ti–3 Al and TiAl.

Ti-Si alloys have excellent casting properties, including a low melting point, a narrow crystallization range, and good fluidity [25]. The melting temperature of pure titanium lowers with an increase in the amount of silicon, facilitating the casting process. Reducing the melting temperature of titanium could decrease its reactivity with oxygen, decrease the risk of inadequate mold filling, and porosity development due to the considerable temperature difference between the molten alloy and the cooler investment [26]. Si can also be used to strengthen Ti alloys and is known to be safe for use as an alloying element.

The properties of titanium alloys are essentially determined by two factors: the chemical composition and the microstructure. The chemical composition of the titanium alloys primarily determines the properties and volume fraction of the phases, α and β. To generally improve the properties of titanium alloys, there are essentially two ways to proceed: alloying and processing, presented in Fig. 2.5 [22]. Alloying lays the basis for an increase in strength, allows the generation of ordered structures, determines most of the physical properties, and largely controls the chemical resistance of the material. Processing allows the careful balancing of the property profile of materials. Depending on the specific property profile required for the final application, different microstructures can be generated for titanium alloys by means of thermomechanical treatment to optimize for strength, ductility, toughness, stress corrosion, creep resistance and superplasticity.

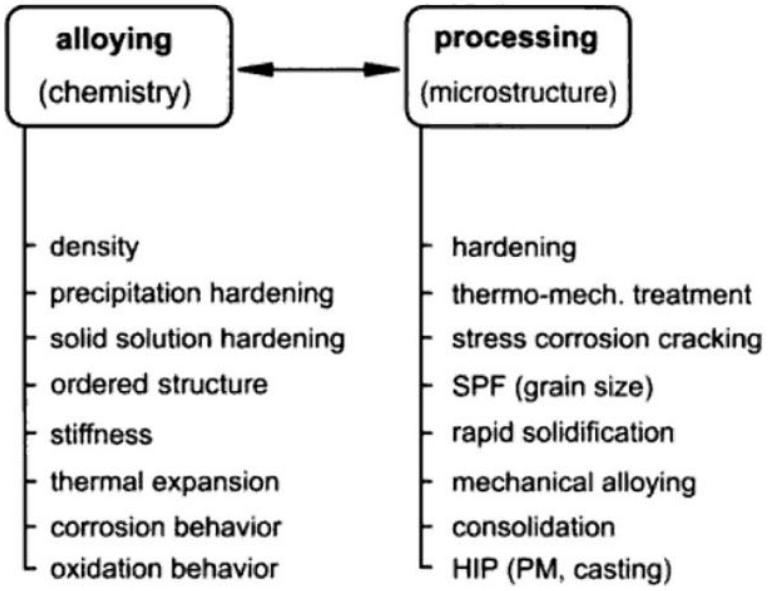

Figure 2.5: Ways to modify the properties of titanium alloys [22].

2.2 Titanium Production Methods

The existing technologies, including both commercial and developmental processes, can be categorized into two groups: electrochemical methods, by reduction of TiO_2, and thermochemical methods, by reduction of $TiCl_4$. Examples of the electrochemical approach are the FCC or Cambridge processes, while the Kroll process is an example of the thermochemical method and is the most commonly used one. Titanium producers have since the 1970's been looking for easier and cheaper processes to replace the Kroll process, like PPR (Preform reduction process), FFC (Fray-Farthing-Chen), and OS (ONO-Suzuki). The Kroll process, FFC, and OS process are discussed further, and a comparison of the features of the processes can be seen in Table 2.5.

Table 2.5: Features of the Kroll process, FFC process and the OS process [27].

Process	Advantages	Disadvantages
Kroll	High-purity titanium obtainable Easy metal/salt separation Established chlorine circulation Utilizes efficient Mg electrolysis Reduction and electrolysis operations can be carried out independently	Complicated process Slow production speed Batch-type process
FFC	Simple process Semicontinuous process	Difficult metal/salt separation Reduction and electrolysis must be carried out simultaneously Sensitive to carbon and iron contamination Low energy efficiency
OS	Simple process Semicontinuous process	Difficult metal/salt separation Sensitive to carbon and iron contamination Low energy efficiency

2.2.1 Kroll Process

In the Kroll process, Ti is extracted from its ore rutile, TiO_2, or titanium concentrates during several steps like carbochlorination, purification, and reduction. The main ore is treated with chlorine gas to produce titanium tetrachloride, $TiCl_4$, which is purified and then reduced by magnesium or sodium to a metallic sponge [2]. During the carbochlorination, carbon and chlorine are used to react with TiO_2 producing $TiCl_4$ and CO or CO_2. In the following purification process, the impurities of silicon, iron, aluminium and magnesium are removed by fractional distillation to generate $TiCl_4$ (99.9 % in purity). Then the $TiCl_4$ is reduced by molten magnesium or sodium in an argon atmosphere to produce sponge titanium [2]. All these steps make this process expensive, labor-intensive, and energy-consuming. The chlorination in the process is rather complicated and of substantial cost, while the reduction of $TiCl_4$ by Mg is the most energy-consuming step [28]. Given its attractive properties and current cost, it is understandable that reducing the cost of Ti production and manufacturing has been and is a continuing and primary motivation for Ti research. The main processing steps in the Kroll process is seen in Fig. 2.6.

The disadvantages with the Kroll process are [29]:

1. extensive equipment: Handling of liquid chlorides, Mg-electrolysis, small vacuum units, post distillation
2. small high grade titanium yield (Fe contamination)
3. small space related productivity
4. high energy consumption
5. mechanical removal of the Ti-sponge necessary

6. discontinuous

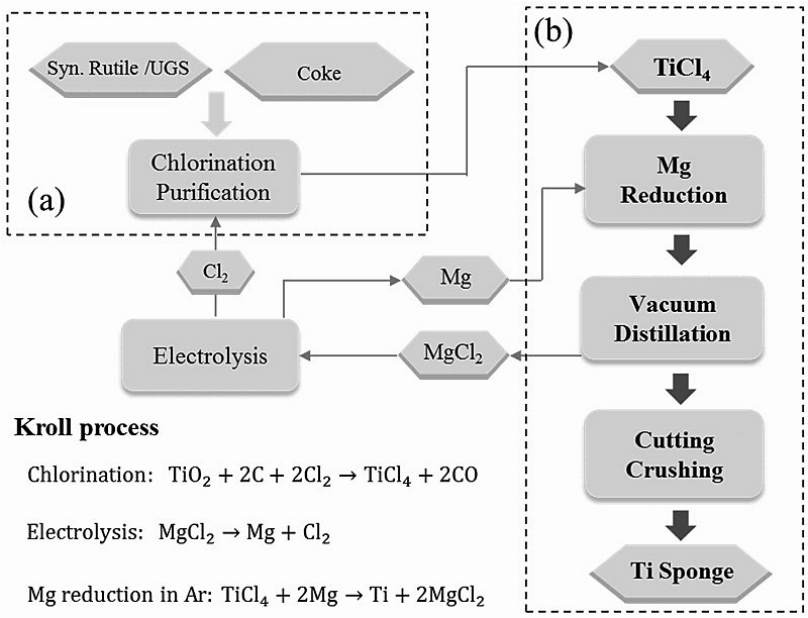

Figure 2.6: Illustration of the main processing steps of the Kroll process: (a) chlorination and (b) reduction of $TiCl_4$ [1].

2.2.2 FFC Cambridge Process

The FFC-Cambridge process, developed by George Chen, Derek Fray, and Tom Farthing, is an electrochemical method in which solid metal compounds, mainly oxides, are cathodically reduced to the respective metals or alloys in molten salts [30]. It was first established for the electro-reduction of TiO_2 to pure titanium in molten $CaCl_2$. In this process, the preformed metal compound (e.g., a pellet of TiO_2) is attached on a cathode which is then electrolyzed against a suitable anode under a cell voltage that is high enough to ionize the oxygen in the metal compound without decomposing the electrolyte (e.g., molten $CaCl_2$) [31]. Fig. 2.7 illustrates schematically the FFC-Cambridge process. The process can also be represented by the following reactions where M represents a metal [31]. Overall reactions are seen in Eq. (2.1), the cathode reaction is seen in Eq. (2.2) and the anode reactions are seen in Eq. (2.3).

$$\begin{aligned} \mathrm{nMO}_x(\mathrm{s}) &= \mathrm{M}(\mathrm{s}) + \mathrm{x}/_2\mathrm{O}_2(\mathrm{g}), (\text{using an inert anode}) \\ \mathrm{nMO}_x(\mathrm{s}) + \mathrm{xC}(\mathrm{s}) &= \mathrm{nM}(\mathrm{s}) + \mathrm{xCO}_n(\mathrm{g}), (\text{using } a \text{ carbon anode}, \mathrm{n} = 1 \text{ or } 2) \end{aligned} \tag{2.1}$$

$$\mathrm{MO}_x(\mathrm{s}) + 2\,\mathrm{xe}^- = \mathrm{M}(\mathrm{s}) + \mathrm{xO}^{2-} \tag{2.2}$$

$$\begin{aligned} \mathrm{xO}^{2-} &= x/2\mathrm{O}_2(\mathrm{g}) + 2\,\mathrm{xe}^-, (\text{using an inert anode}) \\ \mathrm{nO}^{2-} + \mathrm{C(s)} &= \mathrm{CO}_n(\mathrm{g}) + 2\,\mathrm{ne}^-, (\text{using } a \text{ carbon anode, n} = 1 \text{ or } 2) \end{aligned} \tag{2.3}$$

The mechanism first proposed by Chen et al. [30] is that when calcium is deposited on titanium foil cathode, it reacts with the oxygen in the foil to form CaO, which is soluble in molten $CaCl_2$. An alternative explanation is that oxygen ionization occurs at a less cathodic potential than calcium deposition, and so direct reduction of titanium oxides to titanium metal can be achieved electrochemically rather than by the chemical reaction with calcium [30]. These two concepts are seen in Eq. (2.4), which represents the deposition of calcium at a more cathodic potential, while Eq. (2.5) represents ionization of oxygen at a less cathodic potential.

$$\begin{aligned} \mathrm{Ca}^{2+} + 2\,\mathrm{e}^- &\leftrightarrow \mathrm{Ca} \\ \mathrm{TiO}_x + \mathrm{xCa} &\leftrightarrow \mathrm{Ti} + \mathrm{xCaO} \end{aligned} \tag{2.4}$$

$$\mathrm{TiO}_x + 2\,\mathrm{xe}^- \leftrightarrow \mathrm{Ti} + \mathrm{xO}^{2-} \tag{2.5}$$

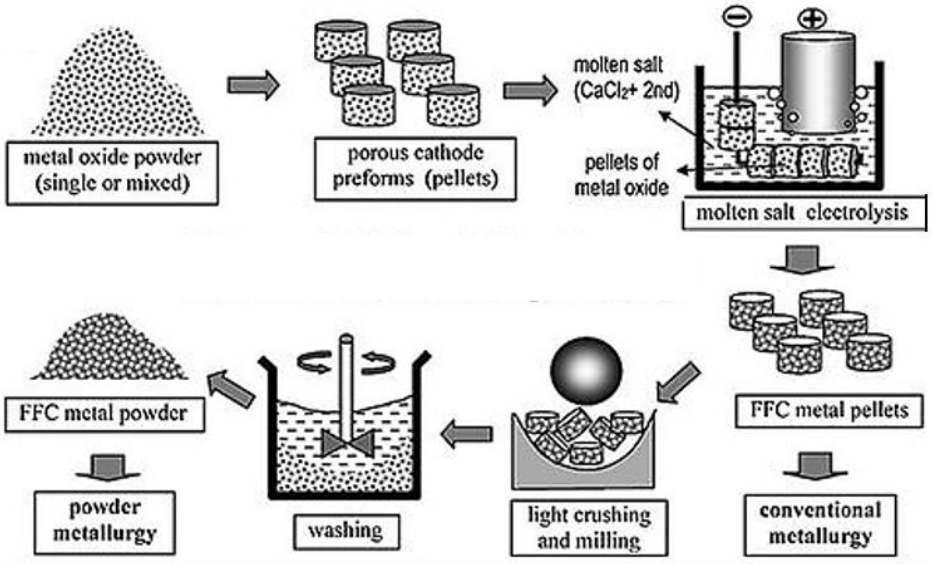

Figure 2.7: An illustration of the FFC-Cambridge process for the electrochemical reduction of solid metal oxide to solid metal in molten salt [31].

For titanium production, the FFC-Cambridge process commonly uses pigment grade TiO_2 as the feedstock, which is safer to handle and transport than $TiCl_4$ used in the Kroll process [31]. In addition it is only

necessary with 1.66 kg of TiO_2 to produce 1 kg of titanium whereas 4 kg of $TiCl_4$ is required for the same yield. Understanding of the mechanisms and kinetic barriers of the FFC-Cambridge process has progressed steadily in recent years, leading to the production of titanium with < 2000 ppm oxygen at 32.3 % in currently efficiency and 21.5 kW h kg^{-1} in energy consumption [31].

2.2.3 OS Process

The OS process was developed by Ono and Suzuki in 2002 [4]. In this process, titanium is produced through a calciothermic reaction with TiO_2 powder. Calcium is dissolved with a strong reducing power infused $CaCl_2$, which constitutes the media, and the TiO_2 powder is directly top-charged into this media and reduced. A schematic diagram of the electrolytic cell for this process is shown in Fig. 2.8. As said, the TiO_2 powder is reduced in molten $CaCl_2$ containing Ca^+ and free electrons. The reduction by-product CaO dissolves in the bath according to the electrochemical reaction [4]:

$$TiO_2 + 2\,Ca^+ + 2\,e^- = Ti + 2\,Ca^{2+} + 2\,O^{2-} \tag{2.6}$$

If TiO_2 particles meet liquid calcium droplets, they are also immediately reduced to metal by the thermochemical reaction:

$$TiO_2 + 2\,Ca = Ti + 2\,Ca^{2+} + 2\,O^{2-} \tag{2.7}$$

Under the conditions used in the process, the dissolved CaO is electrochemically decomposed in-situ in the electrolyte to form CO/CO_2 gases at the carbon and the metallic calcium at the cathode, with an overall cell reaction being expressed as [32] and can also be observed in Fig. 2.8:

$$(CaO) + C = Ca + CO\,(g) \tag{2.8}$$

The reduced calcium metal dissolves into the $CaCl_2$ melt and is used as the calcium reductant again for the reduction of TiO_2. Table 2.6 shows a comparison of the theoretical electric energy consumption in the production of titanium by the Kroll process and the OS process done by Ono et al. [4]. According to this analysis, the theoretical electric power requirement is approximately half of that for the conventional process of magnesium recovery by electrolysis. However, technical improvements have to be established before this process is scaled up for large-scale operations, since it is difficult to control the purity and quality of the reduced titanium metal [32].

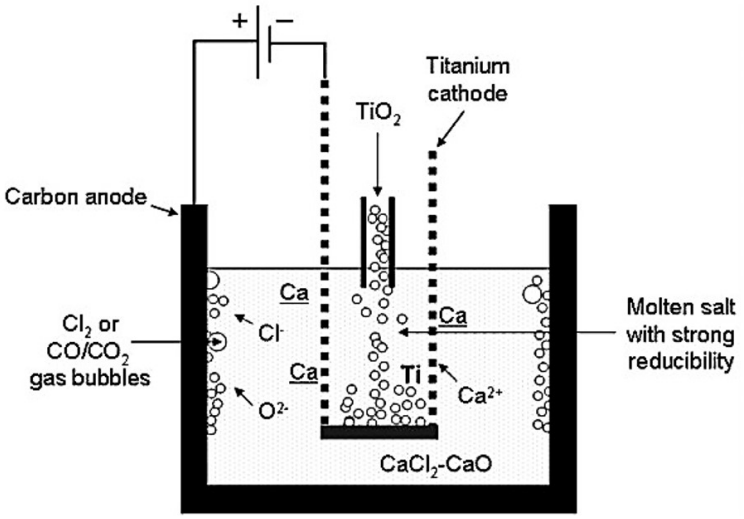

Figure 2.8: Schematic illustration of the OS process for titanium powder production [32].

Table 2.6: Theoretical electric energy consumption in the titanium production processes [4].

	Kroll Process	**OS Process**
Electrolytic reaction and enthalpy change	$MgCl_2 = Mg + Cl$ $\Delta\ H = +598.8$ kJ (1000 K, endothermic)	$CaO + \frac{1}{2}\,C = Ca + \frac{1}{2}\,CO_2$ $\Delta\ H = +445.1$ kJ (1200 K, endothermic)
Reduction reaction and enthalpy change	$TiCl_4 + 2\,Mg = Ti + 2\,MgCl_2$ $\Delta\ H^0 = -420.0$ kJ (1200 K, exothermic)	$TiO_2 + 2\,Ca = Ti + 2\,CaO$ $\Delta\ H^0 = -340.3$ kJ (1200 K, exothermic)
Remarks	Heat generated by the reduction reaction is all discarded because the electrolysis and reduction are operated separately.	Heat generated by the reduction reaction is used in the electrolytic reaction.
Theoretical electric	6945 kW h t^{-1} Ti	3189 kW h t^{-1} Ti

2.2.4 Metallothermic Processes

During the last decade, various investigations have been conducted to find alternative routes to the Kroll process for the production of titanium metal. Metallothermic reduction reactions have been investigated as an alternative to produce titanium metal and titanium powder. Metallothermic reduction reactions

are displacement reactions that use reactive metals to reduce compounds so that metals, alloys, nonmetal elementary substances, and composites are produced, often in a scalable manner [33]. Less noble metals than titanium, like Mg, Al and Ca, Li and Zr can be used to reduce titanium dioxide by metallothermic reduction. Among these metals, Mg and Al are especially attractive, due to their affordable price and low melting or boiling point [6].

Fig. 2.9 shows the Ellingham diagram with the important reactions pointed out. $\Delta\ G^0$ in the diagram represents the thermodynamic energy barrier a system needs to overcome for a given reaction to take place [34]. The more negative a reactions $\Delta\ G^0$ is, the larger the driving force for the reaction will become. A consequence of this is that elements with more negative $\Delta\ G^0$ should form oxides first. As seen in Fig. 2.9 the line for aluminium (green line) is further down in the diagram than silicon (red line) and titanium (blue line). This means that aluminium requires less energy to oxidise to Al_2O_3 than silicon to SiO_2 and titanium to SiO_2, meaning that Al_2O_3 is a more stable compound than SiO_2 and TiO_2. Eq. (2.9) and Eq. (2.10) show the ideal reactions, both of them being exothermic, meaning they will generate heat. As can be seen as well, is than calcium oxide (orange line) is below the line for aluminium, which means that calcium requires less energy to oxidize to CaO than aluminium to Al_2O_3, meaning that CaO is a more stable compound than Al_2O_3, SiO_2, and TiO_2.

$$3\,TiO_2 + 4\,Al = 3\,Ti + 2\,Al_2O_3 \tag{2.9}$$

$$3\,SiO_2 + 4\,Al = 3\,Si + 2\,Al_2O_3 \tag{2.10}$$

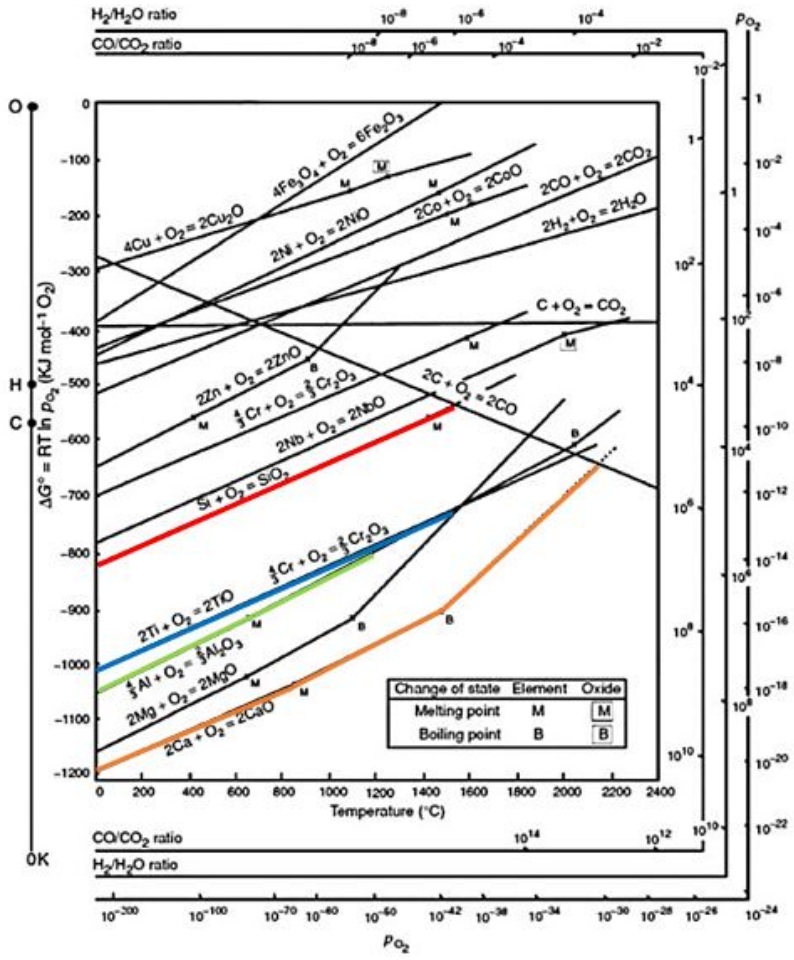

Figure 2.9: Ellingham diagram [35]. Red line: Si oxidation, Blue line: Ti oxidation, Green line: Al oxidation, Orange line: Ca oxidation.

Aluminothermic Reduction

Aluminothermic processes are usually applied to manufacture master alloys for the steel and superalloy industries by reducing mostly refractory metal oxides or ores, offering a carbon-free production method. The aluminothermic process provides a cost-reduced production method for titanium and titanium alloys by reduction of TiO_2 with subsequent refining by electro slag remelting [8]. This process offers great potential to replace the Kroll-process and provides the least expensive production method for the direct synthesis of titanium alloys. However, an aluminothermic reduction can not produce pure metallic titanium with low oxygen contents at the same time because oxygen activity in the equilibrium slag is relatively high, and over-stochiometric aluminium charge causes the formation of stable intermetallic alloys with titanium. On the other hand, this makes it an attractive process to obtain alloys TiAlX [6].

The possible chemical reactions involved during the aluminothermic reduction of TiO_2 in cryolite media can be represented by the following set of equations taken from [36]:

$$\mathrm{Al(l)} + 3\,\mathrm{TiO_2(s)} = \frac{3}{2}\,\mathrm{Ti_2O_3(s)} + \frac{1}{2}\,\mathrm{Al_2O_3(s)} \tag{2.11}$$

$$\mathrm{Al(l)} + \frac{3}{2}\,\mathrm{TiO_2(s)} = \frac{3}{2}\,\mathrm{TiO\,(s)} + \frac{1}{2}\,\mathrm{Al_2O_3(s)} \tag{2.12}$$

$$\mathrm{Al(l)} + \frac{3}{4}\,\mathrm{TiO_2(s)} = \frac{3}{4}\,\mathrm{Ti\,(s)} + \frac{1}{2}\,\mathrm{Al_2O_3(s)} \tag{2.13}$$

$$\mathrm{Al(l)} + \frac{3}{2}\,\mathrm{Ti_2O_3(s)} = 3\,\mathrm{TiO\,(s)} + \frac{1}{2}\,\mathrm{Al_2O_3(s)} \tag{2.14}$$

$$\mathrm{Al(l)} + \frac{1}{2}\,\mathrm{Ti_2O_3} = \mathrm{Ti\,(s)} + \frac{1}{2}\,\mathrm{Al_2O_3(s)} \tag{2.15}$$

$$\mathrm{Al(l)} + \frac{3}{2}\,\mathrm{TiO\,(s)} = \frac{3}{2}\,\mathrm{Ti\,(s)} + \frac{1}{2}\,\mathrm{Al_2O_3(s)} \tag{2.16}$$

The Gibbs free energy of these equations calculated by FactSage 6.4 is shown in Fig. 2.10. As mentioned, it is thermodynamically desirable for a chemical reaction with a low amount of negative Gibbs free energy change. From the figure, it is obvious that Eq. (2.11) has the most negative value, followed by Eq. (2.12). Meaning that, thermodynamically, it is not difficult for TiO_2 to be reduced to Ti_2O_3 and Ti_2O_3 to be reduced to TiO as mentioned earlier. By contrast Eq. (2.16) shows that reduction of TiO to Ti is the most difficult from the thermodynamic point of view [36].

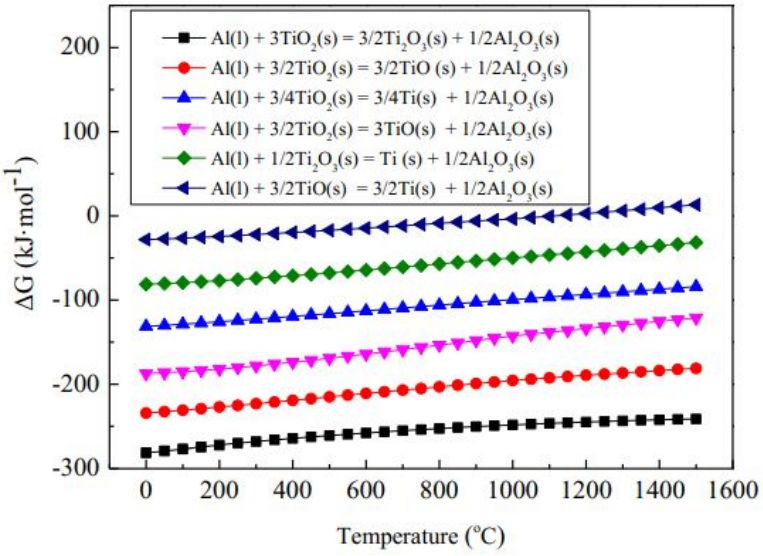

Figure 2.10: Gibbs free energy changes of possible chemical reactions involved in the system of TiO_2 and Al [36].

The reduction of TiO_2 by aluminium was studied by Kubaschewski/Dench [37] and can be expressed simplified by following equation [5]:

$$3\,TiO_2 + 7\,Al \rightarrow 3\,TiAl + 2\,Al_2O_3 \tag{2.17}$$

By adjusting molar Al/TiO_2 ratio of feed material, composition, and oxygen content can be influenced. For decreasing oxygen content below 1 %, Al/TiO_2 ratio must be higher than 2.5 [37]. Further fundamental research projects from Maeda et al. [28] dealt with the aluminothermic reduction of TiO_2 under a $CaF_2-CaO-Al_2O_3$ slag in an atmosphere of argon and alumina crucible. The overall reaction, seen in Eq. (2.18), was finished within 10 min. A flux was used to dissolve alumina, and a slag of CaF_2-CaO was chosen because of its fluidity and capability to absorb aluminium oxide. Table 2.7 describes the materials and weights used with the composition of flux being selected based on these conditions,

(1) As soon as the aluminium oxide is formed, it should be dissolved in the flux.
(2) When titanium oxide is completely reduced, all aluminium oxide should be absorbed in the flux.
(3) The ratio of CaO to CaF_2 should be as high as possible to minimize the use of CaF_2, thus reducing the cost.

The metal and slag was heated up to 1700 °C and then kept for some time. Metal with 68.9 mass% Ti, 25.8 mass% Al and slag containing 6.54 mass% TiO_2 and 46.7 mass% Al_2O_3 were obtained for the sample quenched as soon as it reached 1700 °C. The titanium and aluminium content in metal as a function of time is seen in Fig. 2.11a and the titania and alumina content in slag as a function of time is seen in Fig. 2.11b.

It was concluded with,

(1) The rate of aluminothermic redution of titanium oxide was so fast that it was completed within ten minutes at 1700 °C.
(2) When the molar ratio of aluminium to titanium oxide was $\frac{4}{3}$ (which corresponds to the stoichiometric ratio), alloy containing 5 mass% oxygen and 15 mass% aluminium was obtained; and a ratio was 2.8 realized a metal containing 0.42 mass% oxygen and 42 mass% aluminium.
(3) At 1700 °C, in titanium equilibrated with $CaO-CaF_2-Al_2O_3$ slag in an alumina crucible, the relation between oxygen and aluminium in titanium melt could be expressed as

$$\ln(\%\,O)^3 = -\ln(\%\,Al)^2 + 10.69$$

(4) Free energy change of the dissolution of oxygen in titanium was estimated as $-901\,kJ\,mol^{-1}$ at 1700 °C.

$$TiO_2 + \frac{4}{3}\,Al = Ti + \frac{2}{3}\,Al_2O_3 \tag{2.18}$$

Table 2.7: Material mass.

Molar ratio Al/TiO_2	Added TiO_2 (g)	Added Al (g)	Added Flux (g)
1.0	5.00	1.69	2.51
1.3	5.00	2.25	3.35
1.6	5.00	2.70	3.35
1.9	5.00	3.21	3.35
2.2	5.00	3.71	3.35
2.5	5.00	4.22	3.35
2.8	5.00	4.72	3.35

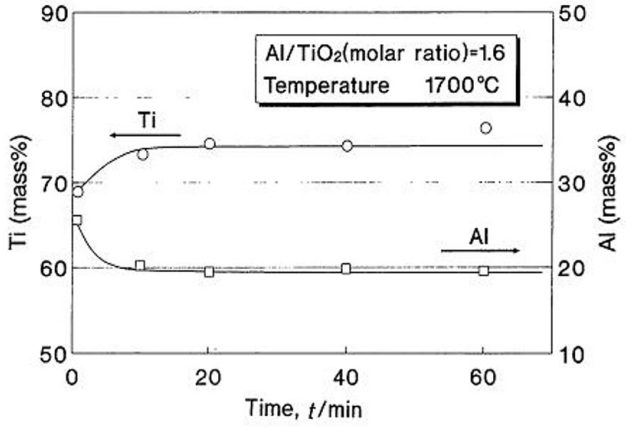

(a) Titanium and aluminium content in metal as a function of time after the temperature reached 1700 °C [28].

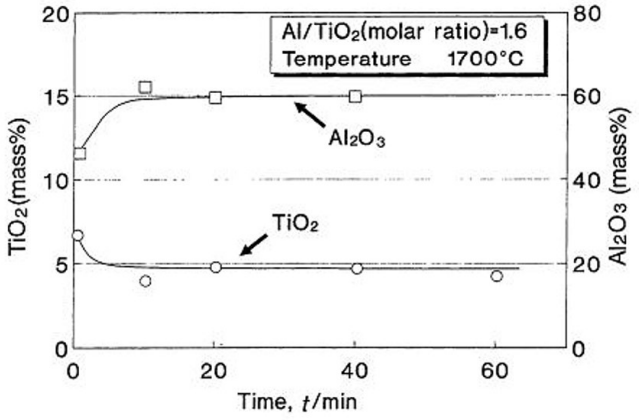

(b) Titania and alumina content in slag as a function of time after the temperature reached 1700 °C [28].

Pourabdoli et al. [38] produced ferrotitanium from titania slag by an aluminothermic process in an Electro

Slag Crucible Melting furnace. The effect of Al and flux additions on titanium recovery, ferrotitanium yield, and Ti/Al ratio were studied. It was found that an increase in Al amount led to a decrease in Ti recovery and Ti/Al ratio. X-ray diffraction patterns of the ferrotitanium slag showed that the titanium recovery declined due to the formation of titanium suboxides and aluminium titanate (Al_2TiO_5) in slag. In the aluminothermic process, a portion of TiO_2 reduces to TiO and Ti_2O_3. These oxides are stable, and their reduction is difficult. TiO is a strong basic compound that reacts with Al_2O_3 in the slag and does not incorporate in the reduction reaction. It also seems like this problem is made more severe by increasing the Al in the charge because this causes an increase in Al_2O_3 in the slag, which is reacted with titanium oxides resulting in a decline in the Ti recovery. Fig. 2.12a shows the effect of the Al amount in the charge on the titanium recovery while Fig. 2.12b shows the XRD pattern from the slag sample from ferrotitanium related to point A. As can be seen, the titanium recovery decreases when the Al increases in the charge, which is explained by the observation of TiO and Al_2TiO_5 phases in the slag. Fig. 2.13 represents the experimental results of the Al amount on Ti and Al contents of ferrotitanium. As can be seen, the residual Al in the ferrotitanium increases while the Ti content decreases when the Al amount is increased.

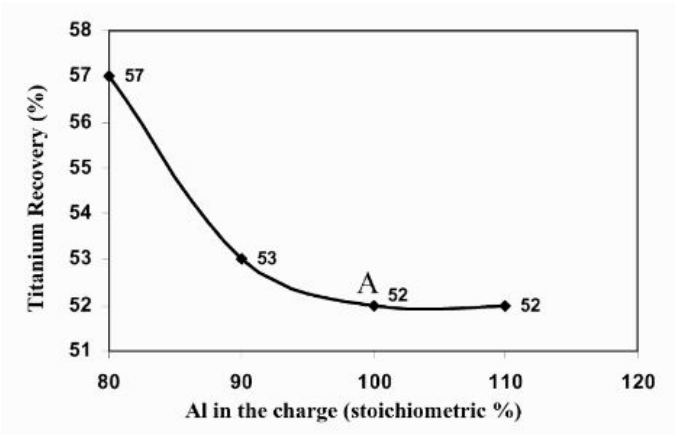

(a) Influence of Al addition in the charge on Ti recovery.

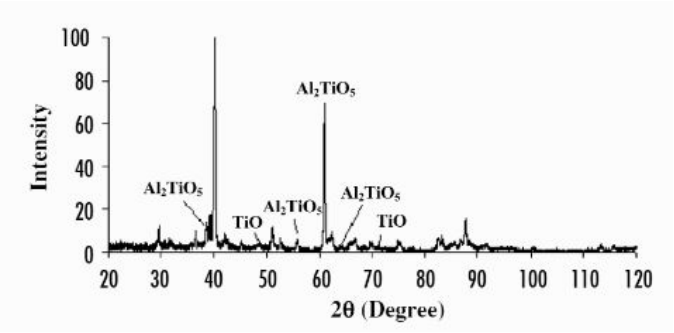

(b) XRD pattern of slag related to experiment No.3, point A in Fig. 2.12a.

Figure 2.12: Influence of Al addition and XRD pattern from one of the experiments from [38].

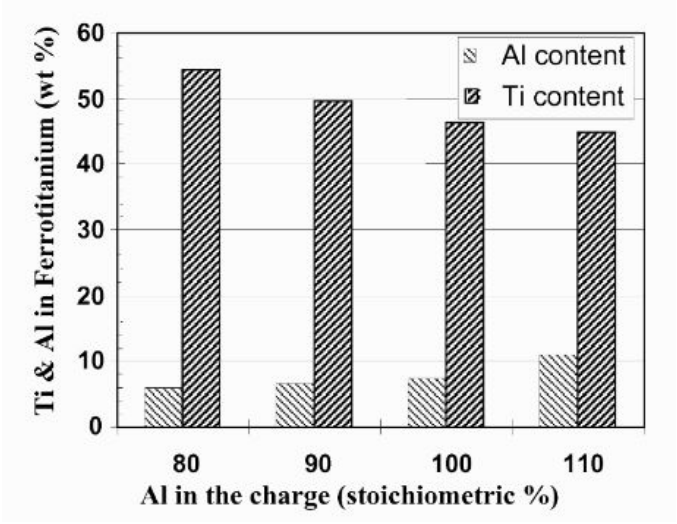

Figure 2.13: Al in the charge (stoichiometric %) [38].

Wang et al. [39] studied the production of ferrotitanium alloy from titania slag based on aluminothermic reduction. As can be seen in Fig. 2.14, according to the Gibbs free energy change of chemical reaction from FactSage calculation, the constituents of TiO_2 and SiO_2 in titania slag and additive Fe_2O_3 are able to spontaneously react with the metallic Al. In terms of thermodynamic reaction priority, the aluminothermic reduction of Fe_2O_3 occurs most easily and preferentially, while SiO_2 is close to TiO_2. As can be seen as well from the figure, all three reactions are exothermic. Eq. (2.19), Eq. (2.21) and Eq. (2.23) show the aluminothermic reactions while Eq. (2.20), Eq. (2.22) and Eq. (2.24) show the corresponding Gibbs free energy changes [39]. This study showed that an increase in the addition of Al leads to an increase of Ti, Si, and Al contents in the alloy phase, indicating the increase of reductant promotes the reduction of silicon and titanium oxides. However, when the ratio of Al/titania slag was more than 12 wt%, the growth trend of Ti in the alloy started to slow down, as well as the Si, while the Al content continued to increase, seen in Fig. 2.15.

$$\mathrm{Al} + 0.75\,\mathrm{TiO_2} \rightarrow 0.75\,\mathrm{Ti} + 0.5\,\mathrm{Al_2O_3} \tag{2.19}$$

$$\Delta G_1 = \Delta G_1^0 + RT \ln \frac{a_{Ti}^{0.75} a_{Al2O3}^{0.5}}{a_{Al} a_{TiO2}^{0.75}} \tag{2.20}$$

$$\mathrm{Al} + 0.5\,\mathrm{Fe_2O_3} \rightarrow \mathrm{Fe} + 0.5\,\mathrm{Al_2O_3} \tag{2.21}$$

$$\Delta G_2 = \Delta G_2^0 + RT \ln \frac{a_{Fe} a_{Al2O3}^{0.5}}{a_{Al} a_{Fe2O3}^{0.5}} \tag{2.22}$$

$$\mathrm{Al} + 0.75\,\mathrm{SiO_2} \rightarrow 0.75\,\mathrm{Si} + 0.5\,\mathrm{Al_2O_3} \tag{2.23}$$

$$\Delta G_3 = \Delta G_3^0 + RT \ln \frac{a_{Si}^{0.75} a_{Al2O3}^{0.5}}{a_{Al} a_{SiO2}^{0.75}} \tag{2.24}$$

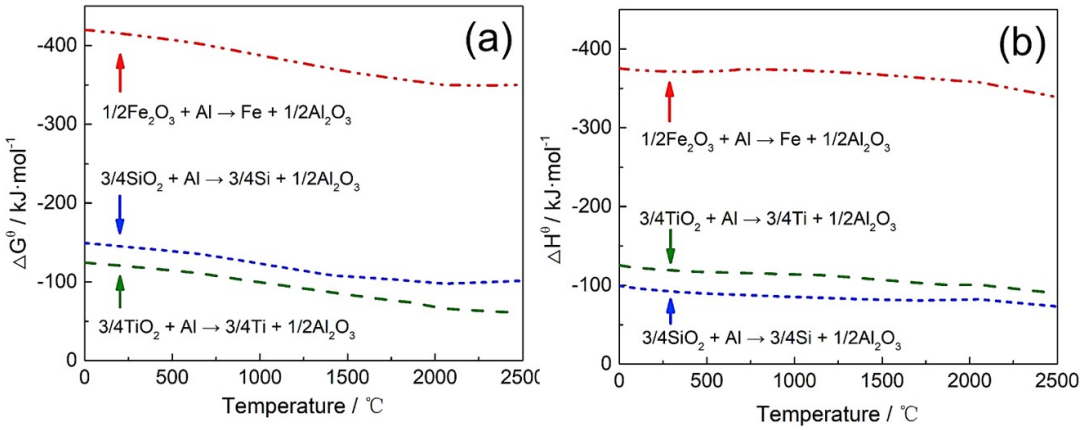

Figure 2.14: Gibbs free energy change (a) and enthalpy change of the main reactions from Wang et al.[39].

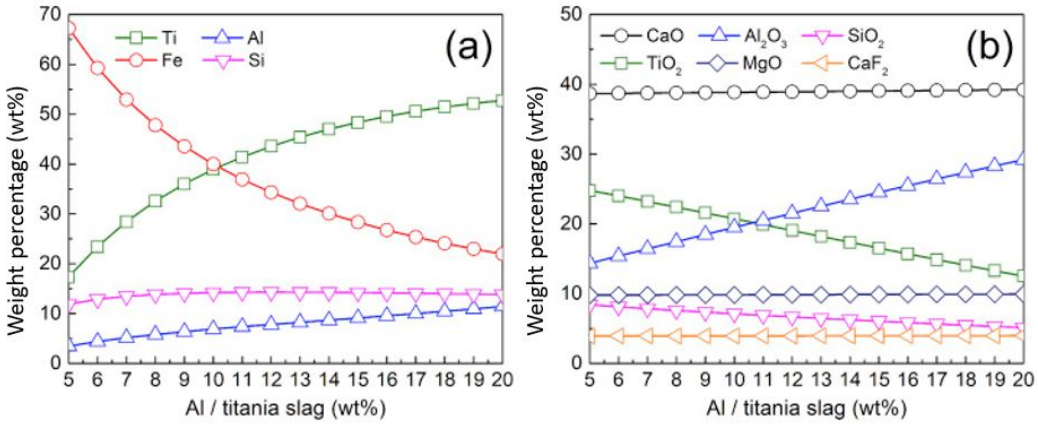

Figure 2.15: Compositions and contents of slag and alloy phases along with Al/slag changing at thermodynamics equilibrium conditions, (a) alloy contents, and (b) slag contents.

Calciothermic Reduction

Another metallothermic reduction process that has been studied is the metallothermic reduction of titanium oxide using calcium metal as the reducing agent. The OS process discussed in Section 2.2.3 is a calciothermic reduction process. Metallic calcium can reduce TiO_2 directly into metallic Ti to the oxygen level of 300 mass ppm to 730 mass ppm, which fits for the industrial standards [40]. Alexander [41] proposed the reduction of TiO_2 using Ca first in 1936:

$$TiO_2 + 2\,Ca = Ti + 2\,CaO \tag{2.25}$$

As seen in Eq. (2.25) the TiO_2 powder is reduced in the molten $caCl_2$ containing Ca^+ and free electrons. The reduction byproduct CaO forms a film on the surface of the Ti particles as illustrated in Fig. 2.16. If TiO_2 particles meet liquid calcium droplets, they are also immediately reduced to metal by the thermochemical reaction:

$$TiO_2 + 2\,Ca = Ti + 2\,Ca^{2+} + 2\,O^{2-} \tag{2.26}$$

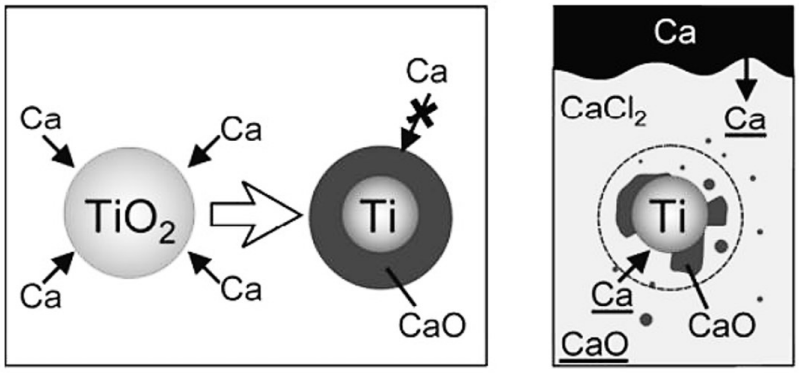

Figure 2.16: Schematic mechanism for calcium reduction and CaO removal in the molten $CaCl_2$. Calcium reduction to the left and calcium reduction in molten $CaCl_2$ to the right [42].

The CaO in both Eq. (2.25) and Eq. (2.26) dissolves into the bath, and it can be converted to Ca^+ and CO_2 gas by electrolysis at temperatures over the melting point of calcium. As seen from Table 2.6, presented in Section 2.2.3, that shows a comparison of the theoretical electric energy consumption in the production of titanium by the Kroll process and the calciothermic reduction process done by Ono et al. [4], the theoretical electric power requirement is approximately half of that for the conventional process of magnesium recovery by electrolysis. However, technical improvements have to be established before this process is scaled up for large-scale operations, since it is difficult to control the purity and quality of the reduced titanium metal [32].

Magnesiothermic Reduction

The reduction of titanium dioxide by magnesium is one of the new approaches that has been investigated and is currently under experimental research at RWTH Aachen University [6]. Magnesium is attractive due to price, low melting or boiling point and that it can reduce titanium dioxide to metallic titanium for further treatment as charge material in common titanium processes [6]. As magnesium exhibits a boiling point 192 °C lower than calcium, using it as a reducer could save energy during the reduction process in comparison to calcium [7]. Magnesiothermic reduction of titanium dioxide is considered to be the first step

to obtain titanium with an acceptable oxygen content of $< 2\,\%$. The magnesiothermic reduction can be represented by the following theoretical equation:

$$TiO_2 + 2\,Mg = Ti + 2\,MgO,\ \Delta H = -129.1 kJ\,mol^{-1} \tag{2.27}$$

As can be seen from Fig. 2.17 reduction of any titanium oxide with magnesium below 1400 °C is thermodynamically favorable, while at temperatures higher than 1400 °C only TiO_2 can be produced.

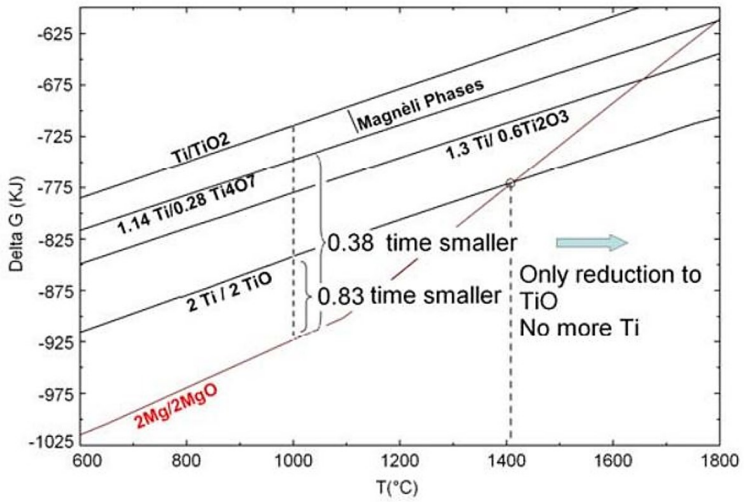

Figure 2.17: Ellingham diagram for titanium oxide [6].

There have been several attempts to use magnesium as a reducer for titanium dioxide within the last years. Titanium powder or titanium wires have been deoxidized using magnesiothermic methods by Kubaschewsky [43] and Miyazaki [44]. Deoxidized titanium with 1.8 wt% to 2.8 wt% oxygen content was obtained, but the results by both researchers do not show any correlation, their tendency lines are quite the opposite as can be seen in figure Fig. 2.18.

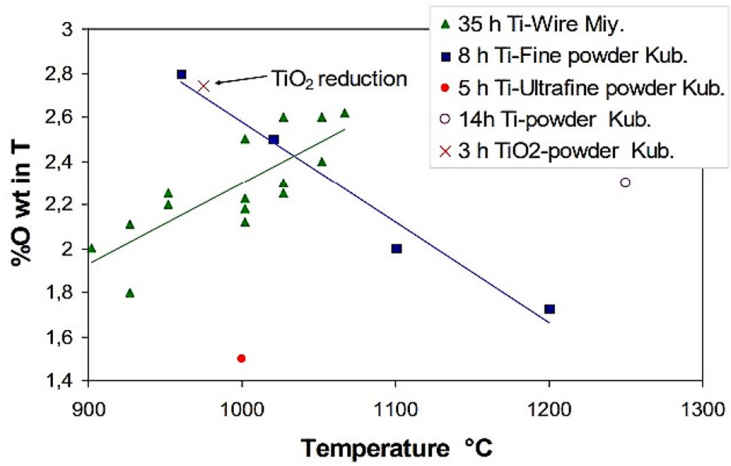

Figure 2.18: Oxygen content reached in magnesiothermic titanium deoxidation [44][43].

Bolivar et al. [7] proposed a four-step process to obtain titanium powder presented in a research article published in 2019. The first step is the reduction of titanium dioxide by magnesium to low titanium oxygen content, followed by an acid leaching step to recover the powder, which is used as a raw material in a subsequent calcium deoxidation process with its leaching process. Then another acid leaching step to obtain the low oxygen content titanium powder. The first two steps are seen in the dotted area in Fig. 2.19. The use of calcium as a dioxider is necessary because magnesium cannot deoxidize titanium to the required levels. These magnesiothermic reduction experiments were carried out to evaluate the influence of temperature and molar ratio of Mg/TiO_2, while different mixtures of acid were used to evaluate the purification of solid titanium metal by the dissolution of Mg, MgO, Ni, Fe, magnesium titanates, and titanium oxides.

The reactants used for the reduction process were titanium dioxide powder "Kronos 3000" with the following properties: TiO_2 purity $\geq$ 99 wt%, size distribution 86 wt% of particles >100 µm and 0.2 wt% of particles <800 µm, X50-Value (media size particle) of 200 µm, and granulated magnesium of commercial grade purity. The leaching step was carried out with analytical grade HCl, HNO_3, and H_2SO_4 acids.

The reduction was carried out in a sealed rotary tube reactor that allowed three different configurations:

1. The reactants were put into contact with each other in each compartment
2. The reagents were placed separately in each compartment allowing a free flow of Mg vapor from the magnesium compartment to the TiO_2 compartment during the entire heating time
3. Isolated compartments with TiO_2 and Mg placed separately

In the leaching process the efficiency of four different acid solutions and a mixture of 8HCl% + 3HNO_3% was tested during 1 or 24 h.

The results showed that high yield of titanium and a homogeneous product mainly conformed by Ti, Mg

and MgO with low proportion of Ti_2O and Ti_2O_3 was obtained when TiO_2 and Mg were placed separately on the sealed reactor. When TiO_2 and Mg were placed with each other, a heterogeneous product conformed of Ti, Mg, MgO, $Mg_{1.5}Ti_{1.5}O$, Ti_2O and Ti_2O_3 was obtained. And, when magnesium gas was allowed to react at 1030 °C with titanium, the homogeneous products obtained were Ti_2O and MgO. The best leaching condition found was a micture of 8HCl% + 3HNO_3% for 24 h at maximum 20 °C, which resulted in the highest dissolution of both the magnesium excess and magnesium oxide, very close to 100 %. The titanium particles obtained were approximately of 0.5 µm size with a content of oxygen on an average of 3.25 wt%.

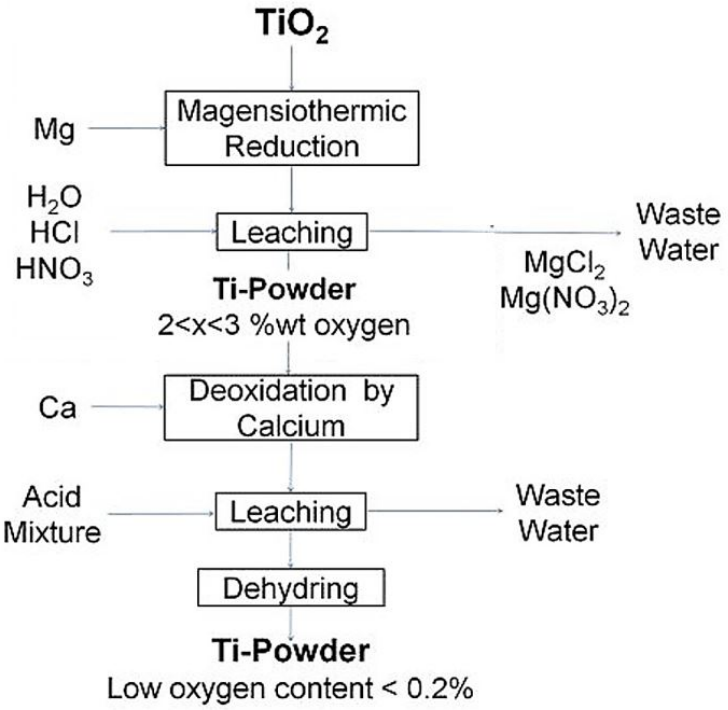

Figure 2.19: Investigated process to produce titanium powder by magnesiothermic reduction from rutile [7].

2.3 Phase Diagrams related to the Aluminothermic Procedure

In this thesis, the aluminothermic reduction of two different slags containing titania and silica is studied. The reasons for choosing this process are, among other things, the fact that aluminium is cheaper and easier to reach than calcium and magnesium, and also because it is more stable. Another reason is that if aluminium remains in the metal, it can be used as an alloying element for titanium-aluminium alloy which is an important alloy.

2.3.1 The CaO – TiO_2 Slag System

The CaO – TiO_2 phase diagram is seen in Fig. 2.20. In this system the following phases are present: CaO, $Ca_3Ti_2O_7$, $CaTiO_3$ and TiO_2. As seen from the diagram a slag with the composition of 82 wt% TiO_2 and 18 wt% CaO will have the lowest melting point at 1450 °C. During solidification of a slag with this composition, one $CaTiO_3$ phase and one TiO_2 phase will remain at room temperature.

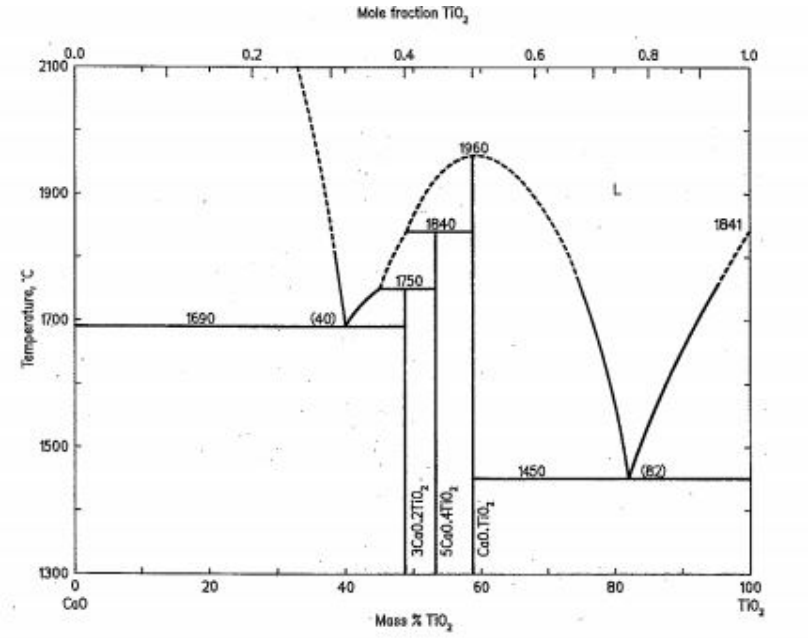

Figure 2.20: CaO – TiO_2 phase diagram [45].

2.3.2 The CaO – SiO_2 – TiO_2 Slag System

The CaO – SiO_2 – TiO_2 ternary phase diagram is presented in Fig. 2.21. In this system the following phases are present: CaO, TiO_2, SiO_2, Ca_3SiO_5, Ca_2SiO_4, $Ca_3Si_2O_7$, $CaSiO_3$, $CaTiO_3$, $Ca_3Ti_2O_7$ and $CaTiSiO_5$ [46].

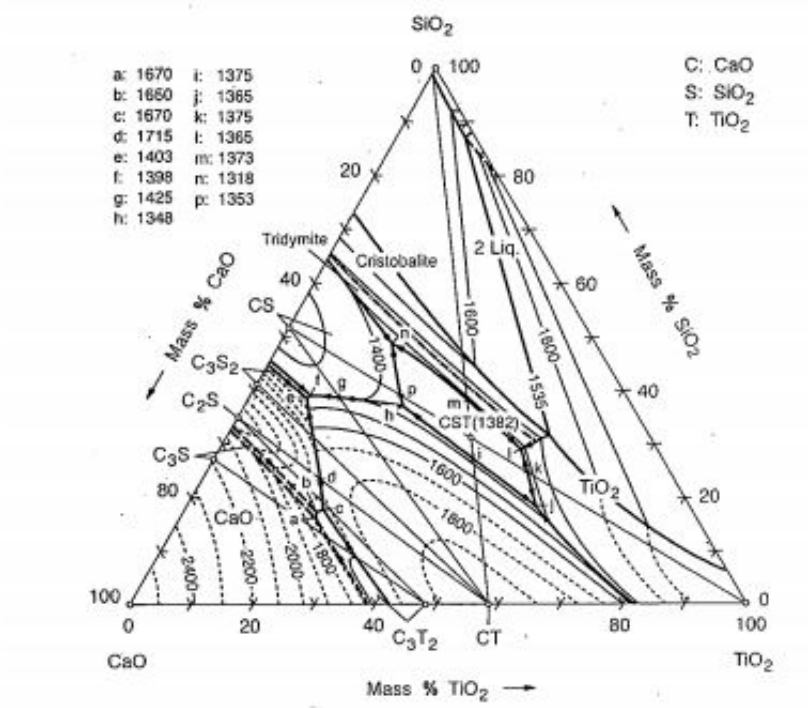

Figure 2.21: $CaO-SiO_2-TiO_2$ phase diagram [45].

It is generally known that SiO_2 is the main network-forming oxide in the structure of silicate melts [46]. In melts of the ternary system $CaO-TiO_2-SiO_2$, silicon oxide acts as the network-forming oxide, calcium oxide acts as the modifier of the network while titanium dioxide is characterized as an amphoteric oxide. Danek et al. [46] calculated the phase diagram of the system $CaO-TiO_2-SiO_2$ using the thermodynamic model of silicate melts. The needed thermodynamic data were taken from the literature and are summarized in Table 2.8. It should be mentioned that the liquidus curves of TiO_2 and SiO_2 were calculated under the assumption that $a_i = x_i$. The calculated phase diagram can be seen in Fig. 2.22.

Table 2.8: Temperatures and Enthalpies of Fusion of Pure Substances Used in the Calculation [46].

Compound	T_{fus}/K	$\Delta_{fus} H$/kJ mol^{-1}
CaO	2843	52.0
Ca_2SiO_4	2403	55.4
$CaSiO_3$	1817	56.0
$CaTiSiO_5$	1656	139.0
$Ca_3Ti_2O_7$	≈ 2070[1]	265.0[2]
$CaTiO_3$	2243	127.3[3]
TiO_2	2103	66.9
SiO_2	1986	9.6

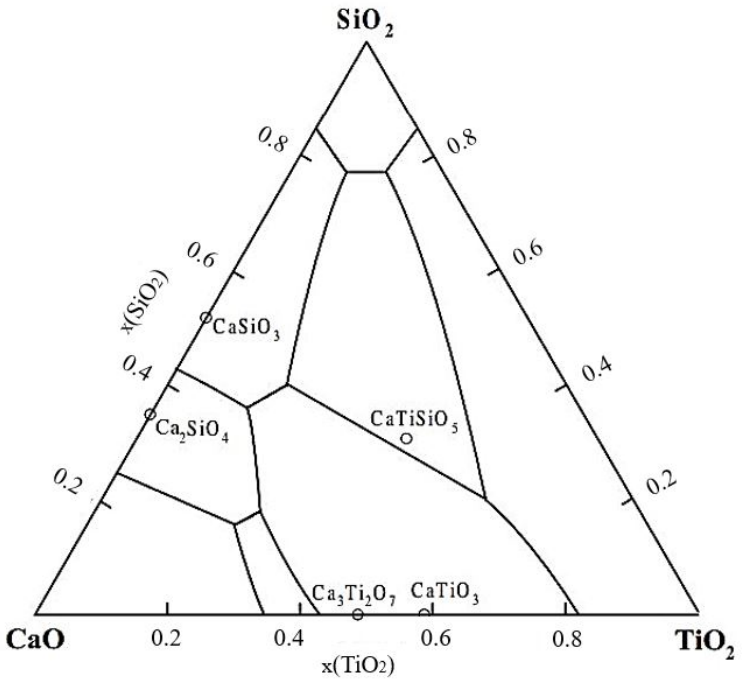

Figure 2.22: Calculated phase diagram of the system CaO–TiO_2–SiO_2 [46].

2.3.3 Ti-Al System

The Al-Ti phase diagram is presented in Fig. 2.23 and is the most important and by far most intensively investigated titanium phase diagram. The equilibrium solid phases present are (1) the terminal solid solutions of β-Ti and α-Ti, (2) Ti_3Al, (3) γ-TiAl, (4) $TiAl_2$ and δ phases, (5) $TiAl_3$ and (6) the Al terminal solid solution with a maximum Ti solubility of about 0.7 at% [47]. The TiAl (γ) phase forms through a peritectic reaction, L + β-Ti $\leftrightarrow$ γ at 1480 °C where the Al contents in the L, β-Ti and γ phases are 53, 47.5 and 51 at% respectively. According to the phase diagram and as mentioned in Section 2.1.2, Al strongly stabilizes the α phase and extends its domain of existence towards higher Al contents and higher temperatures.

[1] $T_{fus\,hyp}(Ca_3Ti_2O_7) \approx 2070\,K$, $\Delta_{fus}\,S(\text{atom}) \approx 10.7\,J\,mol^{-1}\,K$.
[2] $\Delta_{fus}\,H(Ca_3Ti_2O_7) \approx 12 \times \Delta_{fus}\,S(\text{atom}) \times T_{fus\,hyp}(Ca_3Ti_2O_7)$.
[3] $\Delta_{fus}\,H(Ca_3TiO_3) \approx T_{fus}(CaTiO_3) \times \Delta_{fus}\,S(MgTiO_3)$.

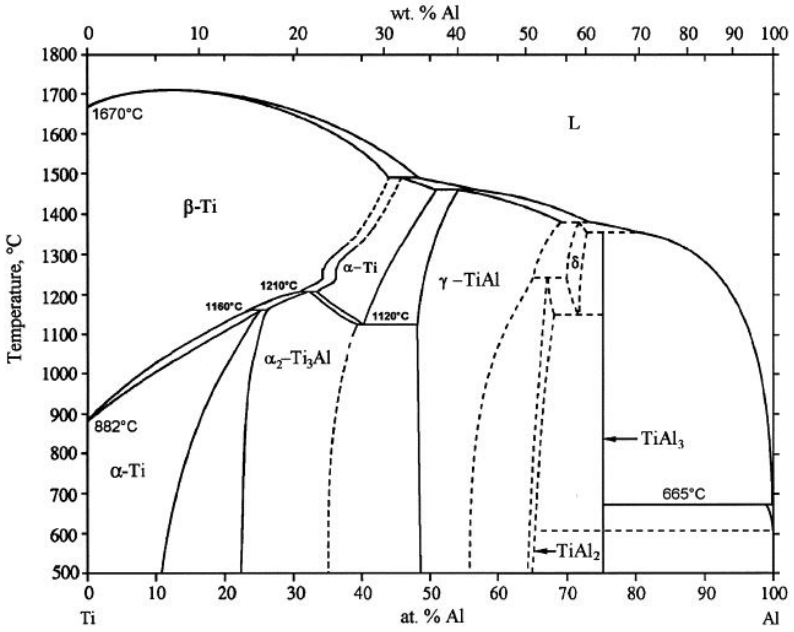

Figure 2.23: Ti-Al phase diagram [48].

2.3.4 Ti-O System

Another important system is the Ti-O system which is seen in Fig. 2.24. The system has following phases: liquid phase, β-Ti, α-Ti, α-TiO, Ti_3O_2, TiO, Ti_2O_3, Ti_3O_5, TiO_2 and Magneli phases included in the region between Ti_3O_5 and TiO_2 [49]. β-Ti possesses the bcc, α-Ti possesses the cph and the γ-TiO possesses the fcc. As can be seen from the figure, oxygen has a high solubility in α-Ti at low temperatures and thus stabilizes α-Ti with respect to the high temperature bcc form, β-Ti [47]. The diagram has two peritectic reactions, at 1770 °C and 1720 °C respectively. Four peritectoid reactions occur as well, at 600 °C, 500 °C, 940 °C and 920 °C. The maximum solubility of oxygen in β-Ti is 5.2 at% and about 34 at% in α-Ti. The intermediate phase, γ-TiO, extends between 43.5 at% to 55 at% oxygen at 1400 °C and from 48 at% to 55 at% oxygen at 800 °C [49]. Fischer [49] assessed the TiO binary system and compared the results with results assessed by Murray et al.[50], the results can be seen in Table 2.9.

The phase transformation between the different titanium oxides depends on its difficulty to rebuild a new structure from the previous one [6]. Crystalline structures of each titanium oxide can be seen in Table 2.10. Reduction from TiO_2 to Ti_2O_3 is relatively easy because the rutile structure is preserved and transformations do not need to be completely reconstructive, while the transformation from Ti_2O_3 to TiO is difficult because TiO has a face-centred cubic NaCl crystal structure [6].

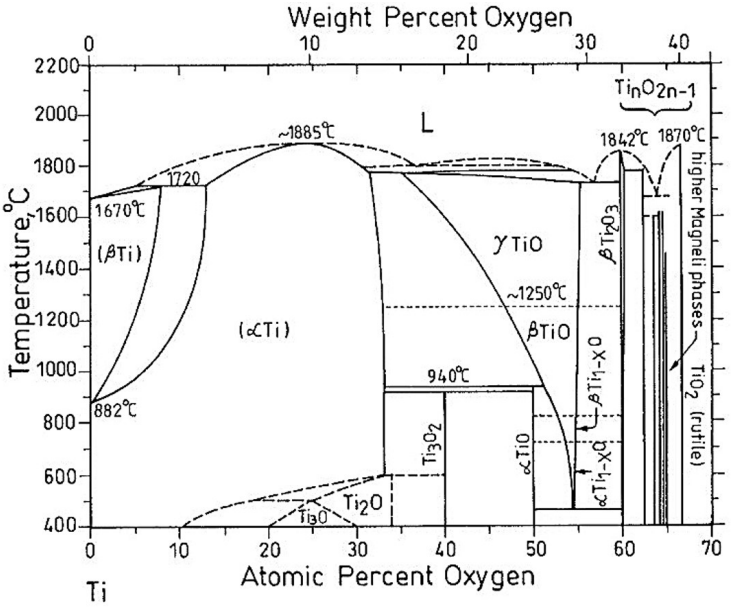

Figure 2.24: Ti-O binary phase diagram [47].

Table 2.9: Comparison betweem Invariant Equilibria Calculated in this optimization and those assessed by Murray et al. [49][50].

Reaction	Temperature °C	Composition at% Ti	Reference
$Liq \leftrightarrow TiO_2 + Ti_3O_5$	1691.80	33.3	Calculated
	1670.00	?	Murray [50]
$Liq \leftrightarrow Ti_3O_5 + Ti_2O_3$	1770.90	37.5	Calculated
	1770.00	37.5	Murray [50]
$Liq \leftrightarrow Ti_2O_3 + \gamma TiO$	1677.70	40.0	Calculated
	1720.0	40.2	Murray [50]
$Liq + \alpha Ti \leftrightarrow \gamma TiO$	1767.50	67.7	Calculated
	1770.0	68.6	Murray [50]
$Liq + \alpha Ti \leftrightarrow \beta Ti$	1726.40	87.0	Calculated
	1720±25	87.0	Murray [50]
$\gamma TiO + \alpha Ti \leftrightarrow TiO$	938.60	66.7	Calculated
	940.00	66.7	Murray [50]
$\gamma Ti \leftrightarrow TiO + Ti_2O_3$	460.33	40.0	Calculated
	460.00	40.0	Murray [50]

Table 2.10: Crystalline structure of each titanium oxide [6].

	Oxidation state	wt% O	Crystal structure
	TiO_2	40.03	Tetragonal
Magnéli phases	$Ti_{10}O_9$ to Ti_4O_7	37.5-36.8	Triclinic
	Ti_nO_{2n-1} $4 \leq n \leq 10$		
High titanium	TiO_3O_5	35.75	α, β, γ Monoclinic
oxide	Ti_2O_3	33.36	β Rhombohedra - α HCP
	TiO_x $0.7<x<1.3$	20.7-11.2	α Monoclinic - β Cubic - γ CCC
Solid solution	TiO_x $x<0.7$	<11.2	HCP

2.3.5 Ti-Si System

The Ti-Si phase diagram is seen in Fig. 2.25. As can be seen from the phase diagram, there are four fully stoichiometric silicide phases ($TiSi_2$, TiSi, Ti_5Si_4 and Ti_3Si) and one non-stoichiometric phase (Ti_5Si_3). Crystal structure data is shown in Table 2.11. Ti-Si alloys have excellent casting properties, including a low melting point, a narrow crystallization range, and good fluidity. The melting temperature of pure titanium lowers with an increase in the amount of silicon, as can be seen in Fig. 2.25, which facilitates the casting process [25]. Although pure titanium is easier to be oxidized compared to pure silicon, the activity coefficient of titanium in molten silicon is too small to allow Ti to be removed from molten silicon [51].

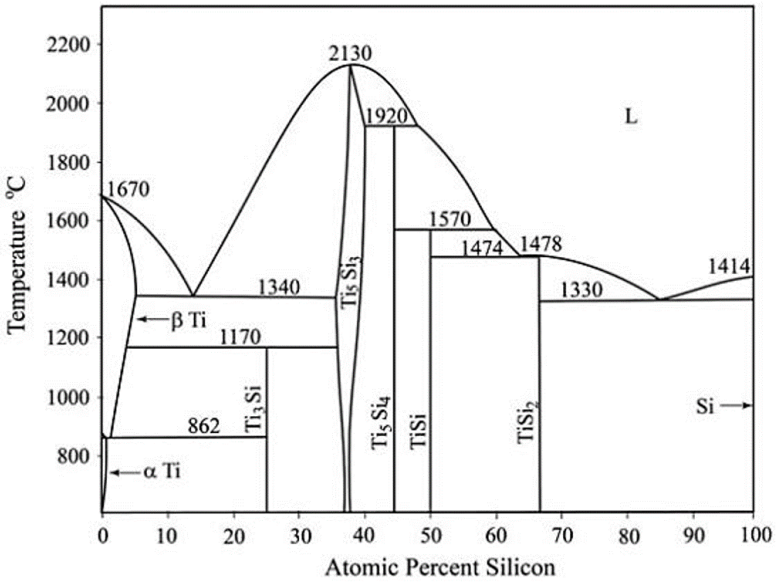

Figure 2.25: Ti-Si phase diagram [52].

Table 2.11: Ti-Si crystal structure data [53].

Phase	Composition at% Si
(α-Ti)	0 to 0.5
(β-Ti)	0 to 3.5
Ti_3Si	25
Ti_5Si_3	35.5 to 39.5
Ti_5Si_4	44.4
Ti_6Si_5	45.5
TiSi	50
$TiSi_2$	66.7
(Si)	100

The thermodynamic properties of titanium in molten silicon were studied by Ceccaroli et al. [51, p. 236]. The activity coefficient of titanium in molten silicon at infinite dilution relative to pure liquid titanium, ${\gamma^0}_{TiinSi}$ at 1723 K was found to be 4.48×10^4. Also, the self-interaction parameter of titanium in molten silicon was determined and shown to hold 3.97 at 1723 K. The same results were obtained in a study done by Miki et al. [54] as well. The activity coefficient at infinite dilution and self-interaction coefficient of titanium in molten silicon and the Gibbs energy change of silicon-titanium mixing relative to pure liquid silicon and titanium at 1723 K were determined as follows and presented in Fig. 2.26:

$$ {\gamma^0}_{Ti(l)inSi} = 4.48 \times 10^4, {\epsilon^{Ti}}_{TiinSi} = 3.97 $$

$$ \Delta {G^M}_{Si-Ti} = -188\,\mathrm{X}_{Ti} + 512\,{\mathrm{X}^2}_{Ti} - 1720\,{\mathrm{X}^3}_{Ti}\,(\mathrm{kJ\,mol^{-1}})\,(\mathrm{X}_{Ti} < 0.1) $$

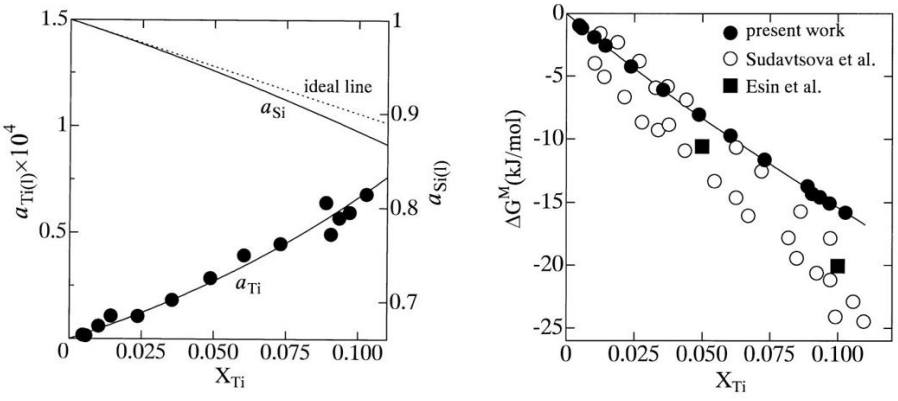

Figure 2.26: Results from [54]. Activities of titanium and silicon in molten silicon relative to pure liquid titanium and silicon at 1723 K to the left, and the free energy change of mixing for silicon-titanium solution relative to pure liquid titanium and silicon at 1723 K to the right.

2.3.6 Al-Si-Ti System

Pierre Perrot [55] studied the Ti-rich corner in the Aluminium-Silicon-Titanium system. The system is shown in Fig. 2.27 with the reactions presented in Fig. 2.28. Perrot reported a tree phase equilibrium, (α-Ti, Ti_3Al + Ti_3Si) at 700 °C which was calculated from the thermodynamic assessments of Ti−Si and Ti−Al systems. Some of the phases observed in the phase diagram are as well presented in Table 2.12. The Ti-Al-Si system is characterized by wide homogeneity regions of a few binary compounds. However, up to now, most of the available data concern the Ti-rich corner of the Al-Si-Ti system, information on phase equilibria at other concentrations are limited [56][57].

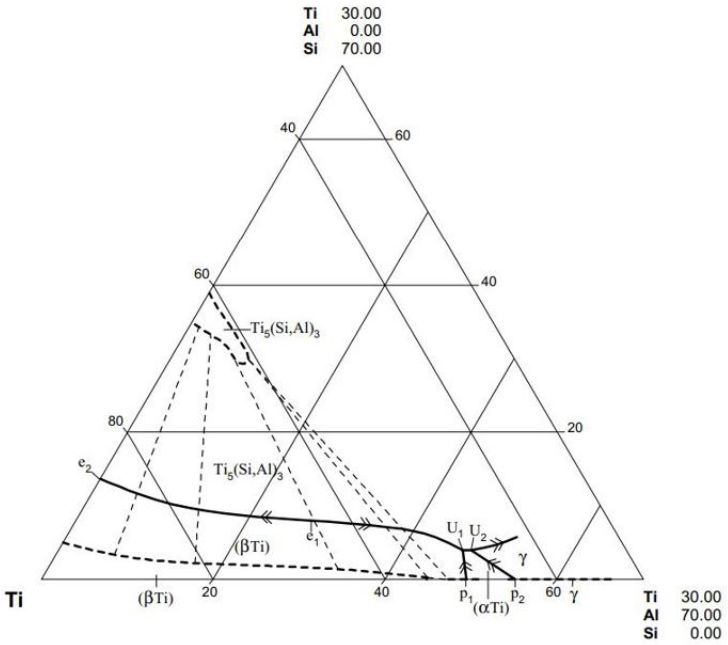

Figure 2.27: Liquidus and solidus surfaces in the Ti-rich corner. Solidus is shown by dashed lines. Taken from [55].

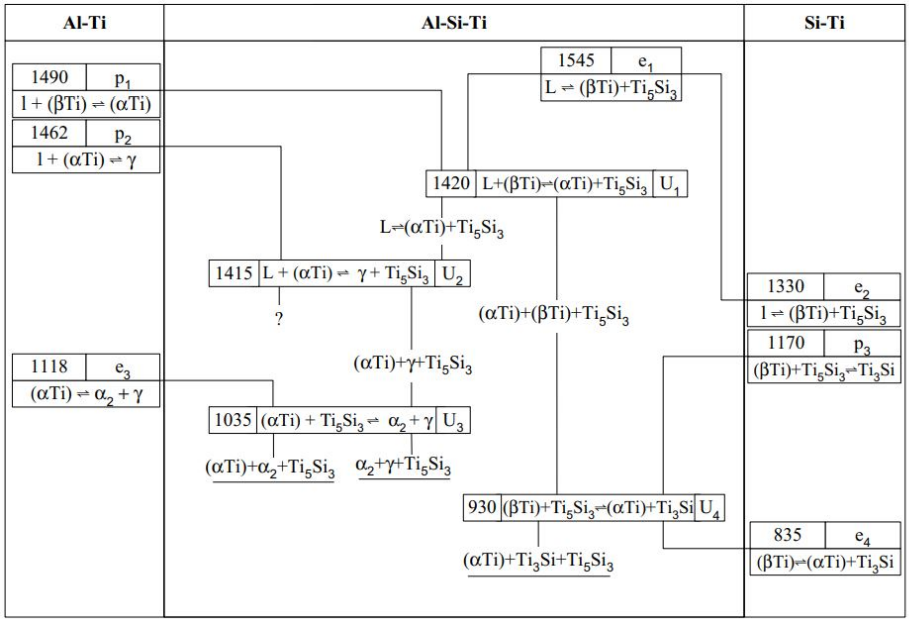

Figure 2.28: Partial reaction scheme from [55].

Table 2.12: Some phases in the Al-Si-Ti system from [55].

Phase	**Composition** (at%)		
	Al	Si	Ti
βTi	33	1	66
Ti_5Si_3	10-15	20-25	60-65
αTi	48	0.5	51.5
γ	48	0.8	51.2
$\tau 1$ ($Ti_7Al_5Si_{12}$)	20.8	50	29.2

Chapter 3

Experimental Work

In this chapter, an overview of the raw materials is given as well as the experiments carried out and the experimental equipment used during the experiments. Preparation of samples and analyzing techniques such as SEM, EDS, EPMA, XRF, and XRD are also given.

The experiments were carried out in an induction furnace (IF75) and a vacuum induction furnace (Blue Furnace).

The induction furnace is an open induction furnace with a maximum power supply of 75 kW and manual heating control.

The vacuum induction furnace is a closed furnace with a temperature limit at 2000 °C, manual heating control, and a maximum effect of 10 kW. The residual air in the furnace is displaced before running experiments by flushing with argon gas.

The slags were made in the induction furnace while the aluminothermic reduction experiments were performed in the vacuum induction furnace.

3.1 Slag Preparation

3.1.1 Raw Materials

The raw materials used were provided by Alfa Aesar. TiO_2, CaO and SiO_2 powders were used to make the slags.
The TiO_2 powder had a purity of 99.5 %, density of 4.23 kg m^{-3} and a melting point in the range of 1830 °C to 1850 °C. It was in the form of 1 µm to 2 µm APS Powder. Total metal impurities were 0.5 % max.
The SiO_2 used had as well a purity of 99.5 %, melting point at 1710 °C and was in the form of <10 µm APS Powder.
The CaO used had a high purity (reagent grade), density of 3.37 kg m^{-3} and melting point at 2572 °C. Trace element as Pb was 0.01 % max.

3.1.2 Setup

An induction furnace was used to make the slags. The setup is seen in Fig. 3.1. A graphite crucible with a height of 40 cm and an inner diameter of about 11.5 cm was used. The graphite tube with the thermocouple was used to measure the temperature and used to stir the mixture during the heating. The graphite crucible and the graphite tube were painted with boron nitride before the experiments to avoid reaction between TiO_2 and the graphite.

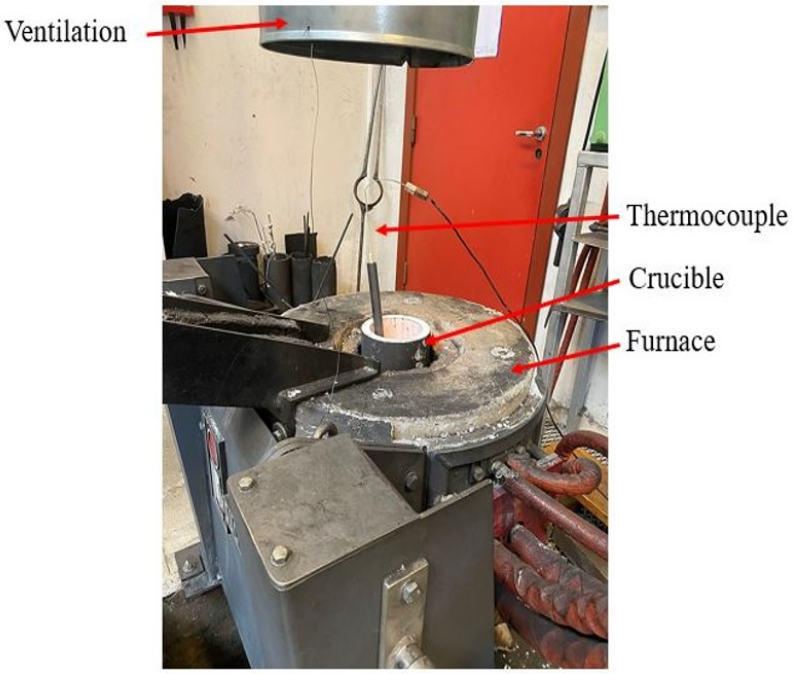

Figure 3.1: Setup of the slag preparation done in the IF75.

3.1.3 Procedure

The powders were weighed out in the crucible before placed into the furnace, the composition of the slags, as well as the phase diagrams with the estimated slag compositions, are seen in Table 3.1 and Fig. 3.2. The furnace was then heated to the temperature where the mixture was completely melted. Once the mixture was melted, it was cast and cooled completely before it was crushed. The crushed slag was then remelted, cast, and crushed again to get a more homogeneous slag. The procedure can be seen in Fig. 3.3 and Fig. 3.4 while the melting and remelting profiles can be seen in Appendix A.1 and Appendix A.2.

XRF-analysis was conducted on the prepared slags. The compositions from the analysis are presented in Table 3.2. The instrument used was a BRUKER S8 Tiger 4 kW X-ray spectrometer.

Table 3.1: Target composition of the slags produced.

nr.	TiO_2 wt%	CaO wt%	SiO_2 wt%
1	82	18	-
2	25	50	25

Table 3.2: Compositions of the actual produced slags after measured by XRF.

Element (%)	CaO-TiO_2	CaO-SiO_2-TiO_2
TiO_2	86.10	29.30
CaO	15.07	43.54
Al_2O_3	0.29	0.56
Fe_2O_3	0.27	0.12
SiO_2	0.22	27.73
MgO	0.14	0.37
P_2O_5	0.05	not detected
Cr_2O_3	0.04	0.02
ZrO_2	0.04	0.01
Nb_2O_5	0.02	not detected
CuO	0.02	not detected
NiO	0.01	0.05
SrO	not detected	0.02

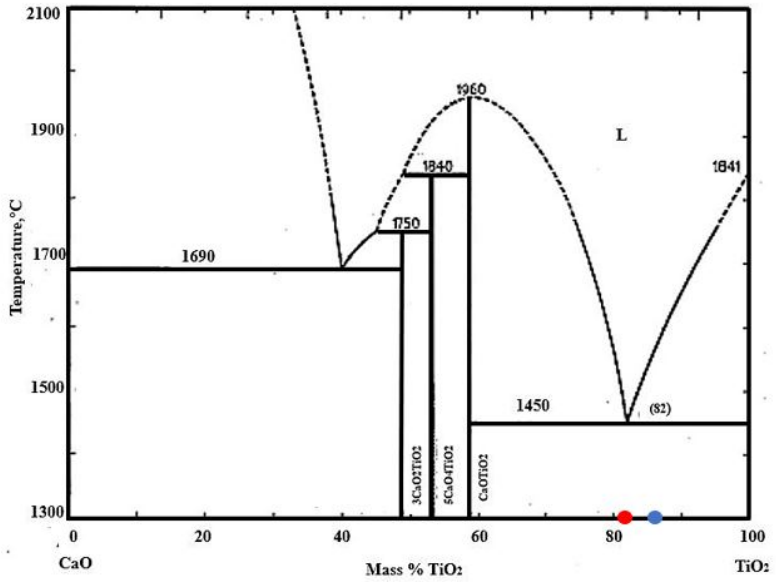

(a) Slag 1.

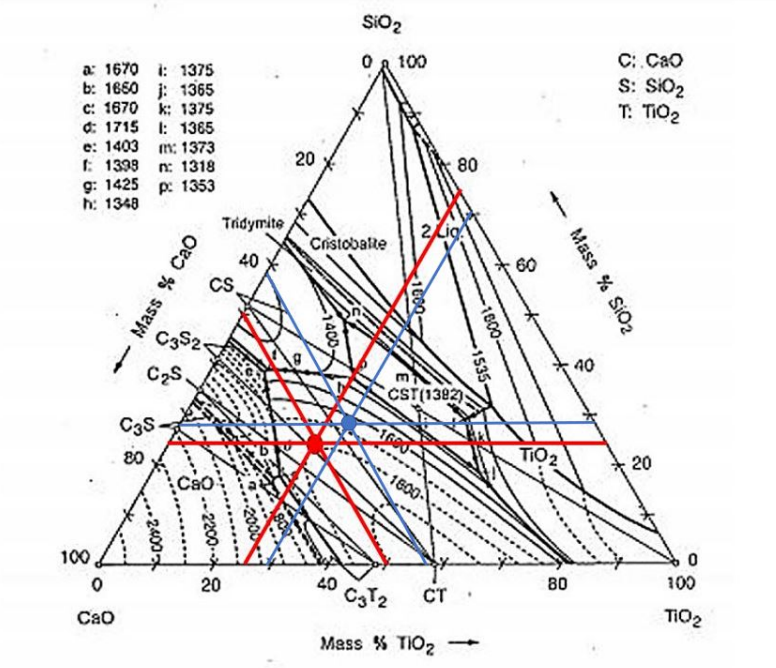

(b) Slag 2.

Figure 3.2: Estimated and measured slag compositions. Targeted in red and measured in blue.

(a) Melting procedure (b) Casting procedure (c) Crushing procedure

Figure 3.3: Slag preparation procedure of slag 1, melting, casting and crushing.

(a) Melting procedure (b) Casting procedure (c) Crushing procedure

Figure 3.4: Slag preparation procedure of slag 2, melting, casting and crushing.

3.2 Aluminothermic Reduction

3.2.1 Raw Materials

The raw materials were slags from the slag preparation and Aluminium. The Aluminium metal used came from molten salt electrolysis, with a purity of 99.8 %. 12 experiments were performed in total seen in Table 3.4. The weight of the metal for each experiment was selected based on Eq. (3.1), Eq. (3.2) and Table 3.3. The target slag compositions were as well used in the calculations, and not the actual slag compositions measured by XRF. For the slag with target composition 18 wt%CaO and 82 wt%TiO_2 it was assumed that 100 g of slag contained approximately 82 g of TiO_2. Meaning that to get 100 % reduction of TiO_2 36.94 g of Al had to be added to the slag, Eq. (3.3). For the slag with target composition 50 wt%CaO, 25 wt%SiO_2 and 25 wt%TiO_2 it was assumed that 100 g of slag contained approximately 25 g of SiO_2 and 25 g of TiO_2. Meaning that to get 100 % reduction of both TiO_2 and SiO_2 a total of 26.23 g of Al had to be added to the slag, Eq. (3.4) showing the amount needed to reduce the total amount of TiO_2 and Eq. (3.5) showing the amount needed to reduce the total amount of SiO_2. The molar ratio Al/TiO_2 for the experiments with the CaO – TiO_2 slag is seen in Table 3.5.

$$3\,SiO_2 + 4\,Al = 3\,Si + 2\,Al_2O_3 \tag{3.1}$$

$$3\,TiO_2 + 4\,Al = 3\,Ti + 2\,Al_2O_3 \tag{3.2}$$

Table 3.3: Molar masses of the elements.

Element	Molar mass ($g\,mol^{-1}$)
4Al	107.924
O	15.999
3Si	84.258
3Ti	143.601
$2Al_2O_3$	203.92
$3SiO_2$	180.252
$3TiO_2$	239.595

$$\frac{82\,g \times 107.926\,g\,mol^{-1}}{239.595\,g\,mol^{-1}} = 36.94\,g \tag{3.3}$$

$$\frac{25\,g \times 107.926\,g\,mol^{-1}}{239.595\,g\,mol^{-1}} = 11.26\,g \tag{3.4}$$

$$\frac{25\,g \times 107.926\,g\,mol^{-1}}{180.252\,g\,mol^{-1}} = 14.97\,g \tag{3.5}$$

Table 3.4: Experiments with metal and slag.

Slag	Amount of slag (g)	Amount of Al (g)	Temperature (°C)	Holding time (min)
18CaO-82TiO_2	100	36.94	1550	60
18CaO-82TiO_2	100	29.55	1550	60
18CaO-82TiO_2	100	44.33	1550	60
18CaO-82TiO_2	100	36.94	1650	60
18CaO-82TiO_2	100	29.55	1650	60
18CaO-82TiO_2	100	44.33	1650	60
50CaO-25SiO_2-25TiO_2	100	26.23	1550	60
50CaO-25SiO_2-25TiO_2	100	20.98	1550	60
50CaO-25SiO_2-25TiO_2	100	31.48	1550	60
50CaO-25SiO_2-25TiO_2	100	26.23	1650	60
50CaO-25SiO_2-25TiO_2	100	20.98	1650	60
50CaO-25SiO_2-25TiO_2	100	31.48	1650	60

Table 3.5: Molar ratio Al/TiO_2.

Molar ratio Al/TiO_2	Added TiO_2 (g)	Added Al (g)
1.08	82	30
1.34	82	37
1.59	82	44

3.2.2 Setup

The aluminothermic reduction experiments were performed in a vacuum induction furnace. The setup is shown in Fig. 3.5. As can be seen, two crucibles were used during the experiments. This was done due to the risk of TiO_2 reacting with the graphite crucible. The slag and the metal were therefore placed into a small crucible, which was put in a larger crucible, as seen in Fig. 3.5b. The dimensions of the two crucibles are seen in Fig. 3.6 and Fig. 3.7.

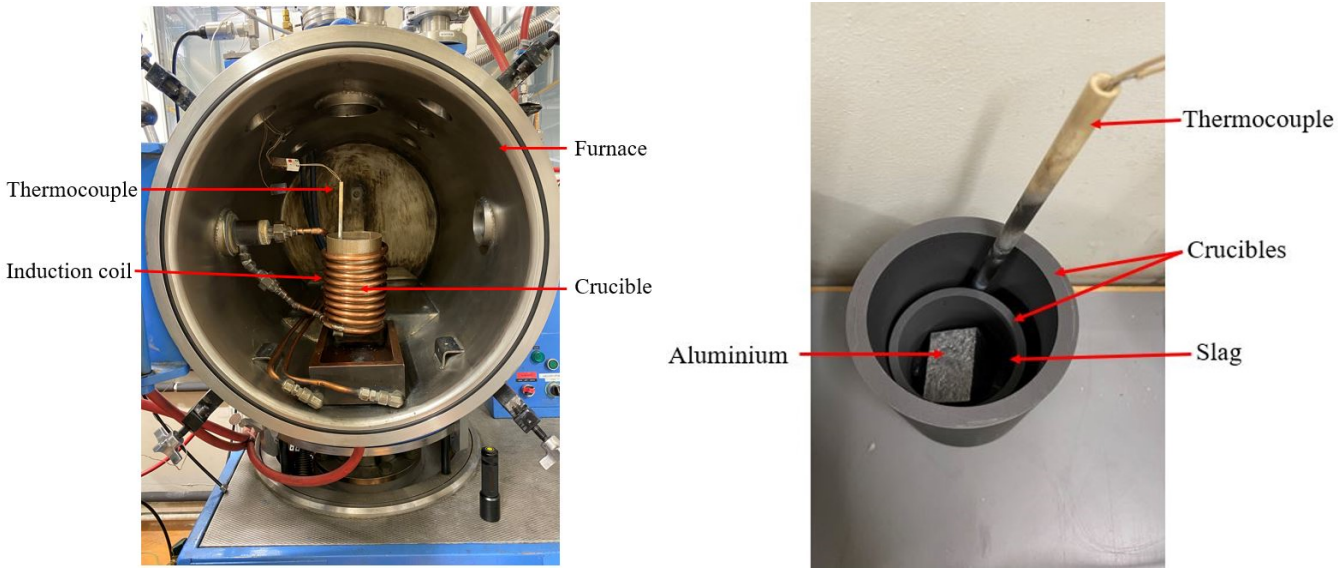

(a) The Blue Furnace (b) The setup of the crucibles

Figure 3.5: Setup of the experiments done in the vacuum induction furnace.

Figure 3.6: Height and diameter of the large crucible used in the vacuum induction furnace.

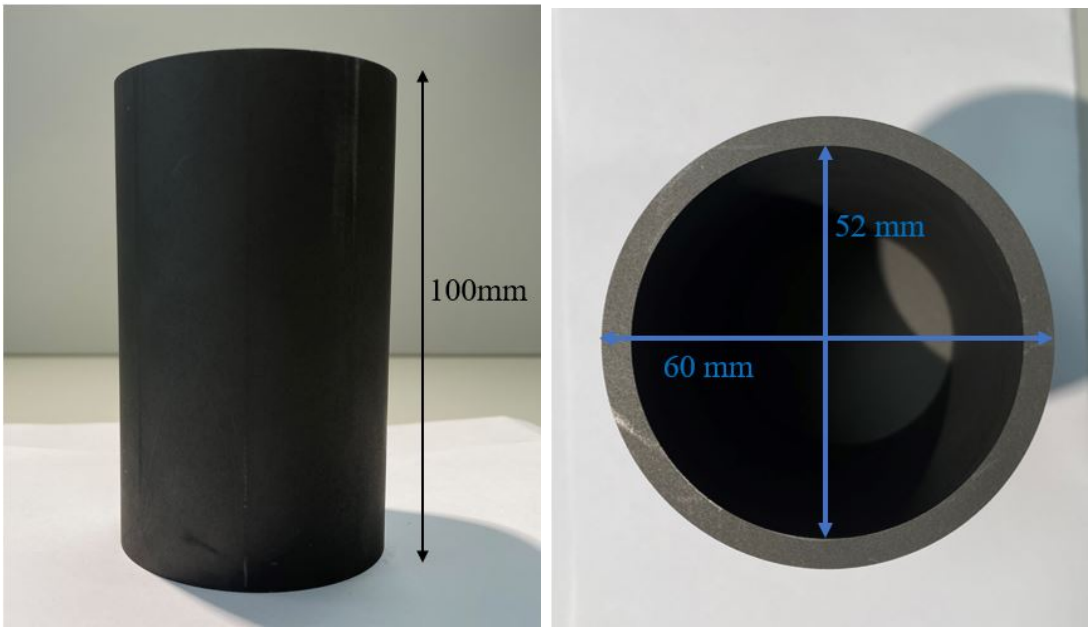

Figure 3.7: Height and diameter of the small crucible used in the vacuum induction furnace.

3.2.3 Procedure

After the crucibles were inserted into the furnace, the furnace was evacuated to at least 3×10^{-3} mbar and flushed with argon three times and then filled with argon with a purity of 5N or 6N. The furnace was then heated until the thermocouple read approximately 1550 °C or 1650 °C, depending on which experiment performed. After reaching the holding temperature, it was kept constant for 1 h by controlling the power. After 1 h, the power was switched off, and the crucibles were allowed to cool down before taking out from the furnace. The heating and cooling rates for each experiment can be seen in Appendix B.1 and Appendix B.1.

3.2.4 Sampling and Analysing

The reacted slag and metal after the experiments were cut and cast in Struers EpoFix. Both slag and metal were tried to be included from each experiment, but some crucibles were more challenging to cut than others depending on the amount of slag and metal and how well mixed it was after the remelting. The samples were subsequently ground with MD-Piano 220 and polished with 9 µm, 3 µm and 1 µm. Metal and slag samples from experiment 11 are seen in Fig. 3.8.

The resulting samples were studied using SEM, EDS, EPMA, and XRD.
The samples were degassed at 65 °C overnight before use in SEM, EDS, and EPMA. SEM- and EDS scans were taken using a LVFESEM Zeiss Supra. 55 VP. An aperture diameter of 120 µm, high current, working distance between 8 mm to 11 mm and a voltage at 15 V were used during the scans. The SEM

mode used was the detection of secondary electrons originating from the surface of the sample, providing detailed surface information. Point analyses were used during EDS measurements.
EPMA measurements were performed by Senior Engineer Morten Peder Raanes. Three analyses were performed on each phase in each sample.
Some samples prepared for SEM, EDS, and EPMA are seen in Fig. 3.9. Covering with aluminium foil was done to avoid overcharging of the epoxy, while the carbon tape was ensuring conductivity between the foil and the sample. In addition, the surface was sprayed with carbon before EPMA.

The resulting slag from experiments with slag 1 was analyzed with XRD. The reacted slag was separated from the crucibles and the metal, then crushed to fine powders in a ring mill in a tungsten carbide chamber. XRD analyses were performed by Laurentius Tijhuis. The instrument used was a BRUKER D8 ADVANCED, and the samples were analyzed from 2θ values between 3-80 with a step size of 0.01. The phases were identified with DIFFRAC.EVA using the PDF 4+ database, and quantified using the Rietveld method in the Topas software.

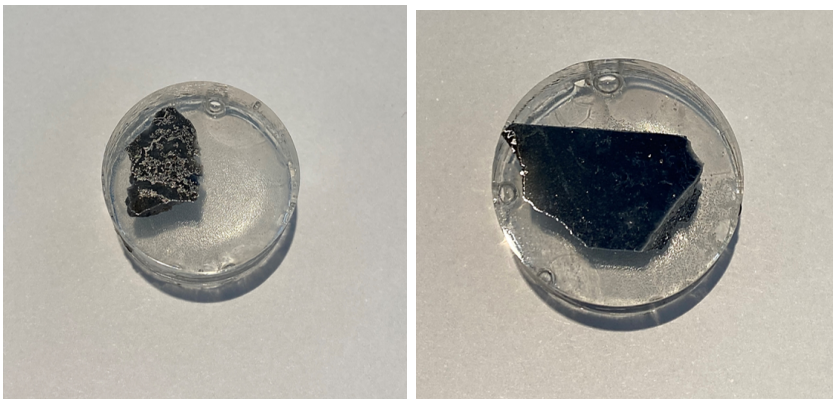

Figure 3.8: Samples cast, ground and polished.

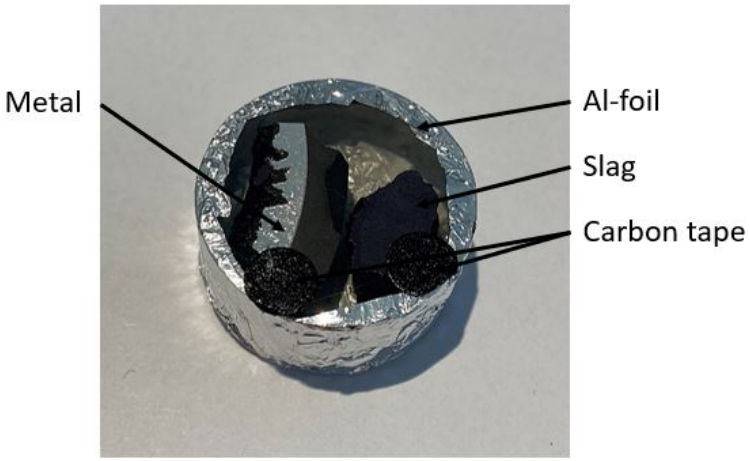

Figure 3.9: Samples prepared for SEM.

Chapter 4

Results

In this chapter, figures of the reacted slag and the reacted metal are presented, as well as the calculated results from FactSage and results from XRD analysis.

SEM scans, EPMA scans, EPMA measurements, and thermodynamic calculations are presented, while EDS measurements can be found in Appendix C and Appendix D. Thermodynamic calculations on the experiments were performed using the thermodynamic software FactSage. The phase transitions upon cooling calculated with FactSage for slag 2 are presented in Appendix F. XRD analysis were done using the program TOPAS.

4.1 Results from experiments with $CaO-TiO_2$ slag

The results from the experiments with slag 1 are presented in this section. The crucibles after cutting are shown and compared. SEM images, EPMA scans and analysis of the reacted slag, and metal are presented, and EDS analysis from SEM scans are included in Appendix C. The area where the SEM scans have been done is pointed out in experiments 1, 3, 4, and 6 as red squares. XRD results from each experiment are shown as well.

4.1.1 Visual inspection of the cut crucibles

The cross sections of the cut crucibles from the experiments are shown in the following figures. Important observations are summarized in these key points:

1. A change in the color of the slag is seen when the temperature is increased from 1550 °C to 1650 °C, from black to bronze.
2. The metal after reduction is located close to the walls and the bottom of the crucibles, making it difficult to separate it from the crucible.
3. It looks like the mixing of the metal and slag are better at higher temperatures.

The crucibles from experiments 1 and 4 with 100 g $CaO-TiO_2$ and 37 g and 36.5 g Al are seen in Fig. 4.1. Slag is detected as the black area while the formation of metal is seen as the silver colored area. A change in the color, from black to bronze, of the slag can be seen from experiment 1 to experiment 4, as well as the amount of metal seen in the cross-section of the crucibles.

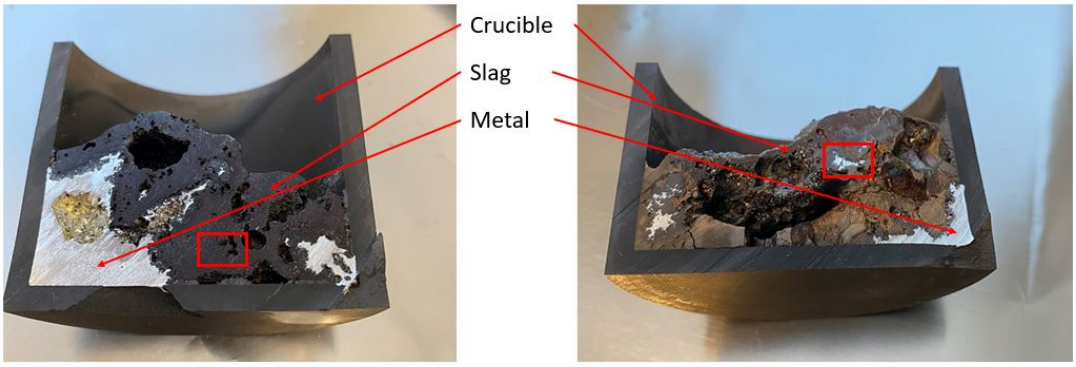

Figure 4.1: Cross-section from experiments 1 and 4 at 1550 °C and 1650 °C.

The crucibles from experiments 2 and 5 with 100 g $CaO-TiO_2$ and 30 g and 30.5 g Al are seen in Fig. 4.2. Also here, a change in the color of the slag is seen. However, the amount of metal seems to be the same, but much more mixed in experiment 5.

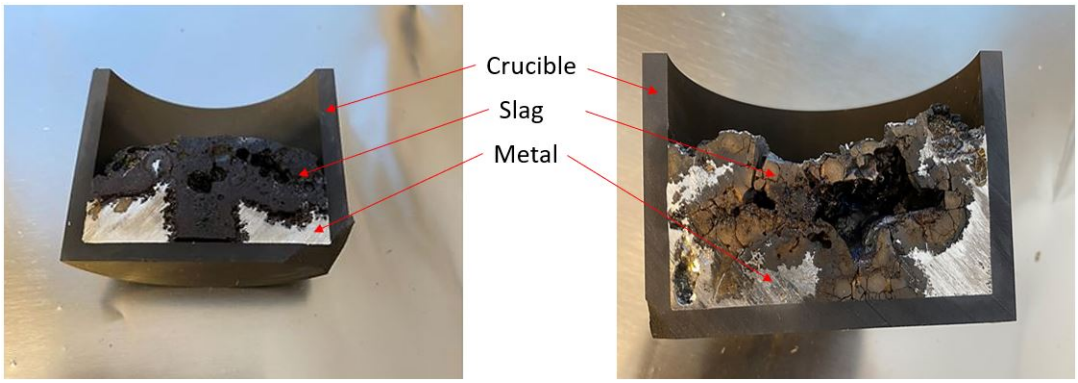

Figure 4.2: Cross-section from experiments 2 and 5 at 1550 °C and 1650 °C.

The crucibles from experiments 3 and 6 with 100 g slag and 43 g and 44 g Al are seen in Fig. 4.3. The same change in color of the slag is seen and also here the amount of metal seems to be higher in the cross-section of the crucible from experiment 6. The mixing seems to have been much better in experiment 6 as well.

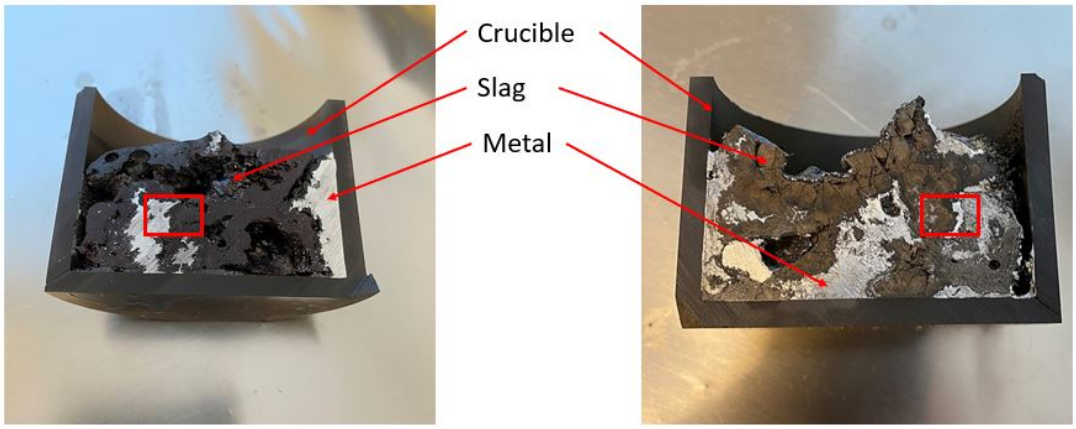

Figure 4.3: Cross-section from experiments 3 and 6 at 1550 °C and 1650 °C.

4.1.2 Results from SEM and EPMA

In this section SEM images, EPMA scans and measurements from the reacted slag and metal are presented. EDS measurements of the points in the SEM scans are shown in Appendix C. In the EPMA analysis three analysis were performed for each phase in each sample as can be seen from the scans and the analysis. The contrast in the SEM scans has been improved to get a more precise look at the different phases.

The overall observations from the analysis are summarized in these key points:

1. Three different phases are observed in the reacted slag, a TiO_2 rich phase, a TiO_2-CaO phase and a $CaO\text{-}Al_2O_3$ phase.
2. The reacted metal is homogeneous, and most likely pure Al with some Al_2O_3 by looking at the EDS analysis.
3. The content of TiO_2 in the reacted slag is high, especially in the TiO_2 rich phase.
4. A change in the microstructure is seen when the temperature is increased from 1550 °C to 1650 °C, with smaller phases observed at higher temperatures.
5. The high content of TiO_2 in the reacted slag implies that no reduction of TiO_2 to Ti has occurred.
6. EPMA analysis are presented in tables with the calculated standard deviations for each phase. Small deviations are observed and the measured content of Al_2O_3, CaO and TiO_2 are quite similar. However, some deviations are observed in the analysis from experiment 3.

SEM images and EPMA analysis from experiment 1 are seen in Fig. 4.4, Fig. 4.5 and Table 4.1. The reacted metal is homogeneous and the white spots are assumed to be Al_2O_3 from the EDS analysis seen in Table C.1. Different phases in the reacted slag are seen in the SEM scan, and more clearly in the EPMA scan. As can be seen, the amount of the $CaO\text{-}Al_2O_3$ phase (black area), with a relatively high content of Al_2O_3, is quite small compared to the TiO_2 rich phase (the white area) and the $CaO-TiO_2$ rich phase (grey area).

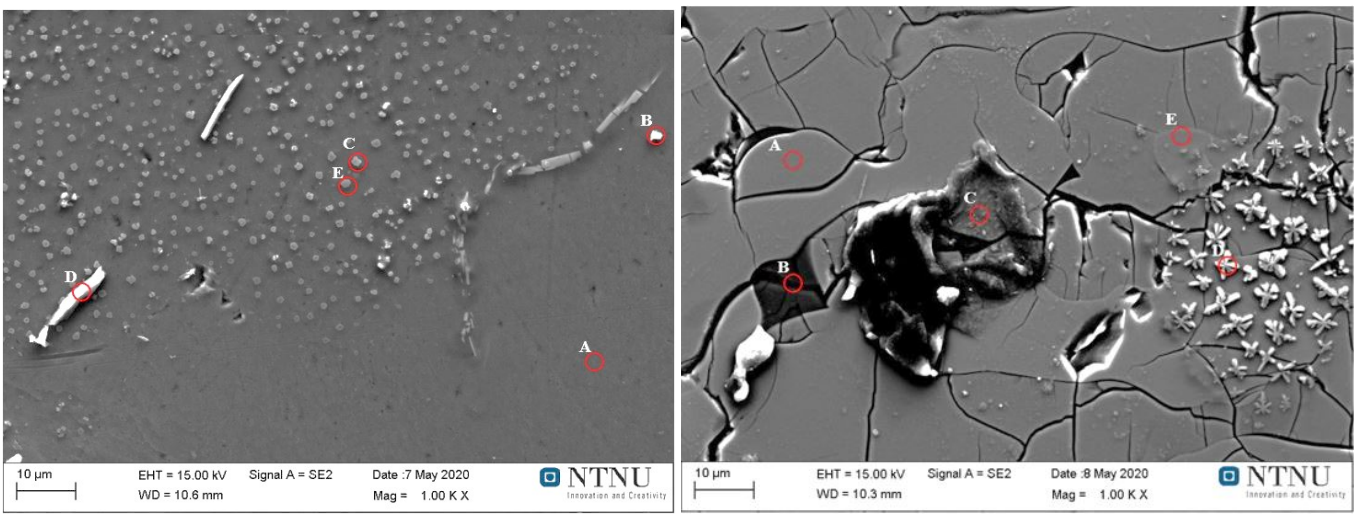

(a) Metal, homogeneous phase.

(b) Slag, different phases observed.

Figure 4.4: SEM images of the reacted metal and slag from experiment 1.

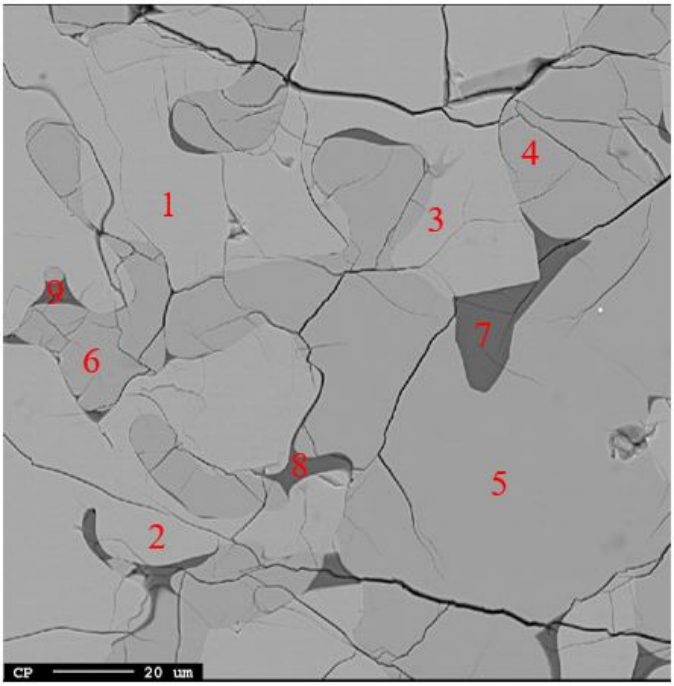

Figure 4.5: EPMA scan of the reacted slag from experiment 1.

Table 4.1: EPMA measurements of points in Fig. 4.5.

Point	Al_2O_3 mass%	CaO mass%	TiO_2 mass%	Phase
1	1.325 ±0.01	0.904 ±0.07	99.562 ±0.05	TiO_2
2	1.298 ±0.01	0.788 ±0.07	99.939±0.05	TiO_2
3	1.302 ±0.01	0.735 ±0.07	99.678±0.05	TiO_2
4	0.115 ±0.02	42.127±0.02	52.863 ±0.03	$CaO-TiO_2$
5	0.144 ±0.02	42.107±0.02	53.505±0.03	$CaO-TiO_2$
6	0.154 ±0.02	42.150±0.02	53.118 ±0.03	$CaO-TiO_2$
7	37.455±0.18	29.950±0.09	4.774 ±0.21	$CaO-Al_2O_3$
8	37.199±0.18	30.115±0.09	5.208±0.21	$CaO-Al_2O_3$
9	37.629±0.18	29.913±0.09	4.760±0.21	$CaO-Al_2O_3$

SEM images and EPMA analysis from experiment 3 are seen in Fig. 4.6, Fig. 4.7 and Table 4.2. The reacted metal is homogeneous with no grain boundaries. The white spots are again assumed to be Al_2O_3 from the high content of O and Al seen from the EDS analysis in Table C.3. Different phases in the reacted slag are seen both in the SEM image and in the EPMA scan, a TiO_2 rich, a $CaO-TiO_2$ phase and a $CaO-Al_2O_3$ phase. Again, the amount of TiO_2 rich phase and the $CaO-TiO_2$ phase is highest with high contents of TiO_2 and CaO. The CaO-Al_2O_3 rich phase has a low content of TiO_2. It should be noticed that the standard deviations are quite high from these analysis. The reason for this is not known, but this will be discussed further in the next chapter.

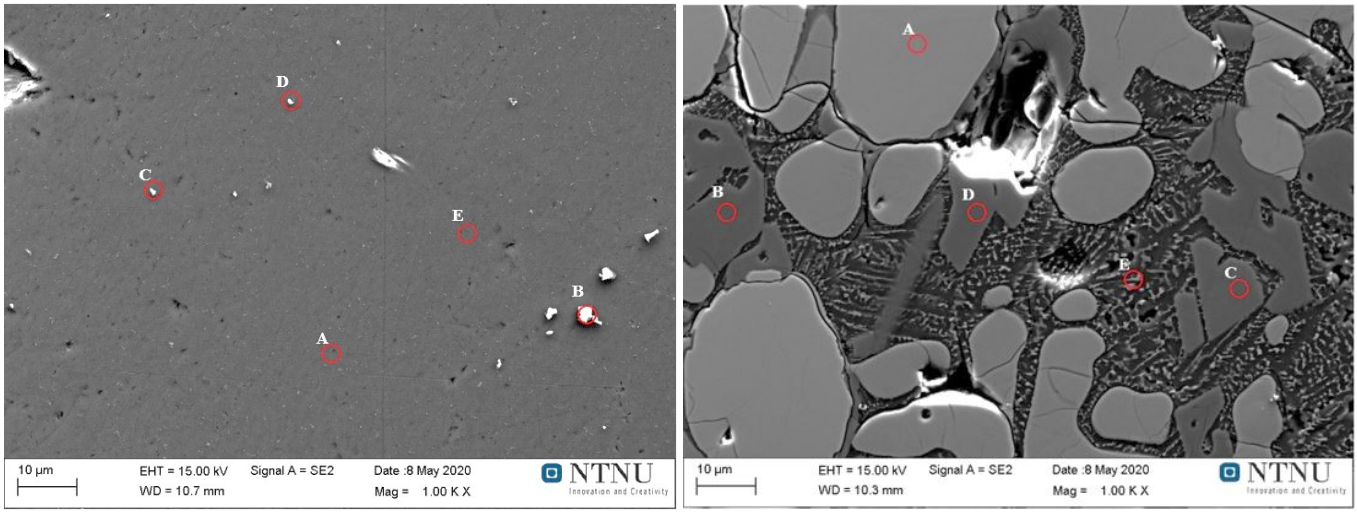

(a) Metal, homogeneous phase.

(b) Slag, different phases observed.

Figure 4.6: SEM images of the reacted metal and slag from experiment 3.

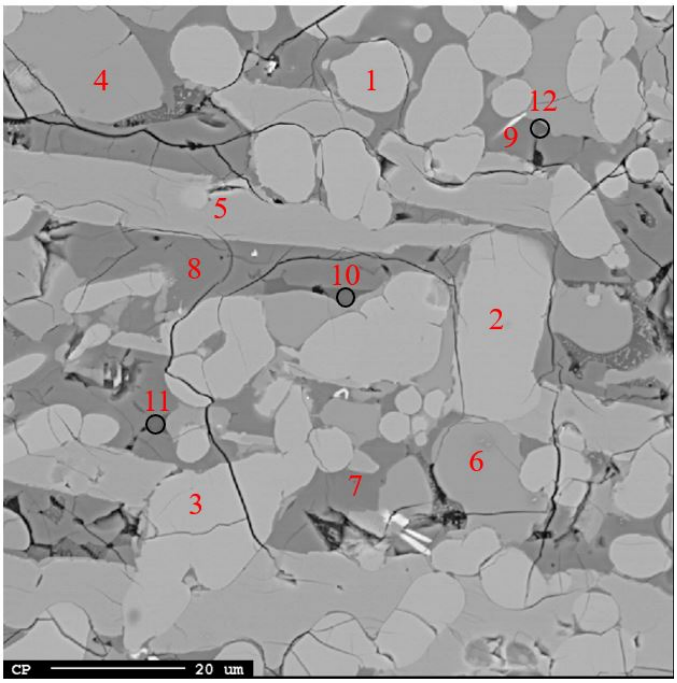

Figure 4.7: EPMA scan of the reacted slag from experiment 3.

Table 4.2: EPMA measurements of points in Fig. 4.7.

Point	Al_2O_3 mass%	CaO mass%	TiO_2 mass%	Phase
1	2.979 ±19.01	1.482±6.62	104.612±28.27	TiO_2
2	2.973 ±19.01	1.491±6.62	104.824±28.27	TiO_2
3	42.839±19.01	15.536±6.62	44.759 ±28.27	TiO_2
4	2.311 ±0.14	42.027±19.00	52.147±21.94	CaO – TiO_2
5	2.348 ±0.14	1.467±19.00	98.988±21.94	TiO_2
6	2.032 ±0.14	41.530±19.00	52.760±21.94	CaO – TiO_2
7	44.954±14.74	16.645±6.60	42.513±8.70	mixed
8	44.617±14.74	16.152±6.60	44.346±8.70	mixed
9	13.517±14.74	30.401±6.60	61.816±8.70	CaO – TiO_2
10	58.197±2.09	34.259±2.65	9.547 ±2.31	CaO – Al_2O_3
11	57.586±2.09	35.969±2.65	8.452 ±2.31	CaO – Al_2O_3
12	53.485±2.09	29.497±2.65	13.797±2.31	CaO – Al_2O_3

SEM images and EPMA analysis from experiment 4 are seen in Fig. 4.8, Fig. 4.9 and Table 4.3. Some overcharging is observed in the SEM image of the slag, due to epoxy in the pores because of the porous slag, and this makes it difficult to see the different phases. Still they are seen in the EPMA scan. The

TiO_2 rich phase and the CaO – TiO_2 phase are dominant in the slag, while the CaO-Al_2O_3 phase with a high content of Al_2O_3 is small when comparing. As for the other experiments, a decrease in the content of TiO_2 is seen comparing the CaO – TiO_2 phase and the CaO-Al_2O_3 phase with the TiO_2 rich phase with a corresponding increase in the content of Al_2O_3.

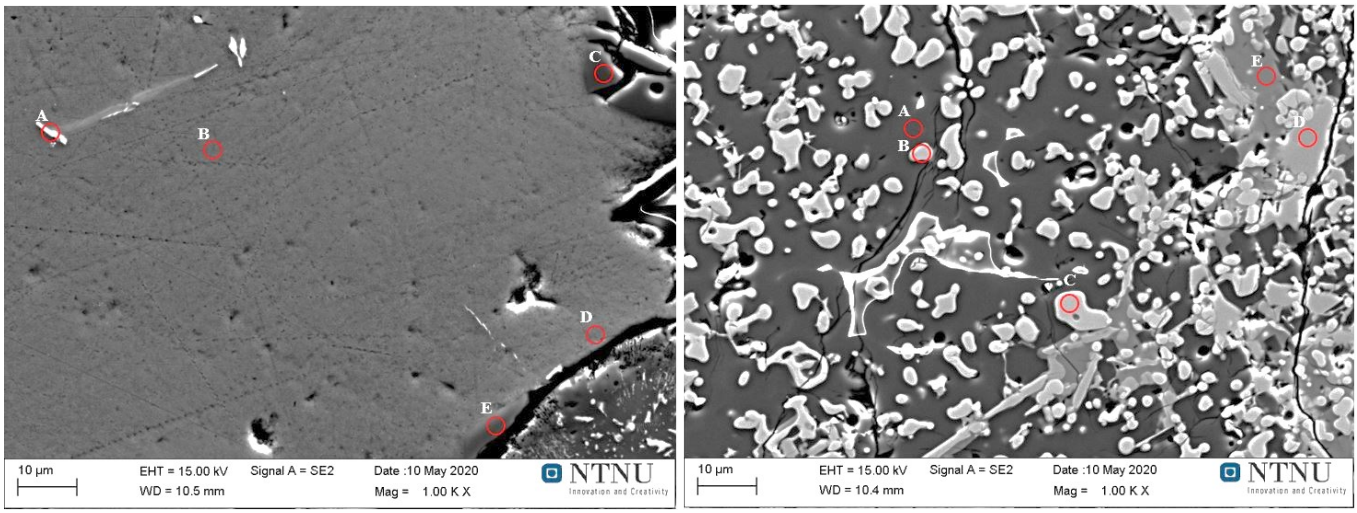

(a) Metal, homogeneous phase.

(b) Slag, some overcharging.

Figure 4.8: SEM images of the reacted metal and reacted slag from experiment 4. Some overcharging from the epoxy are observed in the slag due to pores.

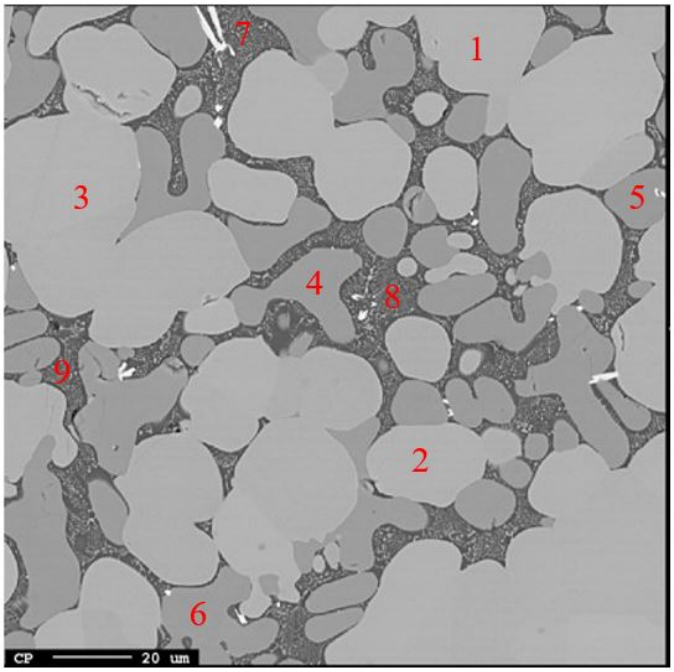

Figure 4.9: EPMA scan of the reacted slag from experiment 4.

Table 4.3: EPMA measurements of points in Fig. 4.9.

Point	Al_2O_3 mass%	CaO mass%	TiO_2 mass%	Phase
1	2.990±0.26	1.311±0.06	103.582 ±0.52	TiO_2
2	2.421±0.26	1.180±0.06	104.780 ±0.52	TiO_2
3	2.963±0.26	1.317±0.06	104.530±0.52	TiO_2
4	2.369 ±0.11	42.456±0.09	52.293 ±0.13	CaO – TiO_2
5	2.578 ±0.11	42.615±0.09	51.980 ±0.13	CaO – TiO_2
6	2.335±0.11	42.390±0.09	52.176 ±0.13	CaO – TiO_2
7	52.501±4.97	33.386±3.48	21.365 ±1.15	CaO – Al_2O_3
8	52.830±4.97	28.673±3.48	23.074 ±1.15	CaO – Al_2O_3
9	42.132±4.97	37.190±3.48	24.172 ±1.15	CaO – Al_2O_3

SEM images and EPMA analysis from experiment 6 are seen in Fig. 4.10, Fig. 4.11 and Table 4.4. The same tendency in the content of TiO_2 in the phases in the reacted slag is seen from the EPMA analysis, while the reacted metal is homogeneous.

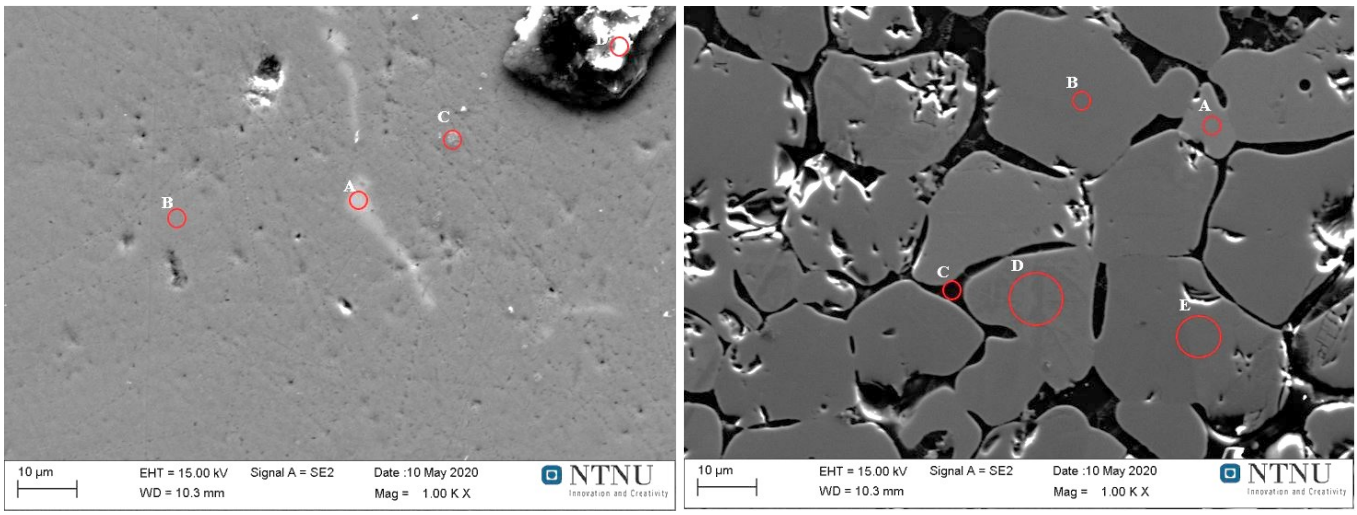

(a) Metal, homogeneous phase.

(b) Slag, different phases observed.

Figure 4.10: SEM images of the reacted metal and slag from experiment 6.

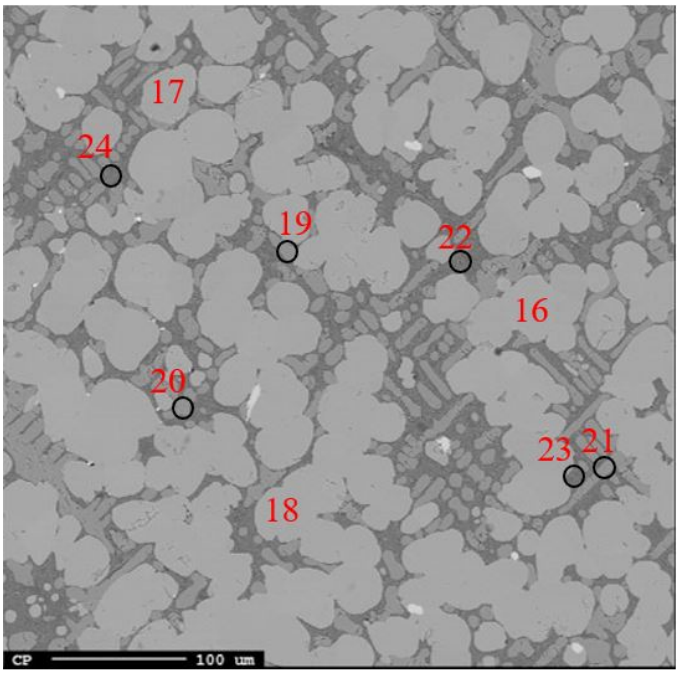

Figure 4.11: EPMA scan of the reacted slag from experiment 6.

Table 4.4: EPMA measurements of points in Fig. 4.11.

Point	Al_2O_3 mass%	CaO mass%	TiO_2 mass%	Phase
16	1.283±0.20	1.005±0.04	109.421 ±0.68	TiO_2
17	1.265 ±0.20	1.035±0.04	108.027±0.68	TiO_2
18	1.688±0.20	0.940 ±0.04	107.939 ±0.68	TiO_2
19	3.190 ±0.25	43.057 ±0.57	50.609 ±0.47	$CaO-TiO_2$
20	2.983 ±0.25	42.057±0.57	51.137 ±0.47	$CaO-TiO_2$
21	3.590 ±0.25	43.393±0.57	49.991 ±0.47	$CaO-TiO_2$
22	46.891±0.63	34.216±1.38	22.671±2.17	$CaO-Al_2O_3$
23	48.176±0.63	32.040 ±1.38	25.994 ±2.17	$CaO-Al_2O_3$
24	46.792±0.63	35.364±1.38	20.749 ±2.17	$CaO-Al_2O_3$

4.1.3 XRD results

In this section, the results from the XRD analysis are presented. For the experiments conducted at 1550 °C formation of perovskite ($CaTiO_3$) and tistarite (Ti_2O_3) are seen. For the experiments performed at 1650 °C formation of perovskite ($CaTiO_3$) and TiO are seen. All the phases in the experiments are summarized in Table 4.5 and Table 4.6.

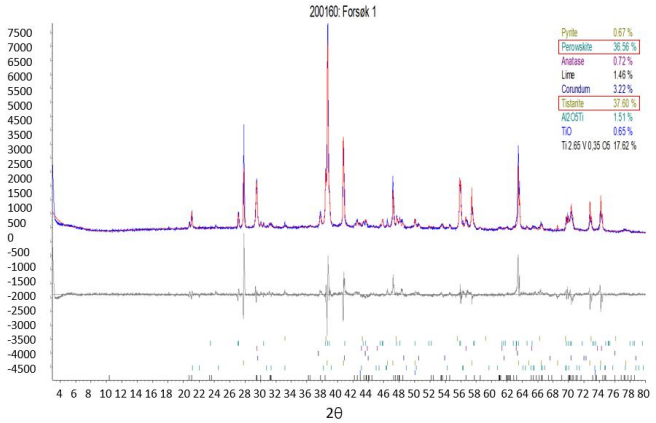

(a) XRD exp.1.

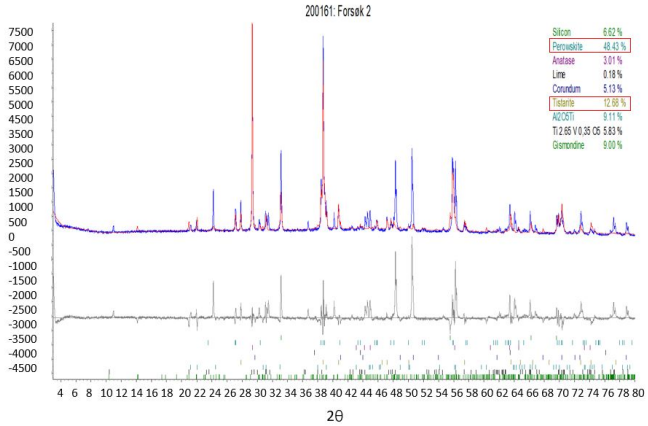

(b) XRD exp.2.

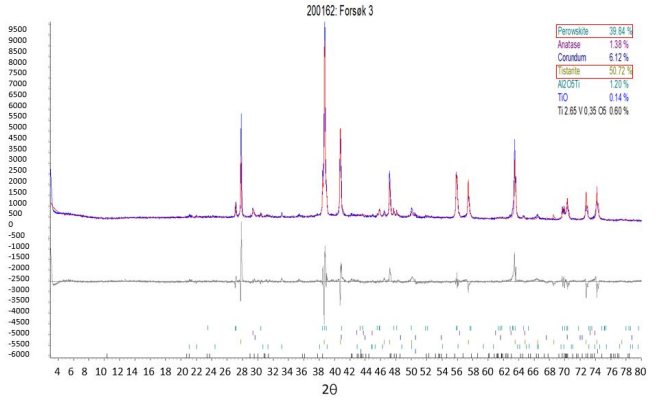

(c) XRD exp.3.

Figure 4.12: Diffractograms on the reacted slags from experiments 1, 2 and 3.

Table 4.5: Phases calculated with XRD in the reacted slag in Fig. 4.12.

Exp.	1	2	3
Pyrite (wt%)	0.67	-	-
Silicon(wt%)	-	6.62	-
Perovskite(wt%)	36.56	48.43	39.84
Anatase (wt%)	0.72	3.01	1.38
Lime (wt%)	1.46	0.18	-
Corundum (wt%)	3.22	5.13	6.12
Tistarite(wt%)	37.60	12.68	50.72
Al_2O_5Ti (wt%)	1.51	9.11	1.20
TiO (wt%)	0.65	-	0.14
$Ti_{2.65}V_{0.35}O_5$ (wt%)	17.62	5.83	0.60
Gismondine (wt%)	-	9.00	-

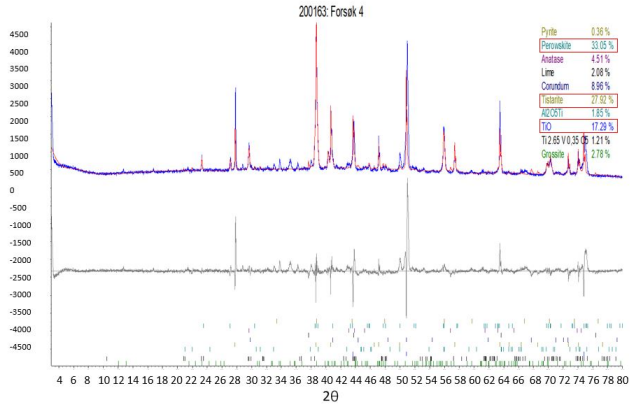

(a) XRD exp.4.

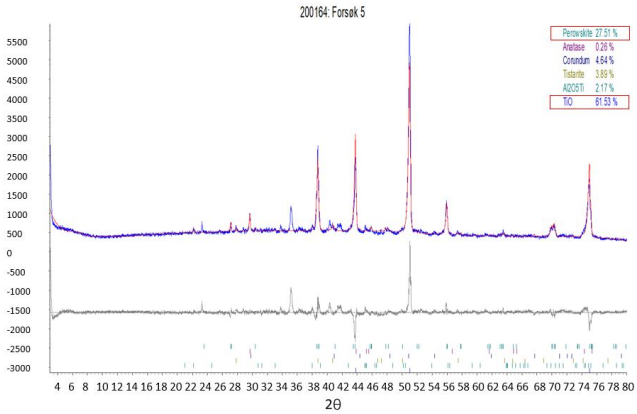

(b) XRD exp.5.

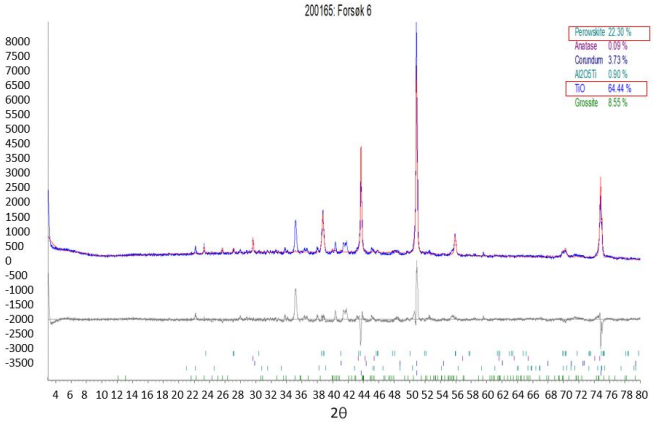

(c) XRD exp.6.

Figure 4.13: Diffractograms on the reacted slags from experiments 4, 5 and 6.

Table 4.6: Phases calculated with XRD in the reacted slag in Fig. 4.13.

Exp.	4	5	6
Pyrite (wt%)	0.36	-	-
Perovskite(wt%)	33.05	27.51	22.30
Anatase (wt%)	4.51	0.26	0.09
Lime (wt%)	2.08	-	-
Corundum (wt%)	8.96	4.64	3.73
Tistarite(wt%)	27.92	3.89	-
Al_2O_5Ti (wt%)	1.85	2.17	0.90
TiO (wt%)	17.29	61.53	64.44
$Ti_{2.65}V_{0.35}O_5$ (wt%)	1.21	-	-
Gismondine (wt%)	2.78	-	-
Grossite (wt%)	-	-	8.55

4.2 Results from experiments with $CaO-SiO_2-TiO_2$ slag

The results from the experiments with slag 2 are presented in this section. The crucibles after cutting are shown and compared. SEM images, EPMA scans and analysis of the reacted slag and metal are presented, and EDS analysis from SEM images are included in Appendix D. The area where the SEM scans have been done is pointed out in experiments 7, 9, 10 and 12.

4.2.1 Visual inspection of the cut crucibles

The cut crucibles from the experiments are shown in the following figures. Essential observations are summarized in these key points:

1. There are no significant differences in the reacted slag or the reacted metal when the temperature is increased from 1550 °C to 1650 °C.
2. The reacted slag has a grey color and is easily removed from the crucible.
3. The reacted metal is observed close to the crucible and is difficult to separate from the crucible. It can imply a reaction between the crucible and the metal.
4. There is less formation of metal in experiments 8 and 11 from the cross-section of the crucibles, and the reacted metal and slag are mixed better.

The crucibles from experiments 7 and 10 with 100 g slag and 26.5 g and 26 g Al are seen in Fig. 4.14. In both the experiments the metal is seen at the bottom of the crucible and against the wall. The slag has a grey color with cracks. In both the experiments the slag was quite easy to get out of the crucible while the metal was stuck to the crucible.

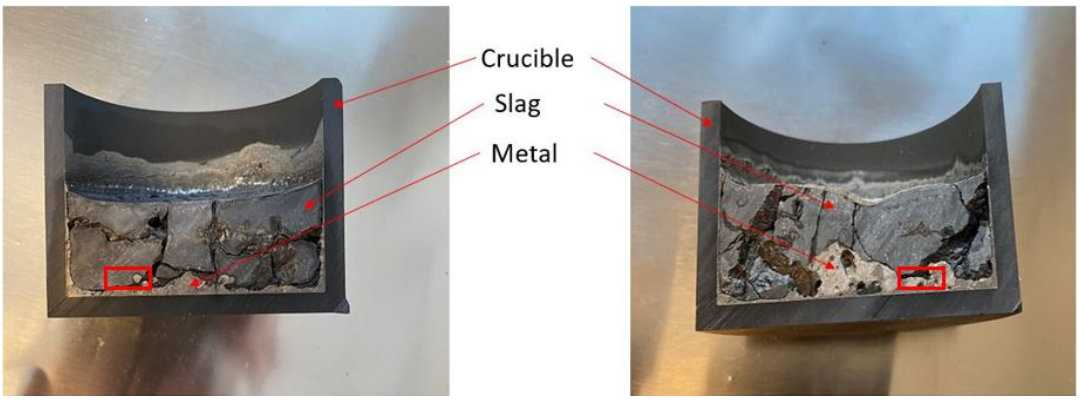

Figure 4.14: Cross-section from experiments 7 and 10 at 1550 °C and 1650 °C.

The crucibles from experiments 8 and 11 with 100 g slag and 20 g and 20.5 g Al are seen in Fig. 4.15. In both the experiments the slag is easily detected with a blue/grey color. The metal, however, is more difficult to see in both experiments. It seems like the metal and slag have been mixed during the melting and solidification, and that most of the metal is in-between the slag. Some silver spots are observed as the metal with a close look at the crucibles.

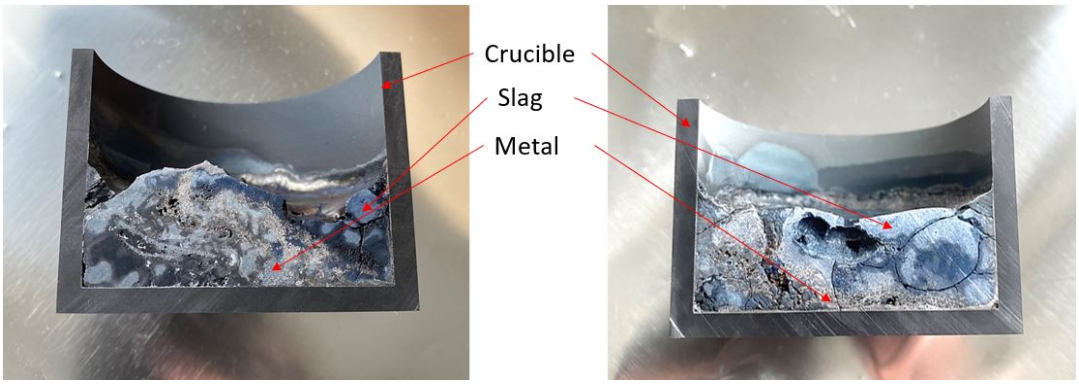

Figure 4.15: Cross-section from experiments 8 and 11 at 1550 °C and 1650 °C.

The crucibles from experiments 9 and 12 with 100 g slag and 32 g and 31.5 g Al are seen in Fig. 4.16. Here both the slag and metal are detected easily. The slag was easily taken out from the crucible as opposed to the metal that is, as can be seen, close to the bottom and the walls of the crucible.

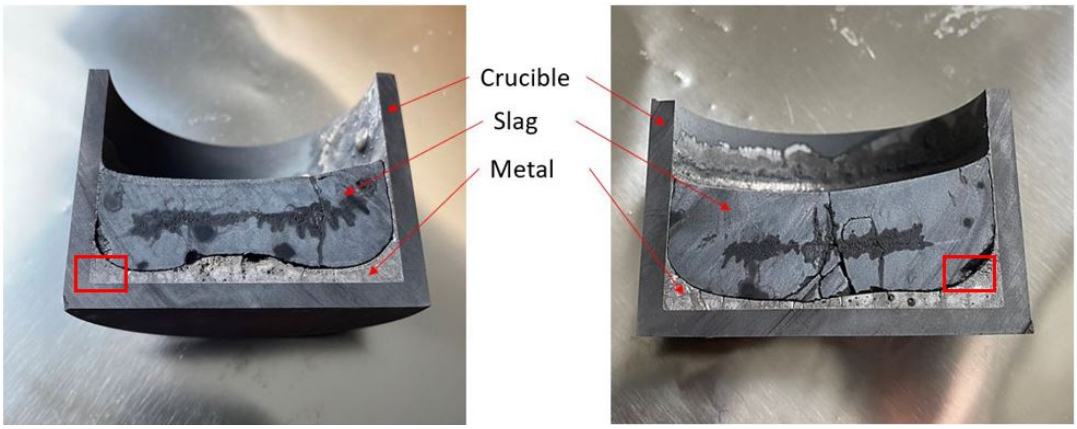

Figure 4.16: Cross-section from experiments 9 and 12 at 1550 °C and 1650 °C.

4.2.2 Results from SEM and EPMA

In this section SEM images, EPMA scans and measurements from the reacted metal and slag are presented. EDS measurements of the points in the SEM images are shown in Appendix D. In the EPMA analysis, three analysis were performed for each phase in each sample.

The overall observations from the analysis are summarized in these key points:

1. Three phases are observed in the reacted metal, a TiSi phase with high Ti content, a Ti_5Si_4 phase with a high Si content, and a mixed phase AlSiCa or $TiSi_2$ with high content of Si depending on the stoichiometric addition of Al. The content of the elements changes with the stoichiometric addition of Al resulting in a slight difference in the calculated phases. For the over-stoichiometric experiments the content of Ca in the mixed phase is high resulting in a CaSiAl phase, while for the 100 % stoichiometric experiments the mixed phase is rather a Si_2Ti phase with a high content of Si.
2. The content of CaO and Al_2O_3 are dominating in the reacted slag, being approximately 40 wt% and 60 wt% respectively. In the under-stoichiometric experiments the content of SiO_2 was relatively high as well, approximately 30 wt%.
3. The content of TiO_2 in the reacted slag is so small that it is clear that an aluminothermic reduction of TiO_2 to Ti has occurred.
4. The temperature does not effect the content in the phases in the reacted metal. The same trend with the phases is seen both at 1550 °C and 1650 °C.
5. The concentration of Ti is highest in the Ti_5Si_4 phase and decreases in the mixed phase where wt% Al is rather high.
6. A decrease in the average Ti concentration is observed with increasing Al content, as can be seen when comparing the EPMA analysis from the 100 % stoichiometric experiments with the 120 % stoichiometric experiments. Corresponding the concentration of Al in the mixed phase is higher in

the over-stoichiometric experiments than in the 100 % stoichiometric experiments.

Since there were no significant differences between the experiments performed at 1550 °C and at 1650 °C, only SEM images and EPMA scans from experiments 7 and 9 are presented.

SEM images and EPMA analysis from experiment 7 are seen in Fig. 4.17, Fig. 4.18 and Table 4.7. Three phases in the reacted metal are seen both in the SEM image and the EPMA scan. The Ti_5Si_4 phase has a high content of Ti seen from both EPMA and EDS, Table D.1, around 60 wt%, located as the white area in the EPMA scan. An increase in the Si content is seen in the TiSi and the mixed phases (the more darker area), point B in Fig. 4.17a and points 7, 8, and 9 in Table 4.7. The amount of the mixed phase (black area) is quite small compared to the amount of the two other phases.

The slag is a bit more challenging to analyze, but two phases can be observed, a bright and a dark. As seen from the EDS measurements, Table D.2, the content of Al, O, and Ca is high, while the content of Si and Ti is below 1 wt%. However, no significant difference in the amount of Ca and Al is seen when comparing the phases.

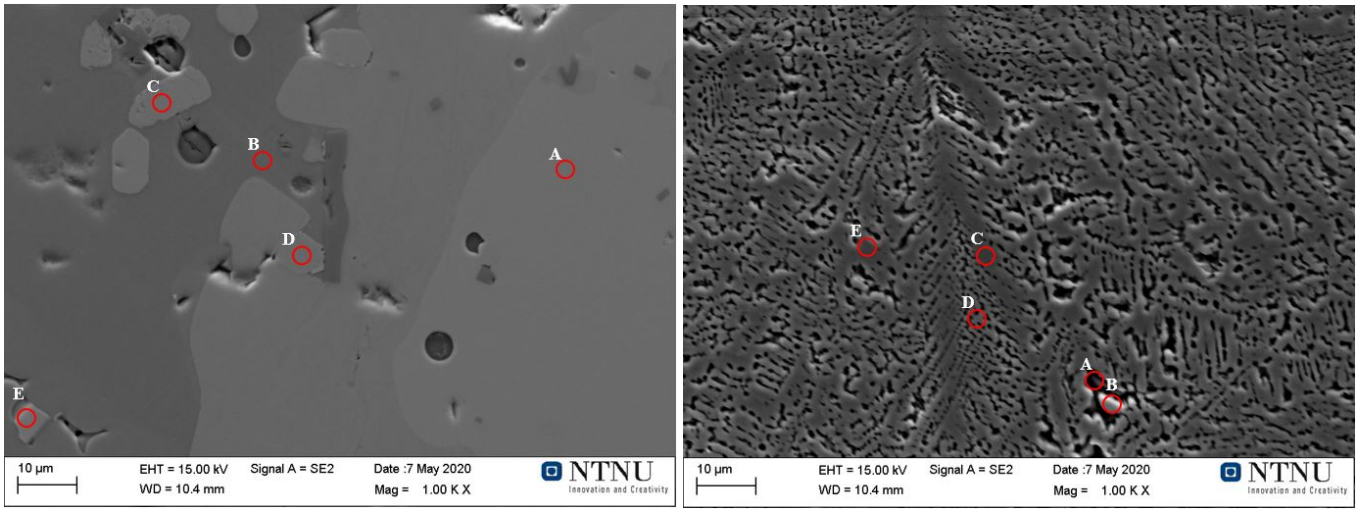

(a) Metal, three phases are observed.

(b) Slag, two phases are observed.

Figure 4.17: SEM images of the reacted metal and slag from experiment 7.

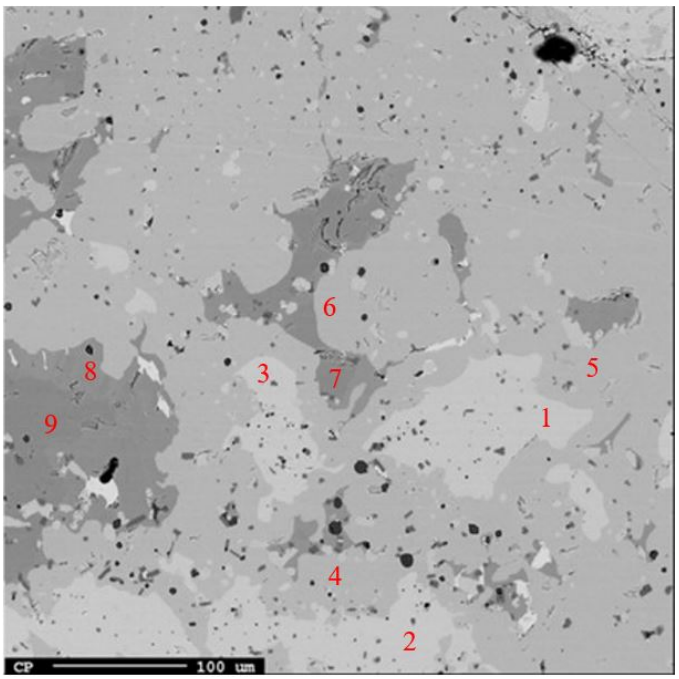

Figure 4.18: EPMA scan of the reacted metal from experiment 7.

Table 4.7: EPMA measurements of point in Fig. 4.18.

Point	Al mass%	O mass%	Ca mass%	Si mass%	Ti mass%	Phase
1	0.058 ±0.01	1.547 ±0.10	0.027 ±0.01	36.603 ±0.42	62.350 ±0.49	Ti_5Si_4
2	0.087 ±0.01	1.352 ±0.10	0.013 ±0.01	35.902 ±0.42	61.222 ±0.49	Ti_5Si_4
3	0.070 ±0.01	1.563 ±0.10	0.038 ±0.01	35.595 ±0.42	61.439 ±0.49	Ti_5Si_4
4	0.029 ±0.00	1.215 ±0.06	0.023 ±0.01	42.261 ±0.47	57.791 ±0.21	TiSi
5	0.023 ±0.00	1.315 ±0.06	0.002 ±0.01	42.085±0.47	57.531±0.21	TiSi
6	0.022 ±0.00	1.367 ±0.06	0.004 ±0.01	41.182±0.47	58.041 ±0.21	TiSi
7	1.378±2.74	1.015 ±0.07	0.016 ±0.06	59.448±2.29	42.456±0.17	$TiSi_2$
8	7.106±2.74	1.000 ±0.07	0.152 ±0.06	53.888±2.29	42.085±0.17	$TiSi_2$
9	1.203±2.74	0.861 ±0.07	0.016 ±0.06	60.014±2.29	42.113±0.17	$TiSi_2$

SEM image and EPMA analysis from experiment 9 are seen in Fig. 4.19, Fig. 4.20 and Table 4.8. Three different phases are as well observed in the reacted metal, with a high content of Ti in the Ti_5Si_4 phase (white area), point A and point E in Fig. 4.19a and points 7, 8 and 9 in Fig. 4.20. As can be seen from both the EDS analysis, Table D.3, and Table 4.8 a quite drastic increase in the content of Al and Ca is observed in the SiTi and the mixed phases (more darker area), point C and points 13, 14, and 15. Corresponding, a drastic decrease in the content of Ti is observed. Again, the amount of mixed phase (black area) is small

compared to the size of the two other phases.

The slag consists of two phases, a bright and a dark, which is quite easily seen from Fig. 4.19b. From the EDS analysis, Table D.4, the contents of Al and O are high in all the points, while the content of Ca is low. Here the content of Ti is approximately 0 wt% while a small amount of Si is detected. It should be noticed that some overcharging were influencing the SEM image, which made it a bit difficult the get useful analysis.

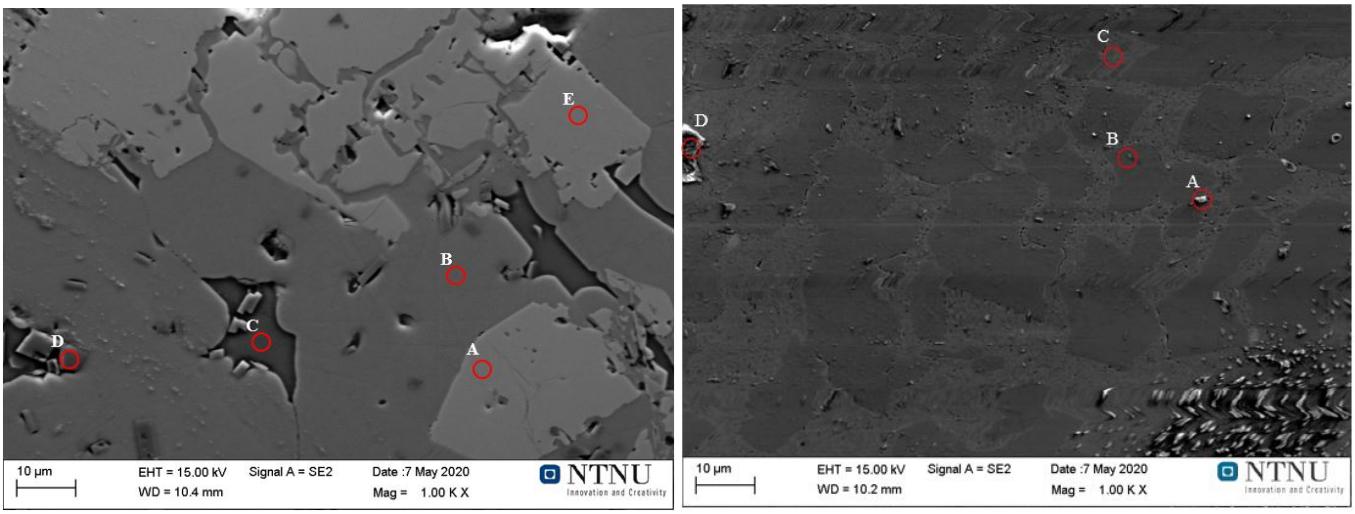

(a) Metal, three phases are observed.

(b) Slag, two phases are observed.

Figure 4.19: SEM images of the reacted metal and slag from experiment 9.

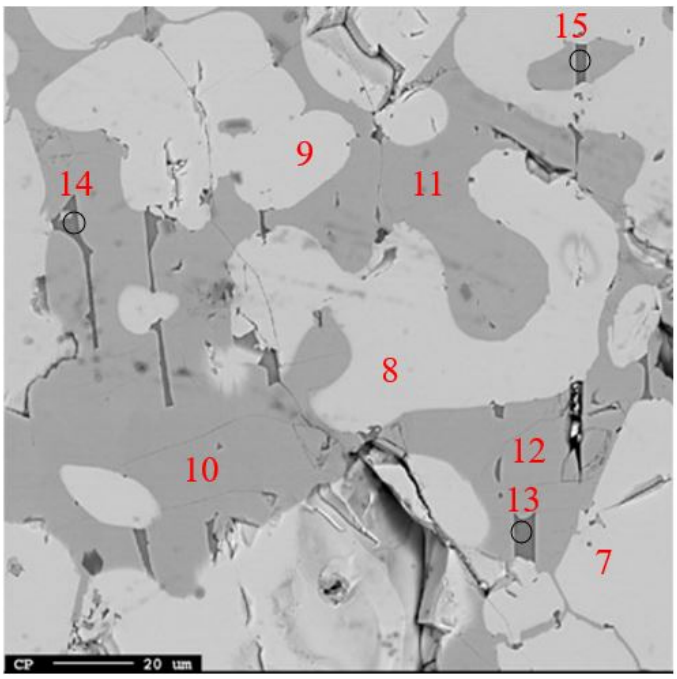

Figure 4.20: EPMA scan of the reacted metal from experiment 9.

Table 4.8: EPMA measurements of point in Fig. 4.20.

Point	Al mass%	O mass%	Ca mass%	Si mass%	Ti mass%	Phase
7	1.628 ±0.06	1.380 ±0.03	0.000 ±0.01	30.248 ±0.30	62.047 ±0.18	Ti_5Si_4
8	1.775 ±0.06	1.450 ±0.03	0.021±0.01	30.269 ±0.30	63.317 ±0.18	Ti_5Si_4
9	1.742 ±0.06	1.376 ±0.03	0.030±0.01	29.629 ±0.30	62.480 ±0.18	Ti_5Si_4
10	8.169 ±0.41	0.927 ±0.05	0.000±0.01	50.973 ±0.77	42.575 ±0.21	TiSi
11	7.869 ±0.41	0.851 ±0.05	0.004±0.01	51.827 ±0.77	42.094 ±0.21	TiSi
12	7.198 ±0.41	0.963 ±0.05	0.017±0.01	52.858 ±0.77	42.475 ±0.21	TiSi
13	33.452±1.50	1.005 ±0.18	24.596±0.63	39.035 ±0.52	4.329 ±0.61	CaAlSi
14	34.410±1.50	0.949 ±0.18	25.538±0.63	38.397 ±0.52	3.068 ±0.61	CaAlSi
15	30.257±1.50	1.360 ±0.18	24.014±0.63	39.663 ±0.52	2.998 ±0.61	CaAlSi

4.3 Calculations done with FactSage

In this section the thermodynamic calculations done with FactSage are presented. Calculations were done with the FToxid (oxide/slag) and FTlite (metal solutions) databases. The FToxid database contains consistently assessed and critically evaluated thermodynamic data for the molten slag phase, numerous extensive ceramic solid solution phases and all available stoichiometric compounds containing SiO_2-CaO-MgO-Al_2O_3-

FeO-Fe_2O_3-MnO-TiO_2-Ti_2O_3-CrO-Cr_2O_3-ZrO_2-NiO-CoO-Na_2O-K_2O-B_2O_3-Cu_2O-As_2O_3-GeO_2-PbO-SnO-ZnO [58]. There are, however, limitations in the FToxid database when calculating slags that contain Ti.

The overall observations from the thermodynamic calculations are summarized in these key points:

1. Two different scenarios are calculated for the $CaO-TiO_2$ slag, (1) with no liquid slag present and (2) with a liquid slag forming. In case (1) addition of 67 g Al is needed to fully reduce TiO_2 and in case (2) addition of 115 g-131 g Al is needed.
2. The phases in the slag at room temperature for (2) for both 1550 °C and 1650 °C are corundum (Al_2O_3-TiO_2), perovskite ($Ca_2Ti_2O_6$ and $Ca_2Ti_2O_5$) and $CaAl_2O_4$.
3. For slag 2, 40 g Al is needed for complete reduction at 1650 °C and 140 g Al is needed for complete reduction at 1550 °C.
4. For experiments at 1650 °C the phases in the reacted slag are calculated to be $Ca_3Ti_2O_7$-$Ca_3Ti_2O_6$, $CaAl_2O_4$, $Ca_3Al_2O_6$ and Ca_2SiO_4, while the phases in the reacted metal are Si_4Ti_5, $Ti_3Al_2Si_5$ and $Ti_7Al_5Si_{14}$.
5. For experiments at 1550 °C the phases in the reacted slag are calculated to be $Ca_3Ti_2O_7$-$Ca_3Ti_2O_6$, Si_5Ti_5, $CaAl_2O_4$, $Ca_3Al_2O_6$, Ca_2SiO_4 and $Ca_3Ti_2O_7$, while the phases in the reacted metal are Si_4Ti_5 and $Ti_3Al_2Si_5$.

4.3.1 $CaO-TiO_2$ slag

For the CaO-TiO_2 slag two different scenarios are calculated:
(1) No liquid slag and the liquid metal is in equilibrium with two solid calcium-aluminate phases, $CaAl_{12}O_{19}$(s) and $CaAl_4O_7$(s).
(2) A liquid slag phase is forming at high Al additions, and $CaAl_{12}O_{19}$(s) and $CaAl_4O_7$(s) are removed as possible product species.

In case (1) with the addition of 67 g Al all of the Ti will be found in the liquid metal solution and completely reduced to metallic Ti. At this point, there is no remaining molten slag and the molten metal is in equilibrium with two solid calcium-aluminate phases, $CaAl_{12}O_{19}$(s) and $CaAl_4O_7$(s).

In case (2), 115 g to 131 g of Al has to be added to achieve almost complete reduction of TiO_2 to metallic Ti. In this case, both for the 1650 °C and 1550 °C, the slag solidifies at around 1400 °C into corundum, perovskite and $CaAl_2O_4$(s) presented in Fig. 4.21. As can be seen the corundum phase is formed around 1630 °C, and its amount increases as the temperature lowers. The rest of the slag solidifies around 1400 °C, where it solidifies into the phases shown in Table 4.9.

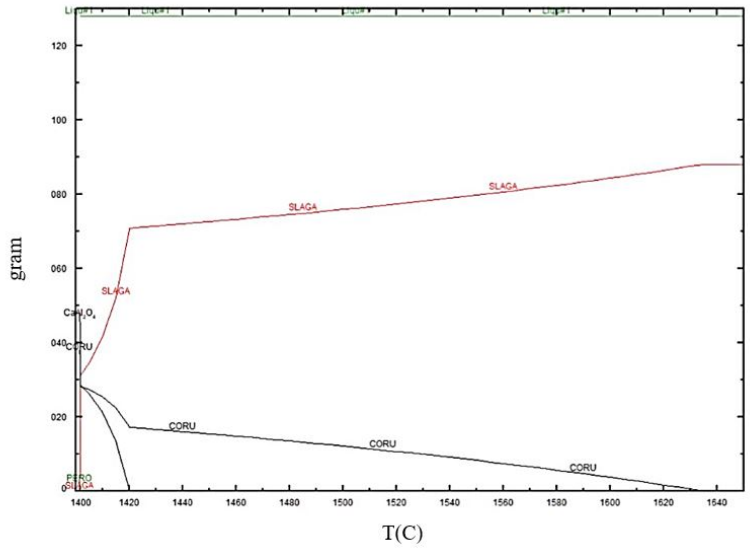

Figure 4.21: Solidification calculations for both 1650 °C and 1550 °C.

Table 4.9: Theoretical concentrations of phases in the slag at room temperature.

Corundum	Al_2O_3	99.837wt%
	TiO_2	0.163wt%
Perovskite	$Ca_2Ti_2O_6$	1.085wt%
	$Ca_2Ti_2O_5$	98.915wt%
	$CaAl_2O_4$	47.973g

4.3.2 $CaO-SiO_2-TiO_2$ slag

For the CaO-SiO_2-TiO_2 slag the calculations done implies that for the 1650 °C case addition of approximately 40 g Al will be needed to get all of the Ti and Si into the molten metal liquid phase. The theoretical concentrations of the phases in the metal and slag before solidification are seen in Table 4.10. Solidification gives formation of $Ca_{12}Al_{14}O_{33}$ and $CaAl_2O_4$, presented in Fig. 4.22 with the theoretical concentrations of phases in the reacted metal and reacted slag presented in Table 4.12 and Table 4.13.

In the case of 1550 °C, addition of approximately 140 g Al will be needed to get all of the Ti and Si into the molten metal liquid phase. The theoretical concentrations of the phases in the metal and slag before solidification are seen in Table 4.11. Solidification gives formation of $CaAl_2O_4$ and $Ca_3Al_2O_6$ presented in Fig. 4.23 with the theoretical concentrations of the phases in the reacted metal and reacted slag presented in Table 4.14 and Table 4.15.

All the solidification calculations are done for equilibrium cooling, except for the calculations done for the reacted slag from experiments at 1550 °C where Scheil-Gulliver cooling was used. This was due to

convergence problems in trying to achieve 100 % solidification during the calculations. However, it should be mentioned that there were no differences in the resulting phases when comparing equilibrium and Scheil-Gulliver.

Table 4.10: Theoretical concentrations of phases in metal and slag from experiments performed at 1650 °C before solidification.

Metal	Al	29.521wt%
	Ca	7.248wt%
	Si	27.726wt%
	Ti	35.506wt%
Slag	Al_2O_3	53.213wt%
	SiO_2	0.022wt%
	CaO	46.716wt%
	Ti_2O_3	0.037wt%
	TiO_2	0.012wt%

Table 4.11: Theoretical concentrations of phases in metal and slag from experiments performed at 1550 °C before solidification.

Metal	Al	74.224wt%
	Ca	7.604wt%
	Si	7.966wt%
	Ti	10.206wt%
Slag	Al_2O_3	57.866wt%
	SiO_2	0.003wt%
	CaO	42.108wt%
	Ti_2O_3	0.020wt%
	TiO_2	0.003wt%

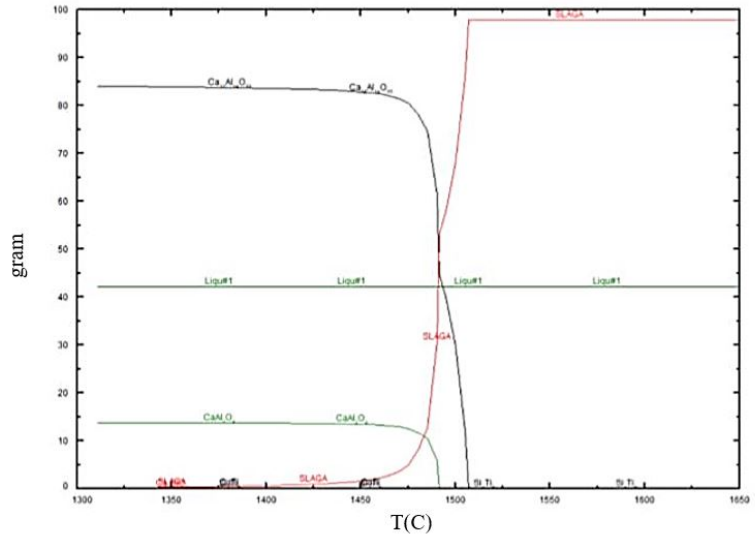

Figure 4.22: Solidification calculation for the 1650 °C case.

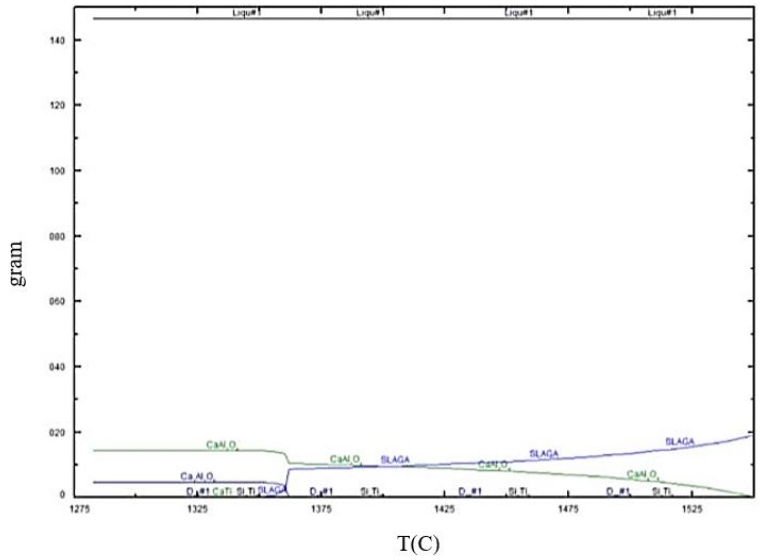

Figure 4.23: Solidification calculation for the 1550 °C case.

Table 4.12: Constituents and phases at 700.81 °C in the reacted metal from experiments performed at 1650 °C.

Phase	Components
B27	Ti, Si
D022	Ti, Si, Al
D13	Ca, Si, Al
hP3	Ca, Si, Al
Si_4Ti_5	Ti, Si
$Ti_3Al_2Si_5$	Ti, Si, Al
$Ti_7Al_5Si_{14}$	Ti, Si, Al

Table 4.13: Constituents and phases at 1319.28 °C in the reacted slag from experiments performed at 1650 °C.

Phase	Components
Liquid	Ti, Ca, Si, Al
$Ca_3Ti_2O_7$-$Ca_3Ti_2O_6$	Ti, Ca, O
$CaAl_2O_4$	Ca, Al, O
$Ca_3Al_2O_6$	Ca, Al, O
Ca_2SiO_4	Ca, Si, O

Table 4.14: Constituents and phases at 625.78 °C in the reacted metal from experiments performed at 1550 °C.

Phase	Components
FCC-A1	Ti, Ca, Si, Al
D022	Ti, Si, Al
D13	Ca, Si, Al
Si_4Ti_5	Ti, Si
$Ti_3Al_2Si_5$	Ti, Si, Al

Table 4.15: Constituents and phases at 1282.19 °C in the reacted slag from experiments performed at 1550 °C.

Phase	Components
$Ca_3Ti_2O_7$-$Ca_3Ti_2O_6$	Ti, Ca, O
Si_4Ti_5	Ti, Si
$CaAl_2O_4$	Ca, Al, O
$Ca_3Al_2O_6$	Ca, Al, O
Ca_2SiO_4	Ca, Si, O
$Ca_3Ti_2O_7$	Ti, Ca, O

Chapter 5

Discussion

In this chapter, the results obtained are discussed and evaluated. The chemical compositions of the reacted slag and metal obtained by EDS, EPMA, XRD, and FactSage, will be discussed and compared with the theory. However, studies and theory concerning TiO_2 containing slags and Ti-alloys are limited. Hence, the most relevant comparison of the chemical compositions will be with the results obtained with FactSage. The effect of temperature, the effect of Al added, and consistency with thermodynamic calculations will be discussed for each slag.

5.1 CaO-TiO_2 slag

5.1.1 Effect of temperature

Two different holding temperatures were used, 1550 °C and 1650 °C. The reason for this was to see if there would be any changes or differences between the compositions or the microstructure in the reacted metal and the reacted slag at a higher temperature.

To see if there were any changes in the compositions in the reacted slag, the concentrations of TiO_2, Al_2O_3, and CaO were plotted for each experiment and compared. The graphs are seen in Fig. 5.1 and the EPMA scans of the slags are presented in Fig. 5.2 and Fig. 5.3. As can be seen from the graphs, a slight deviation is observed between the experiments performed at 1550 °C and 1650 °C. For the experiments at 1550 °C, a slight decrease in the concentration of TiO_2 and an increase in the concentration of Al_2O_3 is seen when the addition of Al is increased. For the experiments performed at 1650 °C, the concentrations are approximately constant. The compositions at 1650 °C are as well quite similar to the starting composition of the slag, which makes sense since there was no reduction of TiO_2 to Ti during the holding time. However, it should be noticed that the results from experiment 2 conducted at 1550 °C are not included in the graph. This was because the sample included both metal and slag, making it difficult to get reliable results from the slag.

Since only one parallel was performed for each holding temperature, it is difficult to know if these results are reliable. Therefore, more parallels should be included to confirm the observed change in the composition

or if this was only a coincidence.

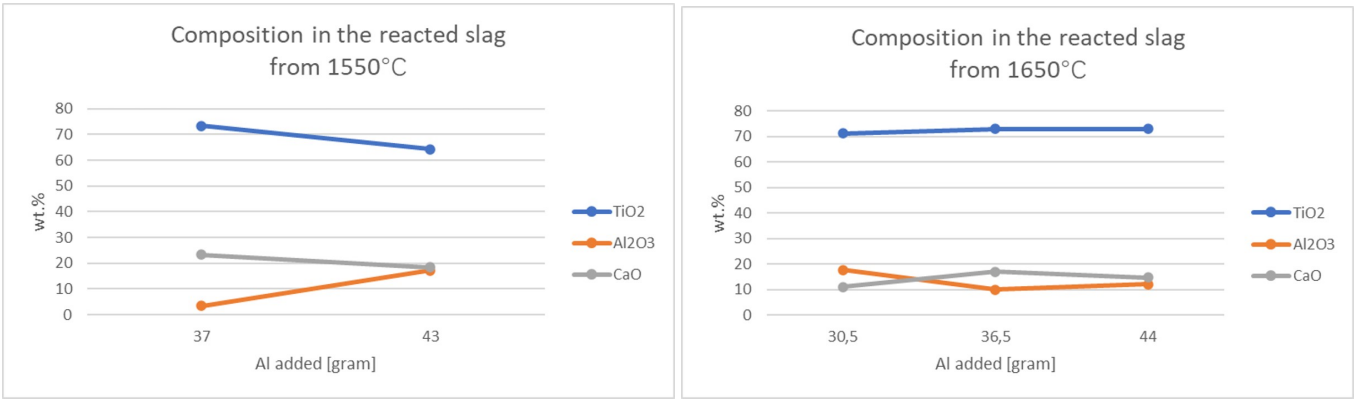

Figure 5.1: Contents of TiO_2, Al_2O_3 and CaO in the reacted slag.

However, by looking at the EPMA scans, it is clear that the microstructure is different for the experiments performed at 1550 °C compared to the experiments conducted at 1650 °C. This change is most likely due to the difference in the holding temperature. A reason for this could be the difference in the solidification rate for each experiment. As can be seen from the calculated cooling rates presented in Appendix B.1 and Appendix B.2, the cooling rates for the experiments performed at 1650 °C were a bit higher than for the experiments conducted at 1550 °C. This leads to a more rapid solidification resulting in smaller phases, as seen by comparing the EPMA scans in Fig. 5.2 with Fig. 5.3. By looking at the microstructures and the size of the phases, it is clear that the cooling rate is highest for experiment 5, and this is confirmed by the calculated rate as well, 116.67 °C min^{-1} compared to 83.33 °C min^{-1} for experiments 1, 2 and 3. Nevertheless, the solidification rate was not affected with purpose since the crucibles were allowed to cool down in the furnace. It would have been interesting to compare a quenched reacted slag and metal with the results from these experiments to see how much the solidification rate can affect the microstructure. However, from the EPMA scans of the reacted slags microstructures, it can be concluded that the holding temperature affects the solidification rate and, hence, the microstructure. Again, as mentioned, more parallels should be included to confirm the change in the microstructure.

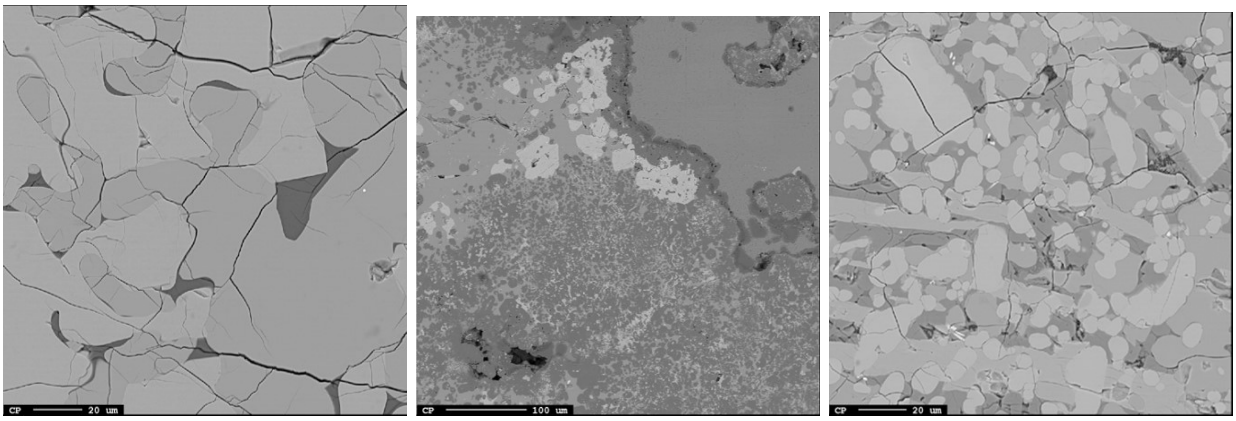

(a) 100 % stoichiometric. (b) Under-stoichiometric. (c) Over-stoichiometric.

Figure 5.2: Scans of the reacted slag from experiments performed at 1550 °C.

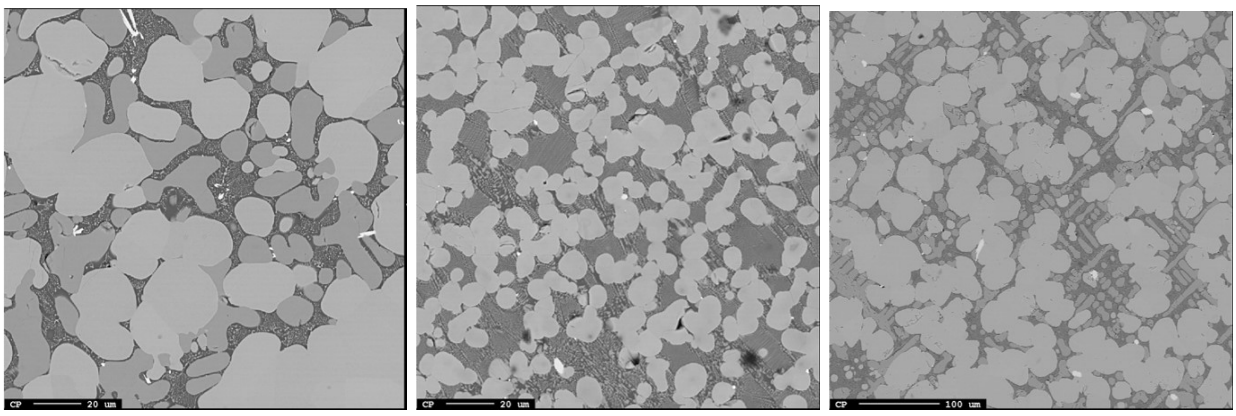

(a) 100 % stoichiometric. (b) Under-stoichiometric. (c) Over-stoichiometric.

Figure 5.3: Scans of the reacted slag from experiments performed at 1650 °C.

5.1.2 Effect of Al added

The amount of Al added to the experiments was calculated stoichiometric, with the intention of getting 100 % reduction of TiO_2. For the two other experiments, the addition of Al was added as 20 % over- and under stoichiometric. From the calculations done, seen in Section 3.2.1, approximately 37 g of Al was needed to get 100 % reduction, and 29.5 g and 44 g under- and over stoichiometric respectively.

However, as could be seen from both the SEM EPMA, and EDS analysis, the reacted metal from all the experiments was homogeneous and had approximately 100 wt% Al with some formation of Al_2O_3. Correspondingly, the concentration of TiO_2 in the reacted slag from all the experiments was subsequently high.

It is expected that the amount of TiO_2 in the reacted slag would decrease with the increase of Al added to the slag, while the amount of Al_2O_3, should, as a result, increase in the reacted slag. As discussed in the theory, the formation of other oxides could be why Ti was not detected. As mentioned in Section 2.2.4, in the aluminothermic process, a portion of TiO_2 reduces to TiO and Ti_2O_3. These oxides are stable, and their reduction is difficult since titanium has a strong affinity for oxygen and is stable in its highest oxidation state (Ti^{4+}). This combined makes it difficult to reduce Ti.

To see if there had been a reduction of TiO_2 to other oxides, XRD analysis was performed on the reacted slag from all the experiments. As could be seen from the XRD results presented in Section 4.1.3, the amount of anatase (TiO_2) was small in all the experiments, which implied that there had been a reduction of the TiO_2. As could be expected from the theory, Section 2.3.4, the formation of Ti_2O_3 and TiO were observed, which explains why no Ti was observed in the metal. A comparison of the XRD results from the experiments conducted at 1550 °C with the experiments performed at 1650 °C shows that there are some differences in the phases formed. In the experiments performed at 1550 °C, the dominant phases formed in the slag were perovskite and Ti_2O_3. In the experiments performed at 1650 °C, on the other hand, the dominant phases formed were perovskite and TiO. As can be remembered from the figures of the cut crucibles, the slag changed color from black to a bronze color for the reacted slag, which was held at 1650 °C, as seen in Fig. 5.4. The change in the color can be explained by the two phases formed at the different holding temperatures. The Ti_2O_3 phase dominating at 1550 °C slag appears as black powder, explaining the black color of the reacted slag. The TiO phase dominating at 1650 °C appears as bronze crystals, explaining the bronze color of the reacted slag.

The formation of Ti_2O_3 and TiO can also be explained by the Gibbs free energy of the reaction, as discussed in Section 2.2.4. Thermodynamically it is not difficult for TiO_2 to be reduced to Ti_2O_3 because this reduction has the most negative Gibbs free energy. In contrast, the reduction of TiO_2 to Ti is difficult from a thermodynamic point of view. The formation of TiO at 1650 °C could also imply that higher temperatures are needed to reduce TiO_2 to Ti with the amount of slag and aluminium used in this experiments since the reduction to TiO is slightly more complicated than reduction to Ti_2O_3.

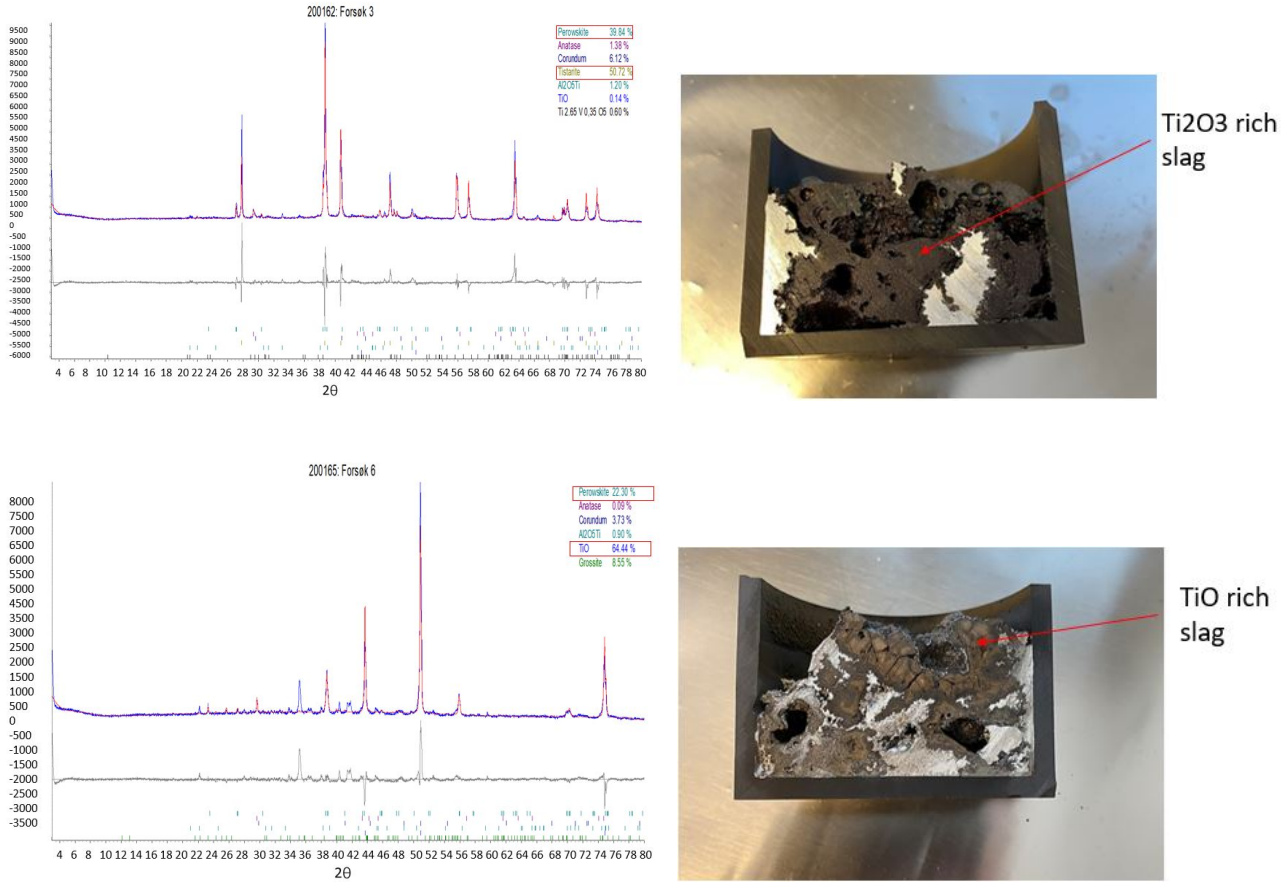

Figure 5.4: XRD results from experiments 3 and 6 to the left and the cut crucibles to the right.

The reduction of TiO_2 to TiO and Ti_2O_3 by Al can be described as:

$$Al + TiO_2 \rightarrow Al_2O_3 + xTi_2O_3 + yTiO$$

By looking at the concentration of Al_2O_3 in the reacted slag for the experiments conducted, a slight increase is seen when the addition of Al is increased. Also, an increase in the concentration of Ti_2O_3 is observed in the XRD measurements for the experiments conducted at 1550 °C. Similar, an increase in the content of TiO in the experiments conducted at 1650 °C is seen. From these analyses, it can be assumed that increasing the amount of Al added leads to an increase in the Al_2O_3 concentration in the reacted slag and an increase in the amount of Ti_2O_3 and TiO reduced. As can be seen, as well, is that the concentration of Al_2O_3 is highest in experiment 3. As can be remembered from the EPMA results shown in Section 4.1.2, the standard deviations were quite high for the analysis done on the reacted slag. This could be why the content of Al_2O_3 was high compared to the content in experiment 6, which had the same addition of Al.

When comparing the calculated concentration of Al_2O_3 with the content of corundum found in the XRD analysis, it fits quite well for the 100 % stoichiometric experiments (1 and 4). For the over-stoichiometric experiments (3 and 6), the calculated content is much higher than the XRD analysis implied.

Table 5.1: Content of Al_2O_3, Ti_2O_3 and TiO in the reacted slag.

Temperature °C	Al added g	Calculated Al_2O_3 wt%	XRD Corundum wt%	Ti_2O_3 wt%	TiO wt%
1550	37.0	3.31	3.22	37.60	0.65
1550	43.0	17.38	6.12	50.72	0.14
1650	36.5	10.43	8.96	27.92	17.29
1650	44.0	12.97	3.73	-	64.44

5.1.3 Consistency with thermodynamic calculations

As the thermodynamic calculations indicate, presented in Section 4.3.1, the slag solidifies into corundum, perovskite and $CaAl_2O_4$, shown in Fig. 4.21. As can be seen from the XRD results, both perovskite and corundum were detected in the reacted slag from all the experiments. The amount of perovskite was significant, being above 20 wt% in each experiment, while the amount of corundum being not that significant, below 10 wt%.

The area fraction of each phase was calculated using ImageJ for all the experiments, and the overall concentrations of TiO_2, Al_2O_3 and CaO were calculated with respect to the area fractions. The compositions were plotted in the ternary phase diagram, seen in Fig. 5.5. As seen from the phase diagram and the calculated compositions, the compositions in the reacted slags are quite similar to the composition in the starting slag with 86 wt% TiO_2 and 15 wt% CaO. The concentration of Al_2O_3 is relatively low, as expected since most of the Al is found in the reacted metal. Comparing with the thermodynamic calculations done with FactSage, there are significant differences observed. The concentration of Al_2O_3 is rather high in the slag calculated thermodynamically, while the concentrations of Ti_2O_3 and TiO_2 are low. The opposite is found by calculations from the EPMA analysis. This was expected due to no reduction of TiO_2 to Ti and is rather confirming that no reduction has occurred. On the other hand, the calculated content of CaO fits quite well with the thermodynamic calculations, being in the range between 17 wt% to 23 wt%. This could mean that if an aluminothermic reduction had occurred, the contents of Al_2O_3 in the reacted slag would have been quite similar to the ones calculated with FactSage.

Table 5.2: Area fraction of phases in the reacted slag and the total wt% of the oxides.

Exp.	**White phase** %	**Grey phase** %	**Dark phase** %
1	45.30	47.61	7.10
3	70.73	23.71	5.56
4	55.92	27.40	16.68
6	59.33	16.13	24.54
Exp.	**Oxide**	**Calculated** wt%	**FactSage** wt%
1	Al_2O_3	3.31	76.57
	CaO	22.55	22.74
	TiO_2	70.83	5.61×10^{-3}
	Ti_2O_3	-	0.69
3	Al_2O_3	17.83	
	CaO	19.04	
	TiO_2	66.34	
4	Al_2O_3	10.43	78.64
	CaO	17.87	20.29
	TiO_2	76.42	1.10×10^{-2}
	Ti_2O_3	-	1.06
6	Al_2O_3	12.97	
	CaO	15.81	
	TiO_2	78.18	

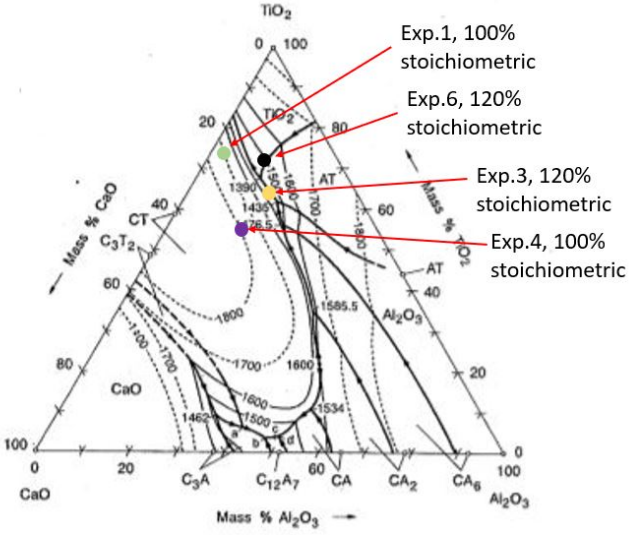

Figure 5.5: Ternary phase diagram with the calculated compositions from EPMA analysis.

As seen from the SEM and EPMA scans, three phases were observed in the reacted slag, a TiO_2-rich, a TiO_2-CaO rich and a CaO-Al_2O_3 rich. As seen from the EPMA analysis presented in Section 4.1.2, the concentration of TiO_2 was the highest in the TiO_2-rich phase, which also had the highest area-fraction. In the two other phases, a decrease in the concentration of TiO_2 was observed. In contrast, an increase in the concentrations of CaO and Al_2O_3 were observed. The average concentrations of the oxides in the three phases were calculated and plotted in the phase diagrams with the overall composition pointed out as well presented in Fig. 5.6. The phases are pointed out with red arrows, while the solidification paths from the overall composition (green points) are pointed out with black dotted arrows. The compositions of each phase are presented in Appendix E.1.

From the calculations and the location of the point in the phase diagrams, the phase with the highest concentration of TiO_2 is most likely a TiO_2 phase or a $CaTiO_3$ phase, shown as the purple points in Fig. 5.6. This is justified by both looking at the content of TiO_2 in the phase compared to Al_2O_3 and CaO and also the location of the phase being close to the TiO_2 rich corner.
The phase with relatively high contents of TiO_2 and CaO is most likely a $CaTiO_3$ phase or a $Ca_3Ti_2O_7$ phase by looking at the wt% and the grey points in the phase diagrams. It is worth noticing that for the over-stoichiometric experiment at 1550 °C, the high concentrations of Al_2O_3 (above 34 wt%) implies formation of a $Ca_3Ti_8Al_{12}O_{37}$ phase. The content of TiO_2 was low as well in the TiO_2 rich phase for this experiment.
The third phase with mostly CaO and Al_2O_3 is most likely a $CaAl_2O_4$ phase or a $Ca_{12}Al_{14}O_{33}$ phase by looking at the wt% of Al_2O_3 and CaO and the location of the black points in the phase diagrams.

By comparing these phases with the ones calculated by FactSage, the first thing to notice is that the phase corundum, Al_2O_3, is not found in the reacted slag as one phase. This can most likely be explained by small amounts of Al being oxidized and that most of the Al still is in the metal. The two other phases, perovskite ($CaTiO_3$) and $CaAl_2O_4$, could be detected in the reacted slag from the EPMA analysis, together with the phases TiO_2, $Ca_{12}Al_{14}O_{33}$ and $Ca_3Ti_8Al_{12}O_{37}$. It was expected that there would be some differences between the phases calculated from the EPMA analysis and the phases calculated with FactSage. By looking at the amount of Al used in the calculations with FactSage and comparing with the Al added, 67 g or 115 g to 131 g with 30 g, 37 g and 44 g respectively, the difference would most likely affect the phases formed during the solidification and the content in the phases. This was seen as well in Table 5.2, where the thermodynamic calculated content of Al_2O_3 were close to 80 wt% compared to being below 20 wt% from the EPMA analysis. Correspondingly, the concentration of TiOx was rather low in the thermodynamic calculations compared to the results from EPMA.

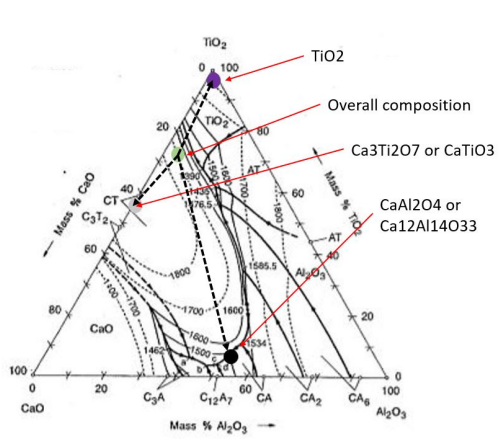

(a) Plot from experiment 1.

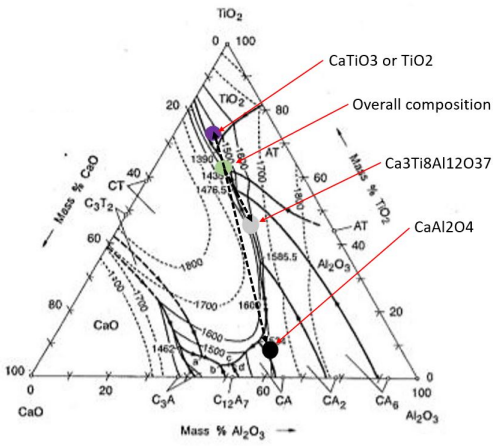

(b) Plot from experiment 3.

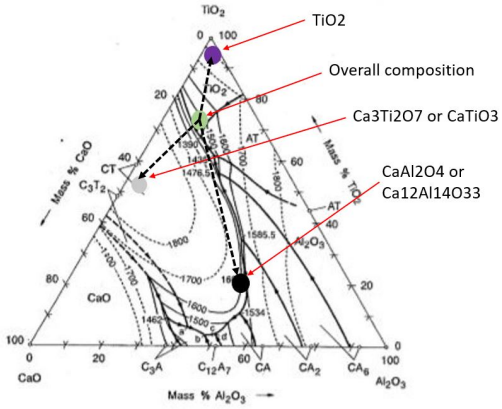

(c) Plot from experiment 4.

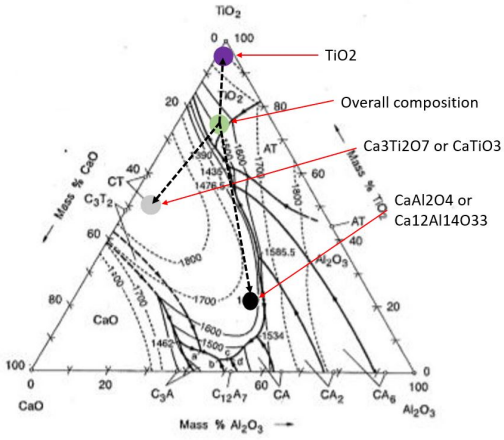

(d) Plot from experiment 6.

Figure 5.6: Plot of the overall content in the slag with the composition of the three phases.

5.2 CaO-SiO_2-TiO_2 slag

In this section, the results from the experiments with slag 2 are presented. What should be noticed and could be seen from the cross-sections of the crucibles, the reacted metal and slag from the under-stoichiometric experiments (8 and 11) were well mixed. This made it difficult to get samples with only reacted metal and only reacted slag. The analyses from these experiments were not that reliable and, in some calculations, not included.

5.2.1 Effect of temperature

The experiments with slag 2 were conducted at two different holding temperatures, 1550 °C, and 1650 °C, respectively. This was to see if the holding temperature would affect the compositions in the reacted metal and slag and also the microstructure.

Three phases were detected in the reacted metal from all the experiments. As seen from the calculated cooling rates in Appendix B.2, the slowest rate was 70 °C min^{-1} for experiment 12 (under-stoichiometric), and the highest rate was 87.50 °C min^{-1} for experiments 10 (100 % stoichiometric) and 11 (under-stoichiometric). Seen from the EPMA scans of the metal presented in Fig. 5.7 and Fig. 5.8, there were some changes in the microstructure. However, these changes are most likely due to the difference in the amount of Al added and not the solidification rate. This assumption is made by the similarities seen when comparing the microstructures of the reacted metals from the two experiments with the same addition of Al, 100 % stoichiometric (7 and 10), under-stoichiometric (8 and 11), and over-stoichiometric (9 and 12), respectively. The same shapes of the phases are seen, and the same color of the phases is observed, and it is therefore concluded that the holding temperature did not affect the microstructure.

Considering the composition of the phases in the reacted metal at the two different holding temperatures, no significant differences were observed when comparing the EPMA analysis of the elements in the reacted metal. The same trend was seen for both 1550 °C and 1650 °C with high concentration of Ti in the assumed to be Ti_5Si_4 phase (white area), around 60 wt%. The same decrease in the Ti concentration for the two other phases (grey and black area) and a corresponding increase in the concentrations of Si and Al were observed, presented in Table 5.3. As seen in the table, the composition does not change noteworthy by increasing the holding temperature. It is therefore concluded that the increase in the holding temperature did not affect the composition of the phases in the reacted metal.

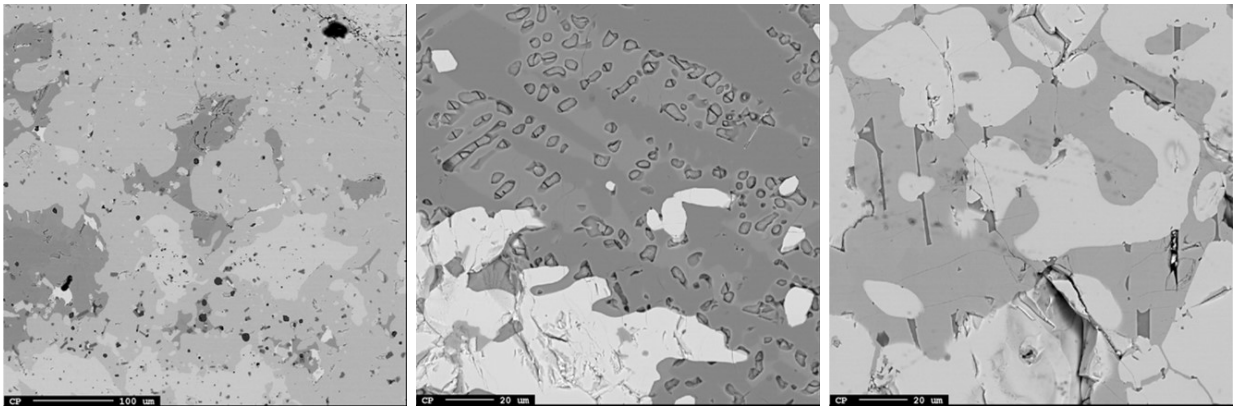

(a) 100 % stoichiometric. (b) Under-stoichiometric. (c) Over-stoichiometric.

Figure 5.7: Scans of the reacted metal from experiments performed at 1550 °C.

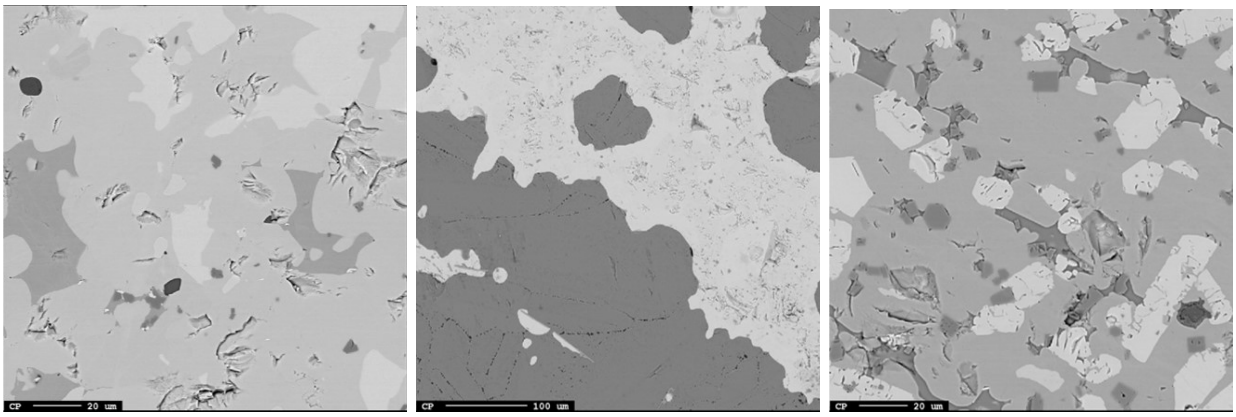

(a) 100 %. (b) Under-stoichiometric. (c) Over-stoichiometric.

Figure 5.8: Scans of the reacted metal from experiments performed at 1650 °C.

Table 5.3: wt% of Si, Al and Ti in the phases in the reacted metal.

Experiment	**Element**	**White area** wt%	**Grey area** wt%	**Black area** wt%	**Temperature** °C
7	Si	36.03	41.84	57.78	1550
	Al	0.07	0.02	3.23	
	Ti	61.67	57.79	42.22	
9	Si	30.05	51.89	39.03	1550
	Al	1.72	7.75	32.71	
	Ti	62.28	42.38	3.47	
10	Si	35.74	41.89	60.03	1650
	Al	0.04	0.01	0.97	
	Ti	61.81	57.47	42.68	
12	Si	31.13	54.97	41.39	1650
	Al	0.97	6.45	34.68	
	Ti	63.17	42.21	2.24	

5.2.2 Effect of Al added

The amount of Al added to the experiments was calculated stoichiometric, with the intention of getting 100 % reduction of both TiO_2 and SiO_2. For the two other experiments, the addition of Al was added as 20 % over- and under stoichiometric. From the calculations done, seen in Section 3.2.1, approximately 26 g of Al was needed to get 100 % reduction, and 21 g and 31.5 g under- and over stoichiometric respectively.

As seen from both the scans from SEM and EPMA, three phases were observed in the reacted metal. From the EPMA analysis, these phases could be described as a Ti_5Si_4 phase with a high concentration of Ti and a TiSi phase with a high concentration of Si being detected in all experiments. While the third phase

was a bit different when looking at the concentrations of Al, Ca, and Ti. For the 100 % stoichiometric experiments, this phase was identified as a $TiSi_2$ phase with high Si concentration, while for the 120 % stoichiometric experiments this phase had a high concentration of Al, Ca and Si and was instead a CaAlSi phase.
As discussed in Section 5.2.1, a change in the color of the phases will occur when increasing the Al addition. The amount of Al in the phases from the EPMA analysis is summarized and compared in Table 5.4. For the over-stoichiometric experiments (9-12) with the highest content of Al, the phases observed were darker. This could be explained by the atomic number contrast, while the increase in the Al in the reacted metal is explained by the increase in the addition of Al added in the experiments. When considering the atomic number contrast, elements with higher atomic numbers will backscatter more electrons than elements with lower atomic numbers. Thus, phases with heavy elements appear brighter in the image. Ti has the highest atomic number when comparing Ti, Al, and Si, while Al has the lowest. Therefore, for the phases with a higher concentration of Al, the color gets darker in the image.

Table 5.4: Content of Al in the reacted metal from the experiments.

Exp.	**White area**	**Grey area**	**Black area**
	wt%	wt%	wt%
7	0.07	0.02	3.23
9	1.72	7.75	32.71
10	0.04	0.01	0.97
12	0.97	6.45	34.68

As discussed in theory and was observed in the study done by Wang et al. [39] and by Pourabdoli et al. [38], was that the content of Ti in the metal decreased with the increased Al addition and Al/slag ratio. To see if this was the case in these experiments, the overall concentrations of Ti, Si, and Al in the metal were calculated and plotted against the Al/slag ratio. The graphs are presented in Fig. 5.9. As can be seen, the same trend was observed as in [39] and [38]. The Ti concentration was highest in the under-stoichiometric experiments (8 and 11), with least added aluminium, while the concentration was lowest in the over-stoichiometric experiments (9 and 12) with the highest addition of aluminium.

The content of Si in the reacted metal to the Al/slag ratio is presented in Fig. 5.10. Here the highest concentration is seen in the 100 % stoichiometric experiment (7) at 1550 °C and at the over-stoichiometric experiment (12) at 1650 °C. The lowest concentration is seen in the under-stoichiometric experiment (8) for both temperatures, and in these experiments the concentration of SiO_2 in the reacted slag was high, approximately 27 wt% measured by EPMA. The high concentration of Ti and low concentration of Si in the reacted metal and the high concentration of SiO_2 in the reacted slag in the under-stoichiometric experiments (8 and 11) implies that the thermodynamic priority of reduction by Al is TiO_2>SiO_2, which was also concluded in the study by Wang et al. [39]. This is also supported by the overall concentration of Ti being higher than Si in the reacted metal, and also the fact that the wt%TiO_2 in the reacted slag was below 1 wt% for all the experiments.

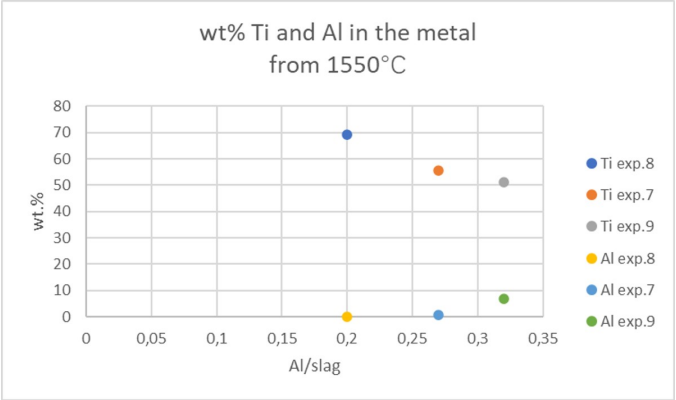

(a) Reacted alloy from 1550 °C.

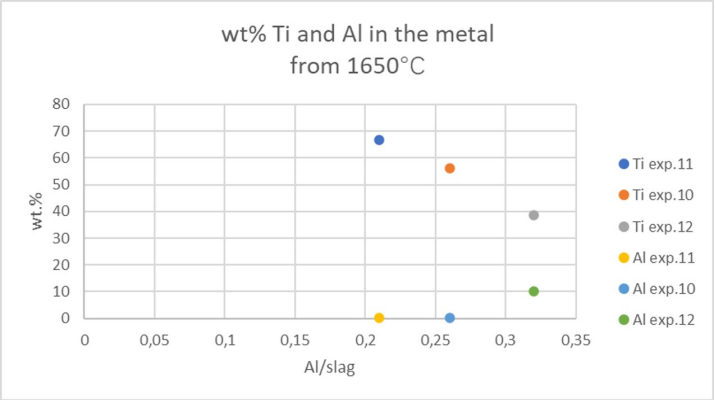

(b) Reacted alloy from 1650 °C.

Figure 5.9: Contents of Al and Ti in the alloy phase along with Al/slag ratio.

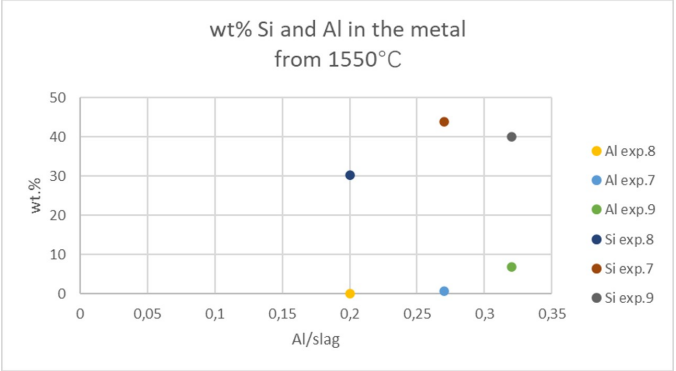

(a) Reacted alloy from 1550 °C.

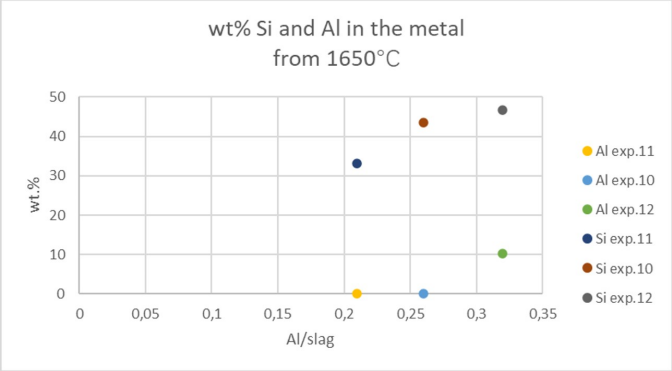

(b) Reacted alloy from 1650 °C.

Figure 5.10: Contents of Al and Si in the alloy phase along with Al/slag ratio.

5.2.3 Consistency with thermodynamic calculations

Thermodynamic calculations on the reactions were as mentioned done using the thermodynamic software FactSage. Related studies [59][60] have shown that the thermodynamic data from FactSage software [61] is reliable for the aluminothermic reduction process. As the thermodynamic calculations done on the aluminothermic reduction of slag 2 indicate, presented in Section 4.3.2, the phases in the reacted metal from the experiments performed at 1650 °C were calculated to be: Si_4Ti_5, $Ti_3Al_2Si_5$, $Ti_7Al_5Si_14$, B27, DO22, D13 and hP3, while the phases in the reacted slag were calculated to be: $Ca_3Ti_2O_7$-$Ca_3Ti_2O_6$, $CaAl_2O_4$, $Ca_3Al_2O_6$, Ca_2SiO_4 and a liquid phase. For the experiments performed at 1550 °C the phases in the reacted metal were calculated to be: Si_4Ti_5, $Ti_3Al_2Si_5$, D13, D022 and FCC-A1, while the phases in the slag were calculated to be: $Ca_3Ti_2O_7$-$Ca_3Ti_2O_6$, Si_4Ti_5, $CaAl_2O_4$, $Ca_3Al_2O_6$, Ca_2SiO_4 and $Ca_3Ti_2O_7$.

The overall concentrations of Al, Ca, Si, and Ti in the reacted metal were calculated using the EPMA

analysis and the area fraction of the three phases. The results were compared with the thermodynamic calculations and plotted in the Al-Si-Ti phase diagram seen in Fig. 5.11. The area fractions of each phase and the total content of the elements in both wt% and mol% are summarized in Table 5.5. As can be seen, when comparing the calculated results from EPMA with the thermodynamic calculations, there are significant deviations. Especially when looking at experiment 7, 100 % stoichiometric, performed at 1550 °C. The concentration of Al calculated with FactSage is rather high, while the concentrations of Ti and Si are low. A reason for the high content of Al in the metal calculated with FactSage could be that the amount of Al added during these calculations was much higher than the amount of Al added during the experiments. The thermodynamically calculated amount of Al needed and used in the calculations were 140 g for the experiments conducted at 1550 °C compared to the actual addition being 26 g, 21 g and 31.5 g respectively. While the calculated addition of Al needed for the experiments conducted at 1650 °C, was approximately 40 g. As can be seen, the difference in the amount of Al added in the experiments conducted at 1550 °C is much higher than the difference in the amount in the experiments conducted at 1650 °C. This could explain why the results from FactSage fits better for the higher temperature experiments.

Table 5.5: Area fractions of the phases and the overall content of the elements in the metal.

Experiment	**White area**	**Grey area**	**Black area**		
7	0.15	0.66	0.19		
9	0.54	0.38	0.09		
10	0.19	0.66	0.15		
12	0.20	0.62	0.18		
Experiment	**Element**	**Calculated** wt%	**Calculated** mol%	**FactSage** wt%	**FactSage** mol%
7	Si	43.96	56.96	7.97	8.25
	Al	0.63	0.85	74.22	80.03
	Ti	55.46	42.17	10.21	6.20
	Ca	0.02	0.02	7.60	5.52
9	Si	39.07	50.98		
	Al	6.63	9.01		
	Ti	49.75	38.08		
	Ca	2.11	1.93		
10	Si	43.47	56.80	27.73	32.86
	Al	0.16	0.22	29.52	36.42
	Ti	56.06	42.97	35.51	24.69
	Ca	0.01	0.01	7.25	6.02
12	Si	47.66	56.21		
	Al	10.38	12.75		
	Ti	39.34	27.22		
	Ca	4.62	3.82		

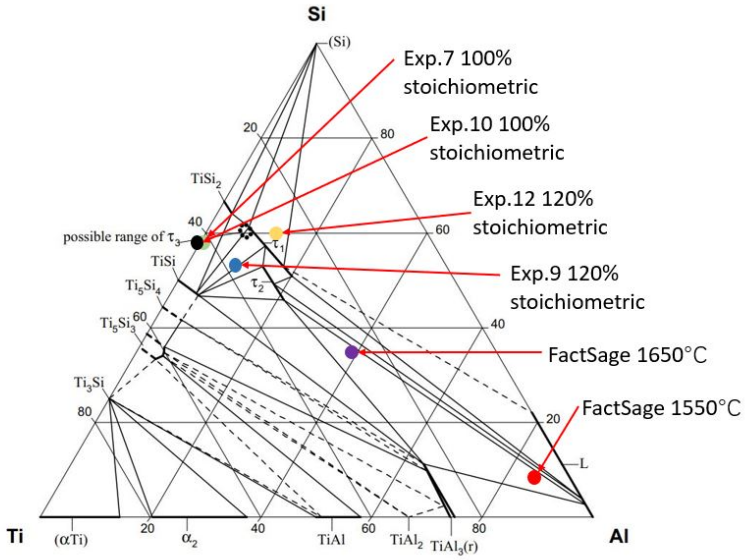

Figure 5.11: Ternary phase diagram with the calculated compositions from the EPMA analysis, and the compositions from FactSage.

The average concentrations of Al, Ca, Si, and Ti in the phases were calculated to compare with the phases calculated with FactSage. The calculations using analysis done with EPMA are presented in Appendix E.2 with the possible phases formed and plotted in the phase diagram seen in Fig. 5.12 with the possible solidification paths pointed out with black dotted lines.

By looking at the phases from the experiments performed at 1550 °C, there are differences between the phases formed in the 100 % stoichiometric experiment and the 120 % stoichiometric experiment. However, the TiSi rich phase with a high content of Ti is similar for both cases, and the phase formed is most likely a Ti_5Si_4 phase, marked with purple points in the phase diagrams. This is justified by looking at the contents of Ti and Si being in the range of 42 mol% to 48 mol% and 48 mol% to 51.5 mol% respectively.
Considering the two other phases, the content of Al is much higher in the 120 % stoichiometric experiment, 9.33 mol% and 36.08 mol% compared to 0.03 mol% and 3.84 mol%. This implies the formation of TiSi and $TiSi_2$ phases in the 100 % stoichiometric experiment, and formation of $Ti_7Al_5Si_{12}$ and FCC-A1 phases in the 120 % stoichiometric experiment. The FCC-A1 phase could also be the D13 phase calculated with FactSage with CaSiAl considering the high content of Ca, 18.35 mol%. These phases are shown as the grey and the black points in Fig. 5.12a and Fig. 5.12b respectively.
Comparing these phases found from the EPMA analysis with the phases calculated with FactSage, FCC-A1, Si_4Ti_5, TiSiAl, CaSiAl and $Ti_3Al_2Si_5$ it fits quite well. The same phases calculated with FactSage are detected from the calculations with the EPMA analysis. It is only the $\tau 1$ ($Ti_7Al_5Si_{12}$) phase that stands out, being found from the EPMA analysis and not from the FactSage calculations.

The same phases are seen for the experiments conducted at 1650 °C and the same trend with an increase in the content of Al for the 120 % stoichiometric experiment compared to the 100 % stoichiometric experiment. Regarding the phases calculated with FactSage for the experiments conducted at 1650 °C, TiSi, TiSiAl, CaSiAl, Si_4Ti_5, $Ti_3Al_2Si_5$ and $Ti_7Al_5Si_{14}$, respectively, corresponds well to the phases found from the EPMA analysis. As mentioned for the experiments performed at 1550 °C, the FCC-A1 phase is most likely a CaSiAl phase by looking at the relatively high content of Ca, 18.29 mol%.

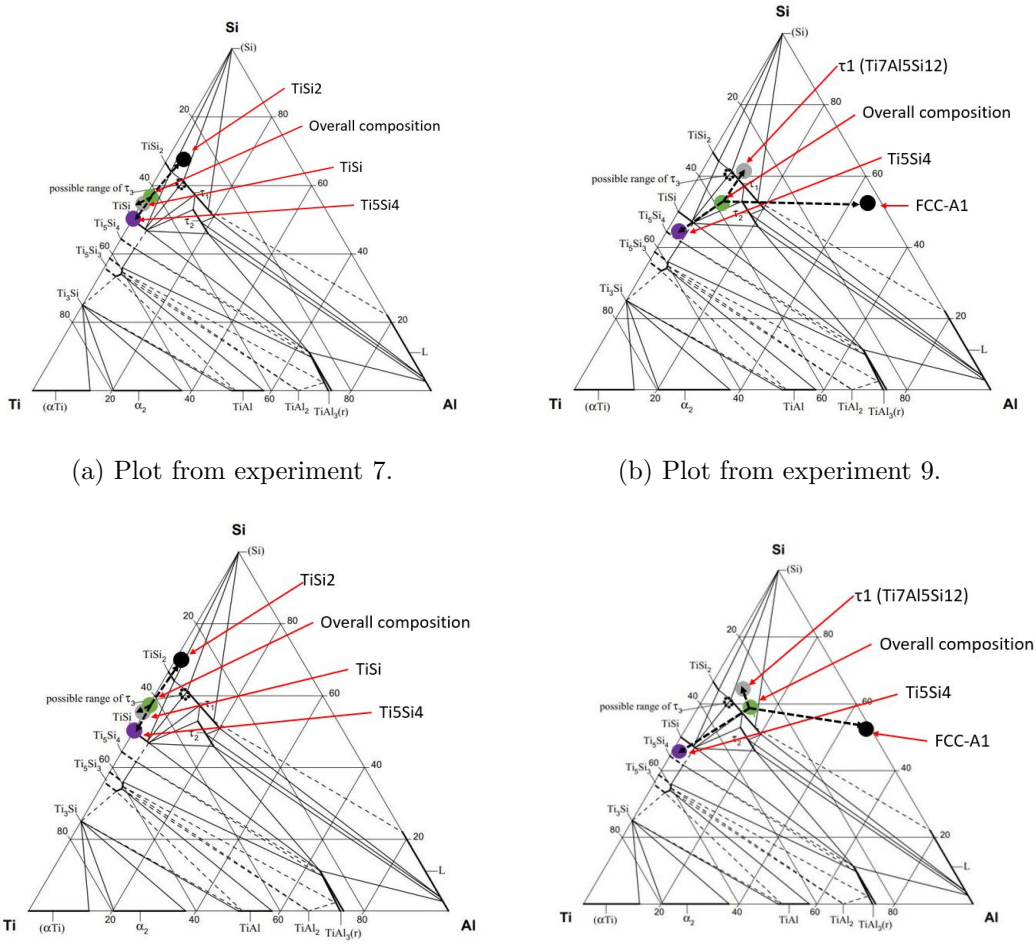

(a) Plot from experiment 7.

(b) Plot from experiment 9.

(c) Plot from experiment 10.

(d) Plot from experiment 12.

Figure 5.12: Plot of the overall content in the metal with the composition of the three phases.

Regarding the reacted slag, two phases could be detected in the scans from the SEM. However, it was quite difficult in some experiments to distinguish between the two phases. From the EDS measurements presented in Appendix D, no significant differences were observed in the contents of the elements. This is

therefore disregarded during the calculations, and the reacted slag is considered one phase in each experiment.
From the EPMA analysis presented in Table 5.6, the dominating phases in the reacted slag were Al_2O_3 and CaO as expected. As already mentioned, the concentration of Si in the reacted metal in the under-stoichiometric experiments was quite low. The reason for this is observed when looking at the concentration of SiO_2 in the same experiments. As can be seen from the table and by comparing the concentration of SiO_2 in the under-stoichiometric experiment with the 100 % stoichiometric and the over-stoichiometric experiments, a significant increase is observed. From being below 3 wt% to higher than 27 wt%.

When comparing with the thermodynamic calculated phases, what should be noticed is that there are no phases with TiO_2 because of the content of TiO_2 being below 2 mol%. So the thermodynamic phase $Ca_3Ti_2O_7$-$Ca_3Ti_2O_6$ calculated to be in the reacted slag from both temperatures was not found from the EPMA analysis. By looking at the calculated content and the calculations from FactSage, there are some deviations, but overall it fits quite well. The content of Al_2O_3 is the highest for both calculations, while the contents of SiO_2 and TiO_2 are low. As can be seen, thermodynamic calculations were only done for the 100 % stoichiometric experiments for both temperatures. The reason for this was that the composition of the slags at 1550 °C and at 1650 °C changed very little by adding and subtracting 20 % Al.

Looking at the plotted phases presented in Fig. 5.13 with the calculated compositions presented in Appendix E.2, the same phases are seen for the experiments with the same addition of Al.
For the 100 % stoichiometric experiments, 7 and 10 respectively, the phases are seen as the green points in the phase diagram. The phase can most likely be determined to be a $CaAl_2O_4$ phase by looking at the position of the points and the mol% of the oxides, 46 mol% to 49 mol% Al_2O_3, 49 mol% to 51 mol% CaO and 1 mol% to 3 mol% SiO_2 respectively.
For the 80 % stoichiometric experiments, 8 and 11, that had a high content of SiO_2, the phases are seen as the yellow points in the phase diagrams. As could be expected from the high SiO_2 content, the points are located closer to the SiO_2 than for the two other stoichiometric experiments. The phases are most likely a Ca_2SiO_4 phase for the experiment conducted at 1550 °C and a $Ca_2Al_2SiO_7$ phase for the experiment conducted at 1650 °C, by looking at the positions of the points and the mol% of the oxides, 14 mol% to 20 mol% Al_2O_3, 46 mol% to 50 mol% CaO and 28 mol% to 38 mol% SiO_2.
In the 100 % and 120 % stoichiometric experiments (7 and 10, and 9 and 12), the concentrations of the oxides were quite similar. The content of CaO, 54 mol% to 56 mol% was slightly higher, while the content of Al_2O_3, 42 mol% to 44 mol% was slightly lower, leading to a shift of the points towards the CaO-rich side of the phase diagram. The location of the blue points, combined with the mol% of the oxides, leads to the formation of the $Ca_3Al_2O_6$ phase, most likely.

Comparing these phases with the ones thermodynamically calculated for the experiments conducted at 1550 °C; $Ca_3Ti_2O_7$-$Ca_3Ti_2O_6$, $CaAl_2O_4$, $Ca_3Al_2O_6$, Ca_2SiO_4 and $Ca_3Ti_2O_7$, this fits quite well if the phases with TiO_2 is ignored. All of the before-mentioned phases were detected with the EPMA analysis. However, all of the phases found thermodynamically were found in the 100 % stoichiometric experiment, while only one phase was detected in each of the experiments from the EPMA analysis.

The same goes for the phases calculated thermodynamically for the experiments conducted at 1650 °C being $Ca_3Ti_2O_7$-$Ca_3Ti_2O_6$, $CaAl_2O_4$, $Ca_3Al_2O_6$ and Ca_2SiO_4. All of the phases were found from the calculations done with the EPMA analysis. This means that the thermodynamic calculations were in good agreement with the experimental results.

Table 5.6: Average content of the oxides in the reacted slag compared with the thermodynamic calculations.

Experiment	**Oxide**	**Calculated** wt%	**FactSage** wt%
7	Al_2O_3	66.31	57.87
	CaO	36.92	42.11
	SiO_2	1.11	2.84×10^{-3}
	TiO_2	0.29	3.26×10^{-3}
10	Al_2O_3	63.25	53.21
	CaO	46.72	46.72
	SiO_2	2.51	2.17×10^{-2}
	TiO_2	0.04	1.17×10^{-2}

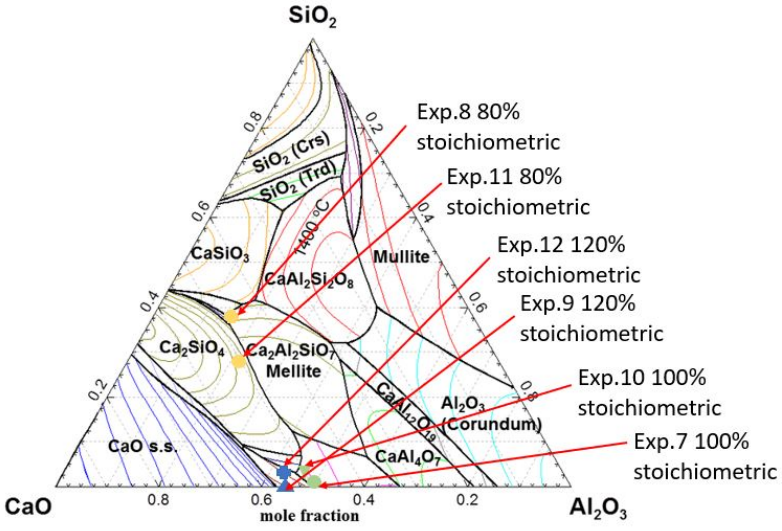

Figure 5.13: Composition (mol%) of the phases plotted.

5.2.4 Consistency with ICP-MS

The reacted metal from the 100 % and 120 % stoichiometric experiments conducted at 1550 °C were analysed with ICP-MS. This was done by ALS Scandinavia in Sweden. The results are seen in Table 5.7 and

compared with the calculated concentrations of Al, Si, and Ti from the EPMA analysis and the area fractions. As can be seen from the table, the results from the ICP-MS fits quite well with the calculated results. There are some deviations, but when considering that the overall concentrations were obtained from EPMA and image analysis, the results are in quite good agreement. The content of Ti is in the same range, between 50 wt% to 60 wt%, while the content of Si is a bit lower, between 35 wt% to 43 wt%, for both ICP-MS and EPMA analysis. Also, an increase in the Al content is observed when comparing the 100 % stoichiometric experiment with the 120 % stoichiometric experiment for both methods.

Table 5.7: Comparison of results from ICP-MS and the calculated content from EPMA analysis.

Experiment	**Al** wt%	**Si** wt%	**Ti** wt%	**Method**
7	3.61	35.8	58.1	**ICP-MS**
7	0.63	43.96	55.46	**EPMA**
9	6.05	35.2	60.6	**ICP-MS**
9	6.63	39.07	49.75	**EPMA**

5.2.5 Formation of carbides

No carbon is assumed present in the system. However, the graphite crucible will introduce carbon. According to thermodynamics, SiC will start to form when carbon is present. As can be seen in Fig. 5.14, some carbides are observed in the interface between the metal and the crucible, as the black areas, with high Si content and relatively high C content, as seen in point A and point B. As can be seen from the EDS measurements from Table 5.8, the amount of carbon decreases further into the metal while the amount of titanium increases. The bright area, point C in Fig. 5.14, close to the crucible, shows a high content of titanium, but the formation of TiC is not observed. This could imply that the reaction between Si and C is more favorable than the reaction between Ti and C.

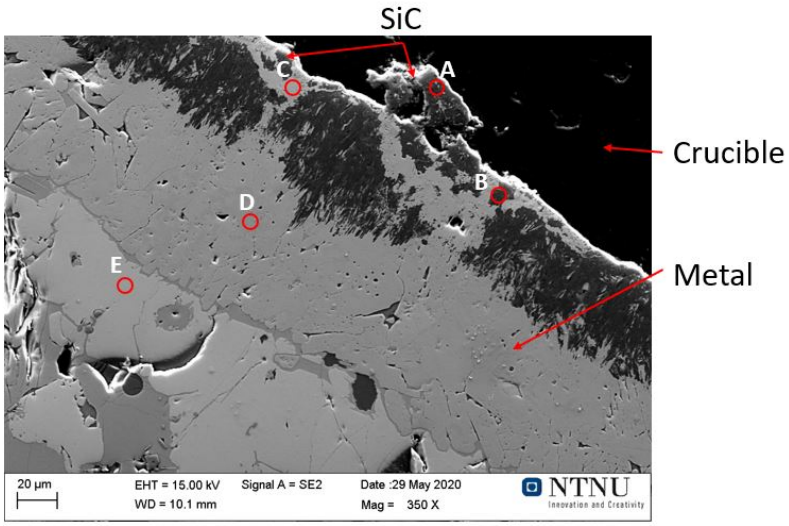

Figure 5.14: Metal and crucible with formation of SiC.

Table 5.8: EDS measurements from points in Fig. 5.14.

Element	**Point A**	**Point B**	**Point C**	**Point D**	**Point E**
	wt%	wt%	wt%	wt%	wt%
C	30.18	24.07	14.03	13.24	6.43
O	-	0.79	-	2.87	3.26
Al	1.57	6.15	1.42	1.02	1.75
Si	66.78	62.80	14.11	14.29	25.55
Ca	-	1.93	-	-	-
Ti	1.48	4.25	70.43	68.57	63.01

5.3 Comparison of the two cases

As mentioned, the theory and studies considering TiO_2 slags and Ti-alloys are limited. It is, therefore, difficult to somewhat explain the results obtained for the two different slags, why the reduction of TiO_2 to Ti did not occur in the experiments with the CaO-TiO_2 slag, and how reliable the results are.

The aluminothermic reduction process was successful for the ternary slag, while for the binary slag formation of TixOy oxides were observed instead. A reason for this could be the high affinity for oxygen that titanium has, explaining why only partially reduced titanium oxides phases (TixOy) were found with XRD for the experiments with the binary slag. However, another reason that could explain the differences in the obtained results is the amount of flux (CaO), amount of TiO_2, and amount of SiO_2 in the starting slags. In the study done by Pourabdoli et al. [38], the required flux was calculated on the basis of CaO/Al_2O_3 weight ratio. The results showed that increasing the CaO content in the slag up to 50 wt% caused the slag

melting point ant the slag fluidity to decrease, and as a result, the produced slag and alloy are separated more easily. These phenomena resulted in an improvement in the alloy yield. The concentration of Ti in the alloy increased as well with increased CaO/Al_2O_3 ratio, while a decrease in the content of Al was observed. In the study done by Maeda et al. [28] CaO-CaF_2 was used as a flux. In that study, the aluminothermic reduction reaction was fully completed in about 10 min. Comparing the content of the added flux with the added TiO_2 for the study done by Maeda et al. [28] and also the study that was done by Pourabdoli et al. [38] with the present study the differences are smaller than compared to the present work for the binary slag. The opposite is seen for the ternary slag, where the amount of CaO in the slag was higher than the amount of both TiO_2 and SiO_2, presented in Table 5.9. Also, the reacted slag and alloy were separated more easily from the experiments with the ternary slag, which can be explained by the decrease in the melting point and the fluidity of the slag by an increase in the amount of CaO as discussed by Pourabdoli et al. [38].

From the two studies [28] and [38], and by comparing the results from the two different slag systems, this could be a reason why no reduction of the binary slag occurred. However, more experiments with the binary slag system where the amount of CaO and TiO_2 is varied should be conducted before concluding.

Table 5.9: Comparison of the amount TiO_2 and flux added in the present study and the study done by Maeda et al. [28].

Study	Added TiO_2 g	Added flux g	Ratio TiO_2/flux
Maeda et al. [28]	5.00	2.51	1.99
Maeda et al. [28]	5.00	3.35	1.49
Present, binary	82.00	18.00	4.56
Present, ternary	25.00	50.00	0.50

Chapter 6

Conclusions

In this study, the aluminothermic reduction of titania and silica-containing slags have been evaluated. The effect of holding temperature and the amount of Al added were discussed, and the results were compared with thermodynamic calculations done with FactSage.

The overall conclusion that can be drawn from the results and the discussion is that aluminothermic reduction of the titania slag led to the formation of stable TixOy oxides in the reacted slag. In contrast, TiO_2 and SiO_2 in the titania-silica slag were reduced to Ti and Si in the reacted metal resulting in an TiSiAl alloy.

The results from the experiments with the CaO-TiO_2 slag can further be summarized as follows:

1. The reacted metal had a high concentration of Al and some formation of Al_2O_3. From the EPMA and SEM images, it was clear that the metal was homogeneous and that no reduction of TiO_2 to Ti had occurred during the holding time.
2. Three phases were observed in the reacted slag, a $CaTiO_3$ phase, a $Ca_3Ti_2O_7$ phase and a $CaAl_2O_4$ or a $Ca_{12}Al_{14}O_{33}$ phase. The concentration of TiO_2 was high in the $CaTiO_3$ phase, and a significant decrease was observed in the two other phases, from above 76 wt% to approximately 50 wt% and 20 wt%. The phase that could either be a $CaAl_2O_4$ or a $Ca_{12}Al_{14}O_{33}$ had a high content of CaO and Al_2O_3, 30 wt% to 33 wt% and 37 wt% to 50 wt% respectively. The calculated concentrations of the phases were quite similar for each experiment, also seen when plotting in the phase diagram, resulting in the formation of the same phases for each experiment. The concentration of TiO_2 was in the range of 4 wt% to 100 wt%, the concentration of CaO was in the range of 0.5 wt% to 43 wt%, while the concentration of Al_2O_3 was in the range of 0.14 wt% to 57 wt%.
3. The holding temperature did not affect the composition of the phases in the reacted slag or the reacted metal. However, the addition of Al lead to a change in the concentration of Al_2O_3. The content of Al_2O_3 increased in the experiments with 120 % stoichiometric addition of Al compared to the experiments with 100 % stoichiometric addition, from 3.31 wt% to 17.83 wt% and from 10.43 wt% to 12.97 wt% respectively.

4. From the XRD analysis of the reacted slag, it became clear that reduction of TiO_2 to Ti_2O_3 and TiO had occurred. This was as well expected from the theory and the Gibbs free energy of the reduction reactions of TiO_2. From the analysis it was seen that in the experiments conducted at 1550 °C TiO_2 had been reduced to Ti_2O_3, while in the experiments conducted at 1650 °C TiO_2 had been reduced to TiO. This could explain why a change in the color of the reacted slag was observed for the experiments performed at the highest temperature, from black to bronze.

5. Comparison of the phases found by the EPMA analysis and the ones thermodynamically calculated showed large deviations. The concentration of Al_2O_3 in the reacted slag calculated by FactSage was high, while the concentration in the reacted slag from the experiments conducted was low, around 76 wt% compared to being below 20 wt% respectively. This was, however, expected due to no reduction of TiO_2 to Ti, and hence, most of the Al still being in the metal.

The results from the experiments with CaO-SiO_2-TiO_2 slag can further be summarized as follows:

1. The reacted slag had a high content of Al_2O_3 and CaO, approximately 60 wt% and 40 wt%. In addition, the under-stoichiometric experiments had a high content of SiO_2 as well, above 27 wt%. From the EPMA analysis the phases in the reacted slag were calculated to be $CaAl_2O_4$ in the 100 % stoichiometric experiments, $Ca_3Al_2O_6$ in the 120 % stoichiometric experiments, while Ca_2SiO_4 and $Ca_2Al_2SiO_7$ were found in the 80 % stoichiometric experiments. The phases found from the EPMA analysis corresponded well with the ones calculated with FactSage, except from the calculated phases with TiO_2. The content of the oxides calculated thermodynamically corresponded well to the calculated content from EPMA, with 66 wt% Al_2O_3 from EPMA and 58 wt% Al_2O_3 from FactSage and 37 wt% CaO from EPMA and 42 wt% CaO from FactSage from the 100 % stoichiometric experiment conducted at 1550 °C.

2. The reacted metal had a high concentration of Ti and Si, and some Al and Ca. Three phases were detected, with varying content of Al, Ti, Ca and Si. From the EPMA analysis the phases were found to be Ti_5Si_4, TiSi, $TiSi_2$, $Ti_7Al_5Si_{12}$, AlSiTi and CaSiAl. The CaSiAl phase was found in the over-stoichiometric experiments due to a high content of Ca, approximately 18 wt%. As could be seen from plotting in the Al-Si-Ti phase diagram, the same phases were seen for the experiments with the same addition of Al, 80 % stoichiometric (exp. 8 and 11), 100 % stoichiometric (exp. 7 and 10) and 120 % stoichiometric (exp. 9 and 12).

3. The wt%Ti in the metal decreased when the addition of Al increased, from approximately 70 wt% to 40 wt%. The same trend was also observed in two studies performed by Wang et al.[39] and Pourabdoli et al.[38].

4. The holding temperature did not affect the composition or the microstructure in the reacted metal and the reacted slag. However, more parallels should be conducted to confirm this.

5. The composition in the reacted metal changed when the addition of Al increased. The concentrations of Al and Ca in the reacted slag were high in the over-stoichiometric experiments, 6.63 wt% and 10.38 wt% compared to 0.63 wt% and 0.16 wt% for Al, and 2.11 wt% and 4.62 wt% compared to 0.02 wt% and 0.01 wt% for Ca.

6. In the under-stoichiometric experiments a relatively high content of SiO_2 was observed, and this combined with the content of Si in the reacted metal being lower than the content of Ti implies that the thermodynamic priority of reduction by Al is TiO_2>SiO_2.
7. ICP-MS analysis done on the reacted metal from the 100 % and 120 % stoichiometric experiments fitted well with the calculated results from the EPMA analysis. The same trend with an increase in the concentration of Al was seen in the 120 % stoichiometric from the ICP-MS results.

Chapter 7

Future work

Since only one parallel was done for each temperature, more parallels should be conducted to see if the results are consistent. Especially considering experiments with slag 2 where the TiO_2 and most of the SiO_2 were reduced so that it was not only a coincidence.

Also, experiments with additional stirring should be conducted for experiments with slag 1 to see if this affects the reduction reaction, since the mixing was quite bad during the experiments. What could have been interesting as well is to vary to holding time to see how this affects the reduction of the content in the reacted slag and metal. In addition, increasing the holding temperature during the experiments with slag 1, since the TiO_2 was reduced to TiO at 1650 °C.

As seen from the thermodynamic calculations, the amount of aluminium needed to have 100 % reduction was significantly higher than the actual addition. Experiments with the addition of the calculated amount of aluminium should, therefore, be tried and compared with those done with the stoichiometric addition of aluminium.

More experiments on the binary slag with varying amount of CaO and TiO_2 should be conducted as well. The amount of CaO should be increased to see how this affects the reduction process.

Bibliography

[1] Zhigang Fang et al. “Powder metallurgy of titanium – past, present, and future”. In: *International Materials Reviews* (2017), pp. 1–53.

[2] Jiayun Zhang, Hiroyuki Matsuura, and Fumitaka Tsukihashi. “Processes for Recycling”. en. In: *Treatise on Process Metallurgy*. Elsevier, 2014, pp. 1507–1561. ISBN: 978-0-08-096988-6.

[3] François CARDARELLI. “A method for electrowinning of titanium metal or alloy from titanium oxide containing compound in the liquid state”. en. WO2003046258A2. June 2003.

[4] Katsutoshi Ono and Ryosuke O. Suzuki. “A new concept for producing Ti sponge: Calciothermic reduction”. In: *JOM* 54.2 (Feb. 2002), pp. 59–61. ISSN: 1543-1851.

[5] Jan-Christoph Stoephasius, Bernd Friedrich, and Jörg Hammerschmidt. “A new Processing Route for Titanium Alloys by Aluminothermic Reduction of Titanium Dioxide and Refining by ESR”. In: 2003.

[6] M R Bolívar. “Synthesis of Titanium via Magnesiothermic Re- duction of TiO2 (Pigment)”. en. In: (2009), p. 17.

[7] Rafael Bolivar and Bernd Friedrich. “Magnesiothermic Reduction from Titanium Dioxide to Produce Titanium Powder”. en. In: *Journal of Sustainable Metallurgy* 5.2 (June 2019), pp. 219–229. ISSN: 2199-3823, 2199-3831.

[8] S. Hassan-Pour et al. “Aluminothermic production of titanium alloys (Part 2): Impact of activated rutile on process sustainability”. en. In: *Metallurgical and Materials Engineering* 21.2 (2015), pp. 101–114. ISSN: 2217-8961.

[9] Alain Lasalmonie. “Intermetallics: Why is it so difficult to introduce them in gas turbine engines?” en. In: *Intermetallics*. EUROMAT 2005 "European Congress on Advanced Materials and Processes" 14.10 (Oct. 2006), pp. 1123–1129. ISSN: 0966-9795.

[10] C. Suryanarayana. “Synthesis of nanocomposites by mechanical alloying”. en. In: *Journal of Alloys and Compounds*. XVII International Symposium on Metastable, Amorphous and Nanostructured Materials 509 (June 2011), S229–S234. ISSN: 0925-8388.

[11] Z. Q Guan et al. “Phase formation during ball milling and subsequent thermal decomposition of Ti–Al–Si powder blends”. en. In: *Journal of Alloys and Compounds* 252.1 (May 1997), pp. 245–251. ISSN: 0925-8388.

[12] Chunxiang Cui et al. “Titanium alloy production technology, market prospects and industry development”. en. In: *Materials & Design* 32.3 (Mar. 2011), pp. 1684–1691. ISSN: 0261-3069.

[13] *Mineral commodity summaries 2020*. English. Report. Reston, VA, 2020, p. 204.

[14] Kamala Kanta Sahu et al. “An overview on the production of pigment grade titania from titania-rich slag”. In: *Waste Management & Research* 24.1 (Jan. 2006), pp. 74–79.
[15] Zhigang Zak Fang et al. “A New, Energy-Efficient Chemical Pathway for Extracting Ti Metal from Ti Minerals”. In: *Journal of the American Chemical Society* 135.49 (2013), pp. 18248–18251.
[16] R. R. Boyer. “Attributes, characteristics, and applications of titanium and its alloys”. In: *JOM* 62.5 (2010), pp. 21–24. ISSN: 1543-1851.
[17] *Titanium: applications and uses-Metalpedia*.
[18] Kevin J Cain. “Industrial Titanium Demand Forecast 2016”. en. In: (2016), p. 29.
[19] J. C. Fanning. “Military applications for beta titanium alloys”. In: *Journal of Materials Engineering and Performance* 14.6 (2005), pp. 686–690. ISSN: 1544-1024.
[20] William Gooch. “The Design and Application of Titanium Alloys to U.S. Army Platforms -2010”. In: 2010.
[21] Hamweendo Agripa and Ionel Botef. “Modern Production Methods for Titanium Alloys: A Review”. In: *Titanium Alloys*. Ed. by Maciej Motyka, Waldemar Ziaja, and Jan Sieniawsk. Rijeka: IntechOpen, 2019.
[22] Christoph Leyens and Manfred Peters. *Titanium and Titanium Alloys: Fundamentals and Applications*. en. John Wiley & Sons, Sept. 2003. ISBN: 978-3-527-30534-6.
[23] Bin Liu and Yong Liu. “27 - Powder metallurgy titanium aluminide alloys”. en. In: *Titanium Powder Metallurgy*. Ed. by Ma Qian and Francis H. (Sam) Froes. Boston: Butterworth-Heinemann, Jan. 2015, pp. 515–531. ISBN: 978-0-12-800054-0.
[24] *The Handbook of Advanced Materials: Enabling New Designs*. en. John Wiley & Sons, July 2004. ISBN: 978-0-471-46517-1.
[25] Hsueh-Chuan Hsu et al. “Structure and mechanical properties of as-cast Ti–Si alloys”. en. In: *Intermetallics* 47 (Apr. 2014), pp. 11–16. ISSN: 0966-9795.
[26] Spiros Zinelis, Athena Tsetsekou, and Triantafillos Papadopoulos. “Thermal expansion and microstructural analysis of experimental metal-ceramic titanium alloys”. en. In: *The Journal of Prosthetic Dentistry* 90.4 (Oct. 2003), pp. 332–338. ISSN: 0022-3913.
[27] Zhigang Zak Fang, Francis Froes, and Ying Zhang. *Extractive Metallurgy of Titanium: Conventional and Recent Advances in Extraction and Production of Titanium Metal*. en. Elsevier, Nov. 2019. ISBN: 978-0-12-817201-8.
[28] Masafumi Maeda et al. “Aluminothermic Reduction of Titanium Oxide”. In: *Materials Transactions, JIM* 34.7 (1993), pp. 599–603.
[29] Jan-Christoph Stoephasius and Bernd Friedrich. “Production of alfa-TiAl-Ingots by Aluminothermic Reduction of TiO2 and Refining by ESR”. In: 2005.
[30] George Zheng Chen, Derek J. Fray, and Tom W. Farthing. “Direct electrochemical reduction of titanium dioxide to titanium in molten calcium chloride”. en. In: *Nature* 407.6802 (Sept. 2000), pp. 361–364. ISSN: 1476-4687.
[31] Di Hu et al. “Development of the Fray-Farthing-Chen Cambridge Process: Towards the Sustainable Production of Titanium and Its Alloys”. In: *JOM* 70.2 (Feb. 2018), pp. 129–137. ISSN: 1543-1851.
[32] Yong Yan and Derek Fray. “Molten salt electrolysis for sustainable metals extraction and materials processing a review”. In: *Electrolysis: Theory, Types and Applications* (2010).

[33] Zhenyu Xing, Jun Lu, and Xiulei Ji. "A Brief Review of Metallothermic Reduction Reactions for Materials Preparation". en. In: *Small Methods* 2.12 (2018), p. 1800062. ISSN: 2366-9608.

[34] Erlend Lunnan Bjørnstad. "Mass Transfer Coefficients and Bubble Sizes in Oxidative Ladle Refining of Silicon". en. In: (), p. 76.

[35] Lide Arteta et al. "Metal Organic Frameworks as precursors for the manufacture of advanced catalytic materials". In: *Mater. Chem. Front.* 1 (2017).

[36] Aimin Liu et al. "Preparation of Al-Ti Master Alloys by Aluminothermic Reduction of TiO2 in Cryolite Melts at 960°C". In: *6th International Symposium on High-Temperature Metallurgical Processing*. Ed. by Tao Jiang et al. Cham: Springer International Publishing, 2016, pp. 239–246. ISBN: 978-3-319-48217-0.

[37] O Kubaschewski and W. A Dench. "The heats of formation in the systems titanium-aluminium and titanium-iron". en. In: *Acta Metallurgica* 3.4 (July 1955), pp. 339–346. ISSN: 0001-6160.

[38] M. Pourabdoli et al. "A New Process for the Production of Ferrotitanium from Titania Slag". In: *Canadian Metallurgical Quarterly* 46.1 (2007), pp. 17–23.

[39] Zhenyang Wang et al. "Production of ferrotitanium alloy from titania slag based on aluminothermic reduction". en. In: *Journal of Alloys and Compounds* 810 (Nov. 2019), p. 151969. ISSN: 0925-8388.

[40] Ryosuke O. Suzuki. "Calciothermic reduction of TiO2 and in situ electrolysis of CaO in the molten CaCl2". en. In: *Journal of Physics and Chemistry of Solids*. Proceedings of the 11th International Conference on High Temperature Materials Chemistry (HTMC-XI) 66.2 (Feb. 2005), pp. 461–465. ISSN: 0022-3697.

[41] P. P. Alexander. "US Patent 2.038. 402 (1936)". In: *US patent* 2.43 (1936), p. 363.

[42] Ryosuke O Suzuki. "Calciothermic Reduction and Simultaneous Electrolysis of CaO in the Molten CaCl2 : Some Modifications of OS Process". en. In: (), p. 8.

[43] O. Kubaschewski and W. A. Dench. "The free-energy diagram of the system titanium-oxygen". English. In: *J. Inst. Metals* Vol: 82 (Oct. 1953).

[44] S Miyazaki, T Oishi, and K Ono. "Thermodynamic properties of oxygen in the alpha and beta titanium-oxygen alloys at 800-1200 celsius". en. In: (), p. 7.

[45] M. Allibert and Verein Deutscher Eisenhuttenleute. *Slag atlas*. 2nd ed. Dusseldorf, Germany: Verlag Stahleisen, 1995. ISBN: 3-514-00457-9.

[46] V. Daněk and I. Nerád. "Phase diagram and structure of melts of the system CaOTiO2SiO2". In: *Chemical Papers* 56 (2002), pp. 241–246.

[47] Siddhartha Das. "The Al-O-Ti (Aluminum-oxygen-titanium) system". In: *Journal of Phase Equilibria* 23.6 (2002), pp. 525–536. ISSN: 1054-9714.

[48] Y. Mishin and Chr. Herzig. "Diffusion in the TiAl system". en. In: *Acta Materialia* 48.3 (Feb. 2000), pp. 589–623. ISSN: 1359-6454.

[49] E. Fischer. "Thermodynamic calculation of the O-Ti system". In: *Journal of Phase Equilibria* 18.4 (Aug. 1997), p. 338. ISSN: 1054-9714.

[50] J. L. Murray and H. A. Wriedt. "The OTi (Oxygen-Titanium) system". In: *Journal of Phase Equilibria* 8.2 (Apr. 1987), pp. 148–165. ISSN: 1054-9714.

[51] Bruno Ceccaroli, Eivind Ovrelid, and Sergio Pizzini. *Solar Silicon Processes: Technologies, Challenges, and Opportunities*. en. CRC Press, Oct. 2016. ISBN: 978-1-4987-4266-5.

[52] Soumitra Roy, Sergiy Divinski, and Aloke Paul. "Reactive diffusion in the Ti–Si system and the significance of the parabolic growth constant". In: *Philosophical Magazine* 94 (2014).

[53] Debashis Bandyopadhyay. "The Ti-Si-C system (Titanium-Silicon-Carbon)". In: *Journal of Phase Equilibria and Diffusion - J PHASE EQUILIB DIFFUS* 25 (2004), pp. 415–420.

[54] Takahiro Miki, Kazuki Morita, and Nobuo Sano. "Thermodynamic properties of titanium and iron in molten silicon". In: *Metallurgical and Materials Transactions B* 28.5 (1997), pp. 861–867. ISSN: 1543-1916.

[55] Pierre Perrot. *AlSiTi (Aluminium - Silicon - Titanium): Datasheet from Landolt-Börnstein - Group IV Physical Chemistry · Volume 11A4: "Light Metal Systems. Part 4" in SpringerMaterials*. Ed. by G. Effenberg and S. Ilyenko. Springer-Verlag Berlin Heidelberg.

[56] Zhi Li et al. "700 °C Isothermal Section of the AlTiSi Ternary Phase Diagram". In: *Journal of Phase Equilibria and Diffusion* 35.5 (2014), pp. 564–574. ISSN: 1863-7345.

[57] Marina Bulanova et al. "Phase equilibria in the alpha-Ti-Al-Si region of the Ti-Si-Al system". In: *Journal of Phase Equilibria and Diffusion* 25.3 (Aug. 2004), pp. 209–229. ISSN: 1863-7345.

[58] In-Ho Jung. "Overview of the applications of thermodynamic databases to steelmaking processes". en. In: *Calphad* 34.3 (Sept. 2010), pp. 332–362. ISSN: 0364-5916.

[59] Vitaly Babyuk, Bernd Friedrich, and Vladyslav Sokolov. "Investigations of Liquid Phase Aluminothermic Reduction of Ilmenite". en. In: *World of Metallurgy* 5 (2007), p. 7.

[60] Christopher W Bale. "FactSage Thermochemical Software and Databases". en. In: (), p. 40.

[61] C. W. Bale et al. "Reprint of: FactSage thermochemical software and databases, 2010–2016". en. In: *Calphad*. Christopher W. Bale Symposium - Thermodynamic Applications, Optimizations and Simulations in High Temperature Processes 55 (Dec. 2016), pp. 1–19. ISSN: 0364-5916.

Appendix A

Temperature profiles

The temperature profiles from the melting and remelting of the two slags are presented.

A.1 $CaO\text{-}TiO_2$ slag

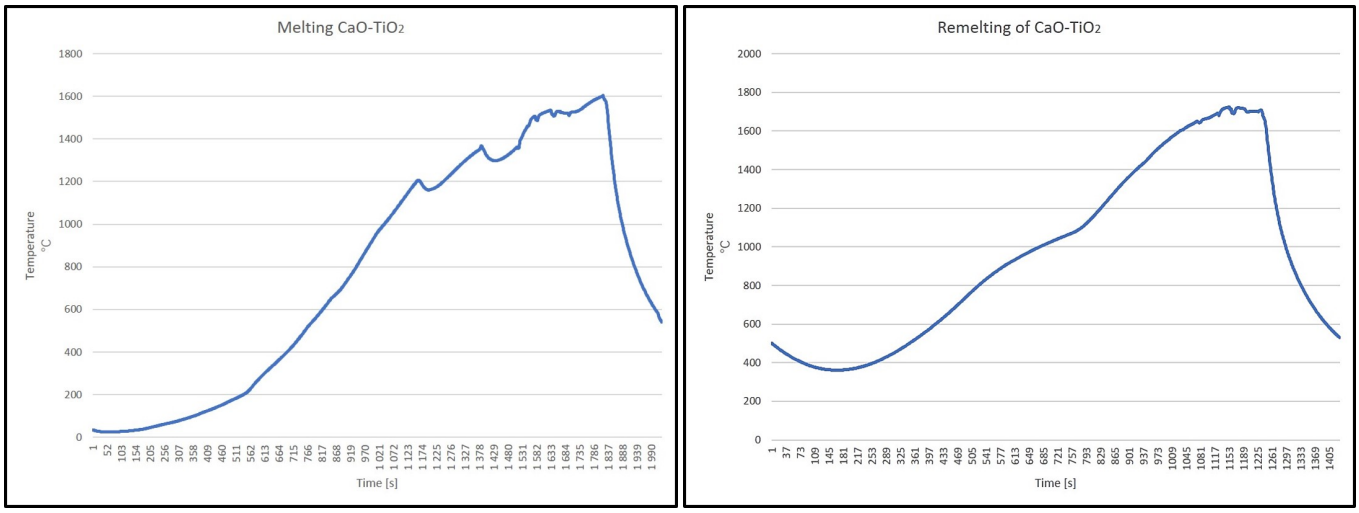

(a) Melting of the slag.

(b) Remelting of the slag.

A.2 CaO-SiO_2-TiO_2 slag

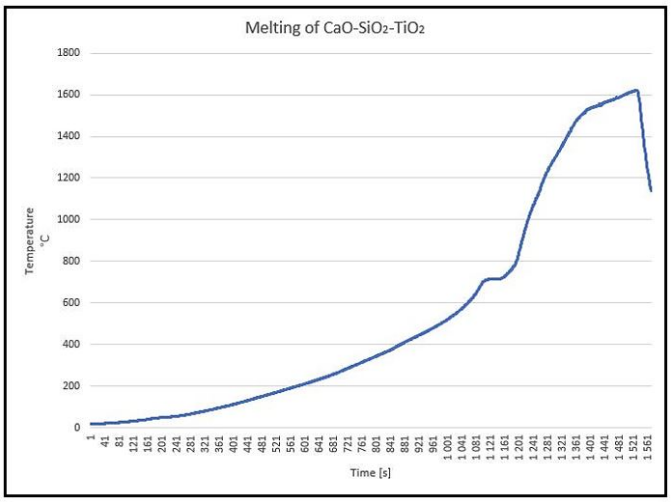

(a) Melting of the slag.

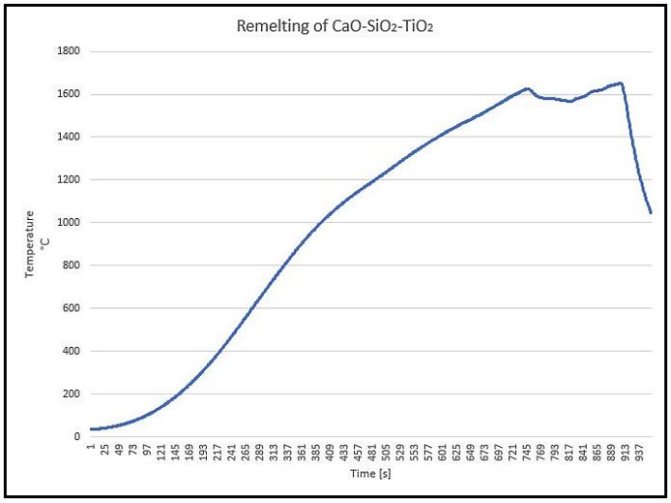

(b) Remelting of the slag.

Appendix B

Heating and cooling rates

The heating and cooling profiles for each experiment are presented, with the calculated heating- and cooling rates presented in tables.

B.1 Experiments with $CaO\text{-}TiO_2$ slag

B.1.1 Experiment 1, 1550 °C

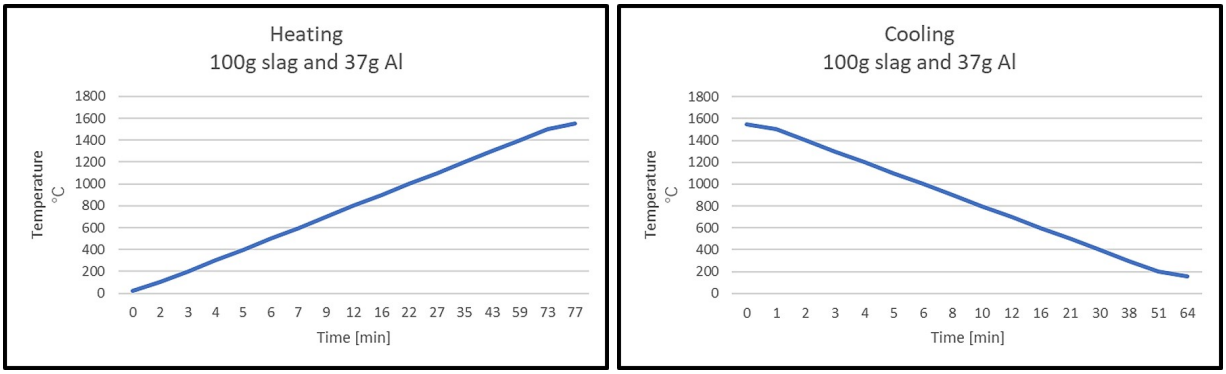

Figure B.1: Experiment with 100 g slag and 37 g Al.

Table B.1: Heating and cooling rates.

	Time (min)	Temp. range (°C)	Rate ($°C\,min^{-1}$)
Heating	77	19.58-1550	19.88
Cooling	64	1550-155	21.80
Cooling	3	1550-1300	83.33

B.1.2 Experiment 2, 1550 °C

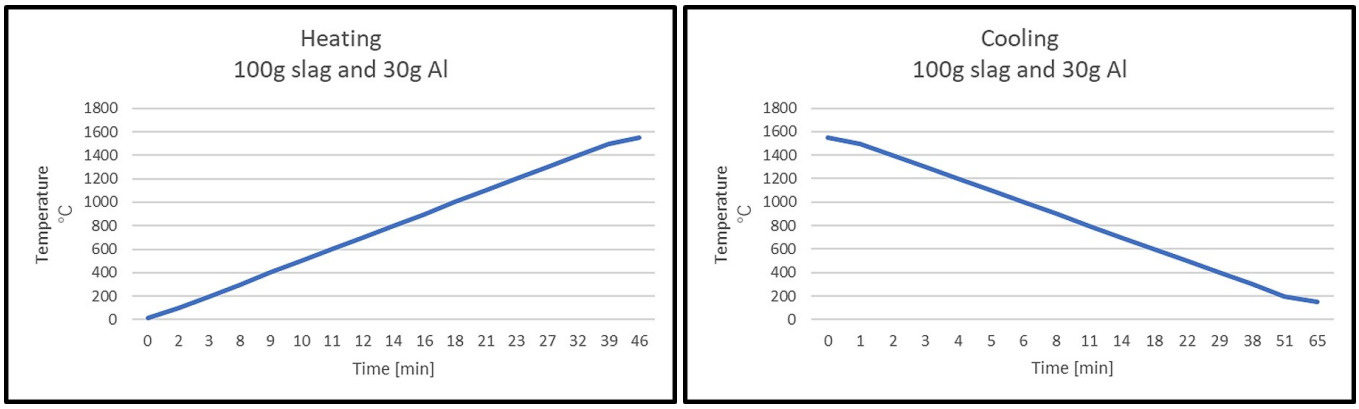

Figure B.2: Experiment with 100 g slag and 30 g Al.

Table B.2: Heating and cooling rates.

	Time (min)	Temp. range (°C)	Rate ($°C\,min^{-1}$)
Heating	46	18.73-1550	33.29
Cooling	65	1550-150	21.54
Cooling	3	1550-1300	83.33

B.1.3 Experiment 3, 1550 °C

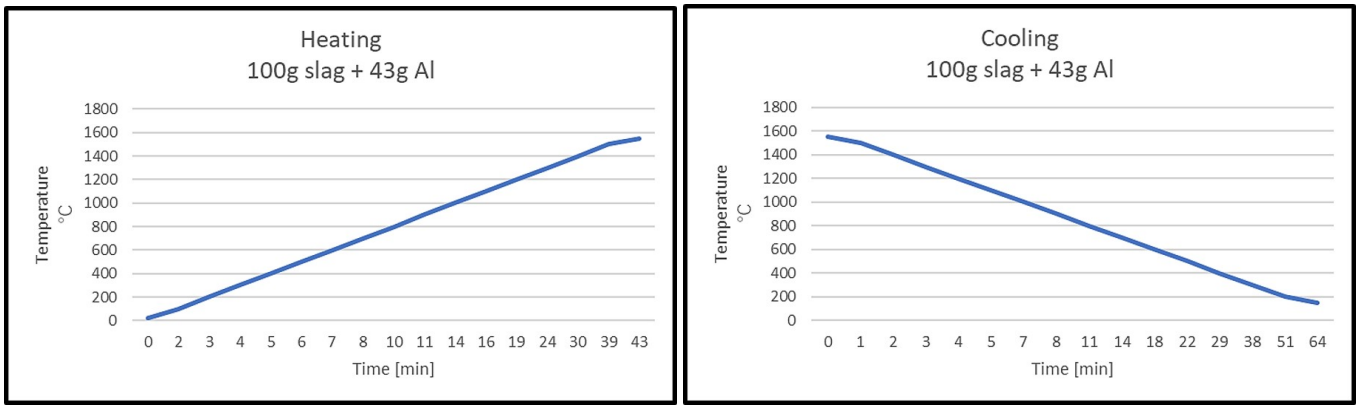

Figure B.3: Experiment with 100 g slag and 43 g Al.

Table B.3: Heating and cooling rates.

	Time (min)	Temp. range (°C)	Rate (°C min^{-1})
Heating	43	19.54-1550	35.59
Cooling	64	1550-150	21.88
Cooling	3	1550-1300	83.33

B.1.4 Experiment 4, 1650 °C

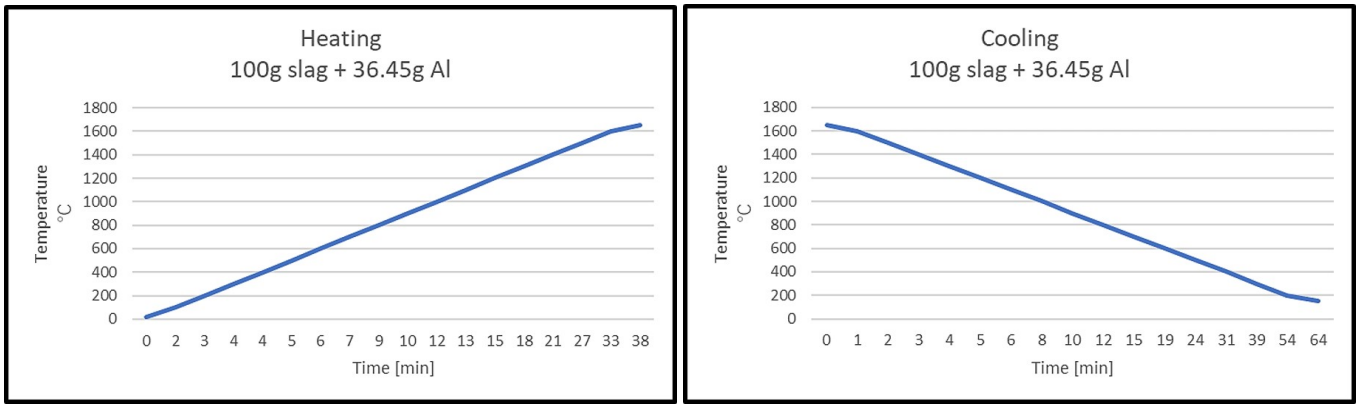

Figure B.4: Experiment with 100 g slag and 36.45 g Al.

Table B.4: Heating and cooling rates.

	Time (min)	Temp. range (°C)	Rate ($°C\,min^{-1}$)
Heating	38	20.2-1650	42.89
Cooling	64	1650-150	23.44
Cooling	4	1650-1300	87.5

B.1.5 Experiment 5, 1650 °C

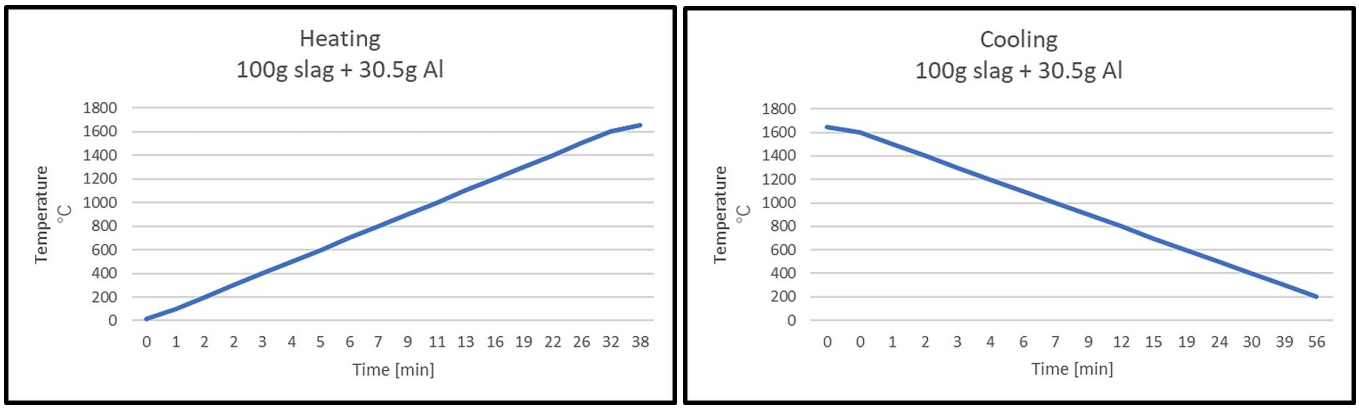

Figure B.5: Experiment with 100 g slag and 30.5 g Al.

Table B.5: Heating and cooling rates.

	Time (min)	Temp. range (°C)	Rate ($°C\,min^{-1}$)
Heating	38	18.73-1650	42.93
Cooling	56	1650-200	25.89
Cooling	3	1650-1300	116.67

B.1.6 Experiment 6, 1650 °C

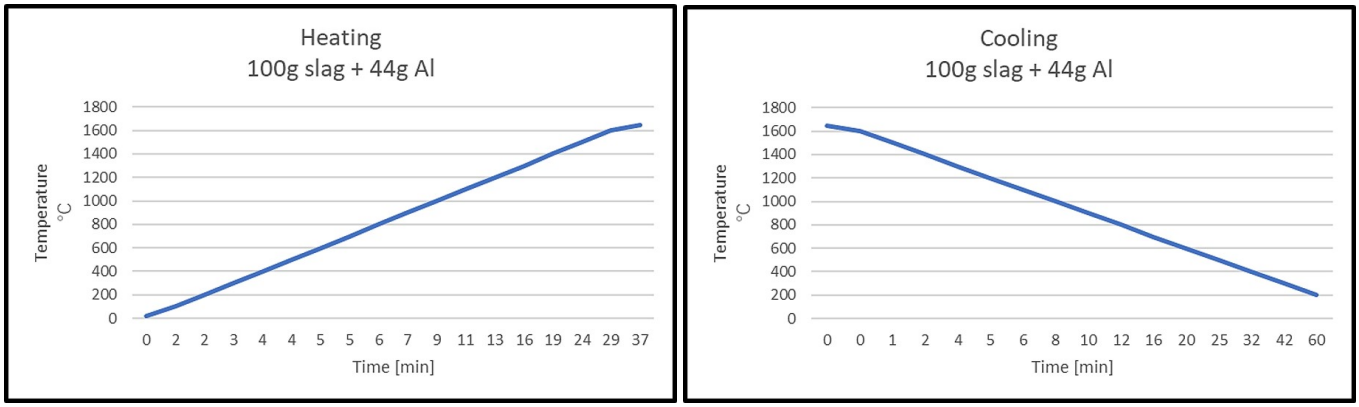

Figure B.6: Experiment with 100 g slag and 44 g Al.

Table B.6: Heating and cooling rates.

	Time (min)	Temp. range (°C)	Rate ($°C\,min^{-1}$)
Heating	37	18.10-1650	44.11
Cooling	60	1650-200	24.17
Cooling	4	1650-1300	87.5

B.2 Experiments with CaO-SiO_2-TiO_2 slag

B.2.1 Experiment 7, 1550 °C

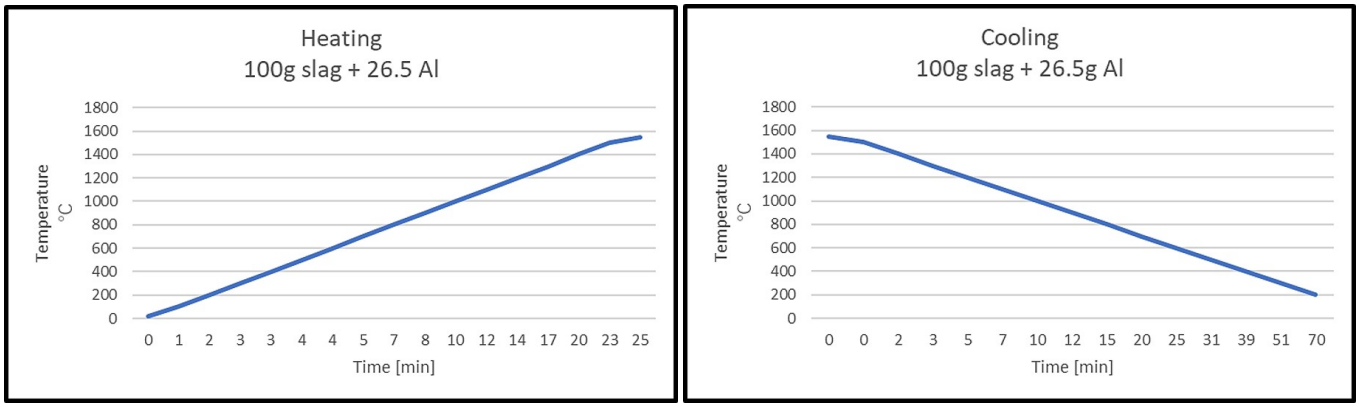

Figure B.7: Experiment with 100 g slag and 26.5 g Al.

Table B.7: Heating and cooling rates.

	Time (min)	Temp. range (°C)	Rate (°C min^{-1})
Heating	25	19.12-1550	61.24
Cooling	70	1550-200	19.29
Cooling	3	1550-1300	83.33

B.2.2 Experiment 8, 1550 °C

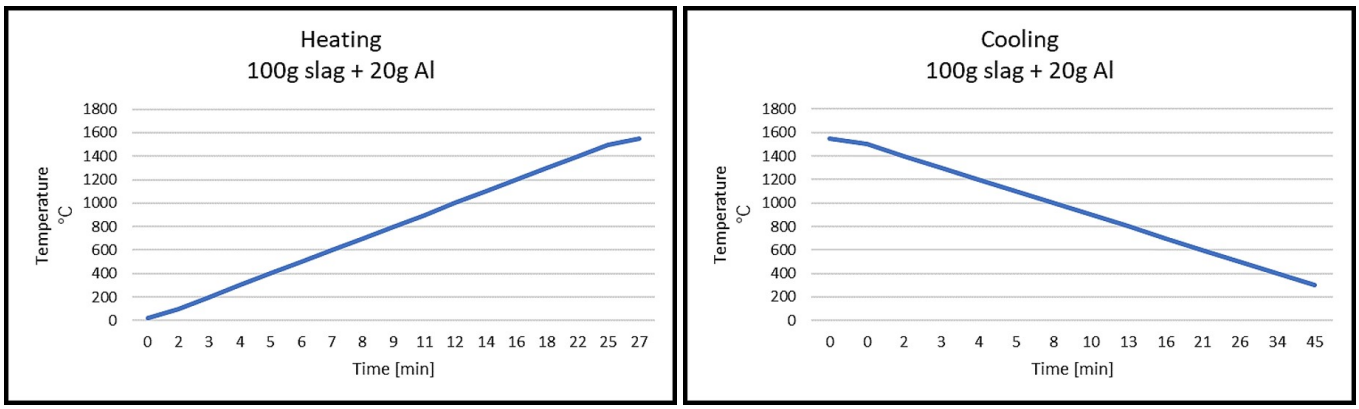

Figure B.8: Experiment with 100 g slag and 20 g Al.

Table B.8: Heating and cooling rates.

	Time (min)	Temp. range (°C)	Rate (°C min^{-1})
Heating	27	18.34-1550	56.73
Cooling	45	1550-300	27.78
Cooling	3	1550-1300	83.33

B.2.3 Experiment 9, 1550 °C

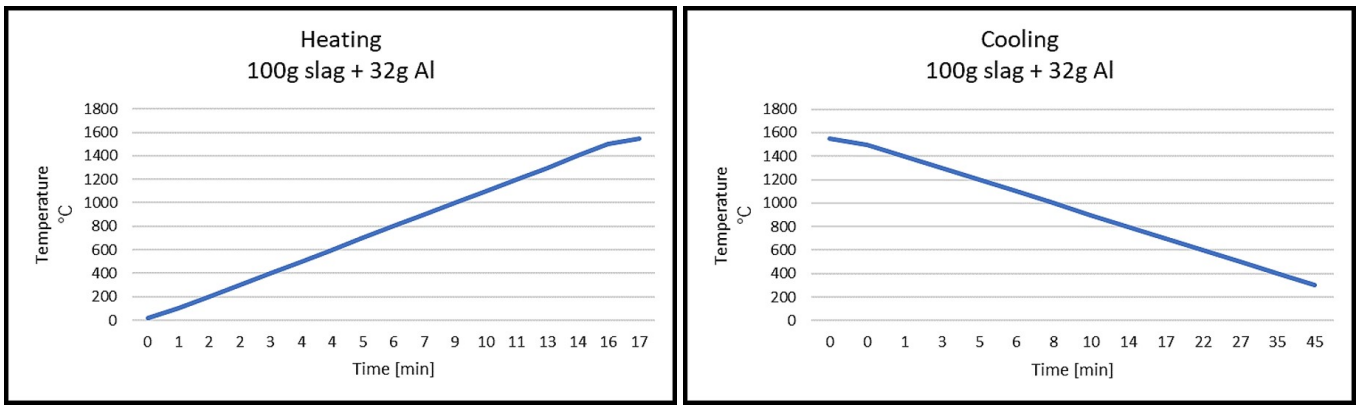

Figure B.9: Experiment with 100 g slag and 32 g Al.

Table B.9: Heating and cooling rates.

	Time (min)	Temp. range (°C)	Rate ($°C\,min^{-1}$)
Heating	17	22.14-1550	89.87
Cooling	45	1550-300	27.78
Cooling	3	1550-1300	83.33

B.2.4 Experiment 10, 1650 °C

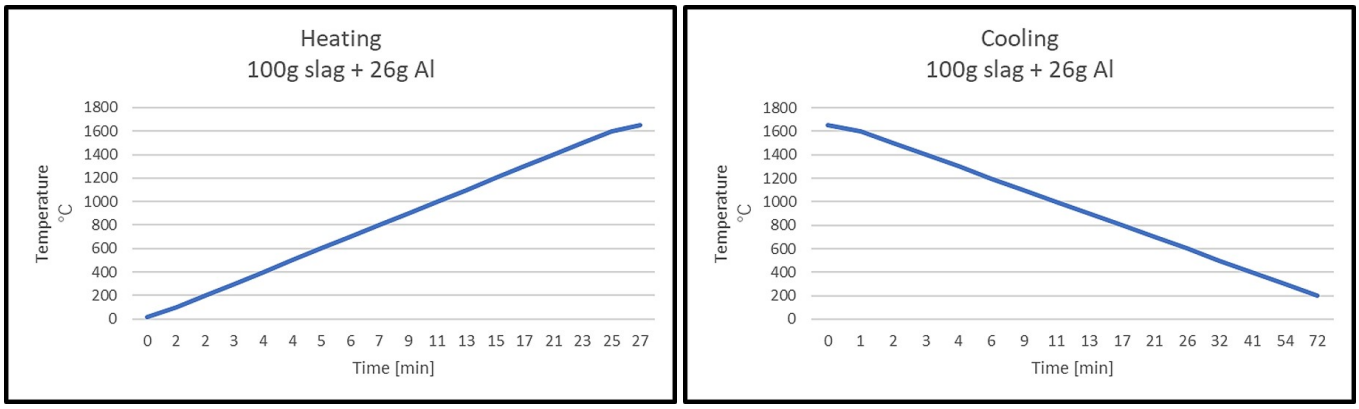

Figure B.10: Experiment with 100 g slag and 26 g Al.

Table B.10: Heating and cooling rates.

	Time (min)	Temp. range (°C)	Rate ($°C\,min^{-1}$)
Heating	27	18.54-1650	60.42
Cooling	72	1650-200	20.14
Cooling	4	1650-1300	87.50

B.2.5 Experiment 11, 1650 °C

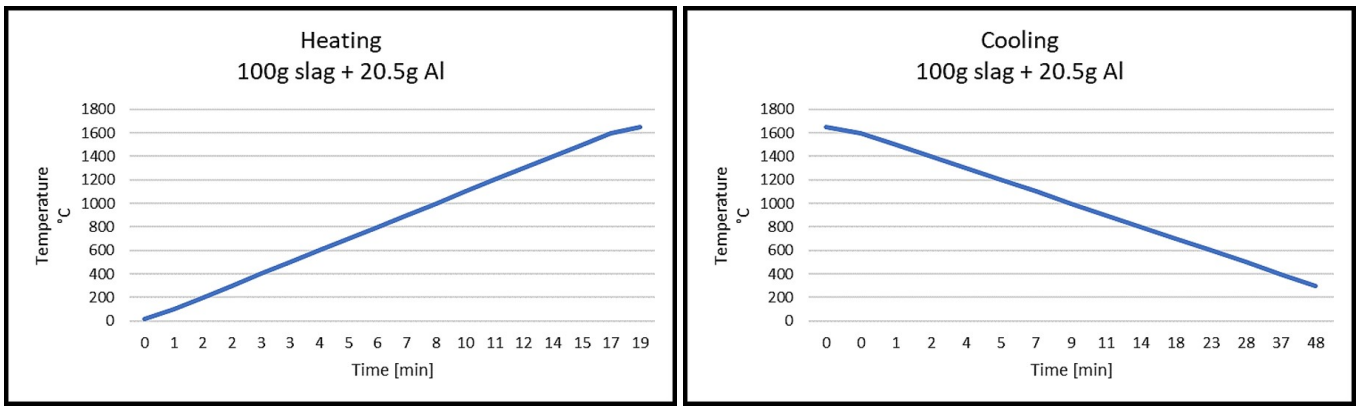

Figure B.11: Experiment with 100 g slag and 20.5 g Al.

Table B.11: Heating and cooling rates.

	Time (min)	Temp. range (°C)	Rate ($°C\,min^{-1}$)
Heating	19	17.92-1650	85.90
Cooling	48	1650-300	28.13
Cooling	4	1650-1300	87.50

B.2.6 Experiment 12, 1650 °C

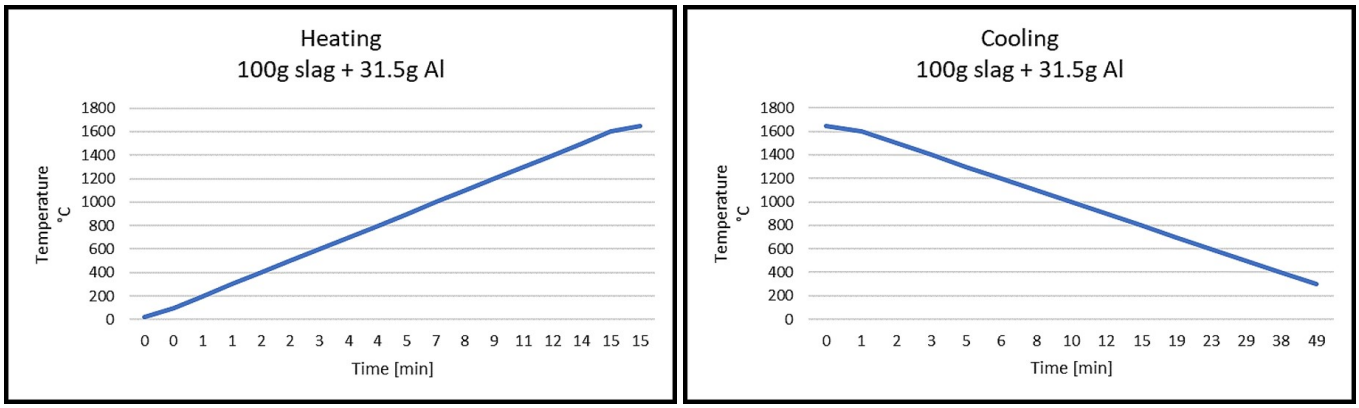

Figure B.12: Experiment with 100 g slag and 31.5 g Al.

Table B.12: Heating and cooling rates.

	Time (min)	Temp. range (°C)	Rate (°C min^{-1})
Heating	15	22.61-1650	108.49
Cooling	49	1650-300	27.55
Cooling	5	1650-1300	70.00

Appendix C

EDS results from CaO-TiO_2 slag

In this appendix, the results from EDS analyses from the SEM scans presented in Section 4.1.2 are seen. The results corresponds well with the EPMA analyses.

Table C.1: EDS measurements of points in Fig. 4.4a.

Element	Point A wt%	Point B wt%	Point C wt%	Point D wt%	Point E wt%
O	0.07	0.98	1.06	0.66	0.72
Al	99.93	99.02	98.94	99.34	99.28

Table C.2: EDS measurements of points in Fig. 4.4b.

Element	Point A wt%	Point B wt%	Point C wt%	Point D wt%	Point E wt%
N	-	-	-	-	1.08
O	35.87	43.77	28.35	17.68	35.96
Al	0.64	19.67	0.81	0.85	0.63
Cl	-	-	-	4.59	-
K	-	-	-	6.07	-
Si	-	2.89	-	-	-
Ca	0.99	31.63	1.39	1.27	1.00
Ti	62.50	2.03	69.45	69.54	61.34

Table C.3: EDS measurements of points in Fig. 4.6a.

Element	Point A wt%	Point B wt%	Point C wt%	Point D wt%	Point E wt%
O	0.11	30.65	-	-	-
Al	99.39	69.26	99.63	99.75	100.00
Ca	0.10	0.04	0.07	0.19	-
Ti	0.40	0.05	0.30	0.06	-

Table C.4: EDS measurements of points in Fig. 4.6b.

Element	Point A wt%	Point B wt%	Point C wt%	Point D wt%	Point E wt%
O	32.97	39.12	38.97	39.16	38.60
Al	2.13	22.47	21.60	22.12	20.48
Ca	1.23	12.28	12.00	12.52	27.42
Ti	63.67	26.13	27.43	26.20	13.50

Table C.5: EDS measurements of points in Fig. 4.8a.

Element	Point A wt%	Point B wt%	Point C wt%	Point D wt%	Point E wt%
O	-	-	33.79	-	10.80
Al	73.33	100.00	66.21	100.00	89.20
Si	0.98	-	-	-	-
Ca	1.72	-	-	-	27.42
Ti	-	-	-	-	13.50
Fe	23.98	-	-	-	-

Table C.6: EDS measurements of points in Fig. 4.8b.

Element	Point A wt%	Point B wt%	Point C wt%	Point D wt%	Point E wt%
N	-	-	1.52	1.71	-
O	42.78	41.58	31.93	34.36	39.28
Al	40.70	31.90	2.13	1.01	13.39
Ca	15.51	12.14	1.31	1.02	6.74
Ti	1.01	14.39	63.11	61.90	40.59

Table C.7: EDS measurements of points in Fig. 4.10a.

Element	Point A wt%	Point B wt%	Point C wt%	Point D wt%
C	-	-	-	68.87
O	0.24	0.11	1.59	2.57
Al	71.91	99.15	98.13	23.05
Si	3.06	-	-	0.21
Mo	-	-	-	2.75
K	-	-	-	1.77
Ca	24.72	0.07	0.23	0.69
Ti	0.07	0.67	0.04	0.08

Table C.8: EDS measurements of points in Fig. 4.10b.

Element	Point A wt%	Point B wt%	Point C wt%	Point D wt%	Point E wt%
N	2.04	2.13	-	2.17	2.09
O	28.16	26.94	40.47	26.73	26.70
Al	0.28	0.45	31.40	0.47	0.37
Ca	0.54	0.28	26.64	0.53	0.39
Ti	68.97	70.20	3.49	70.10	70.46

Appendix D

EDS results from CaO-SiO_2-TiO_2 slag

Table D.1: EDS measurements of points in Fig. 4.17a.

Element	Point A wt%	Point B wt%	Point C wt%	Point D wt%	Point E wt%
O	2.65	1.27	3.41	2.89	1.34
Al	0.44	2.26	0.94	0.78	3.97
Si	30.71	51.05	26.27	26.53	32.39
Ca	0.27	0.11	0.31	0.21	0.14
Ti	65.94	45.31	69.07	69.59	30.57
Fe	-	-	-	-	31.59

Table D.2: EDS measurements of points in Fig. 4.17b.

Element	Point A wt%	Point B wt%	Point C wt%	Point D wt%	Point E wt%
O	22.44	46.48	61.24	58.34	61.42
Br	-	-	-	19.36	-
Al	37.61	32.40	29.36	13.91	27.55
Si	0.55	0.19	0.51	-	0.82
Ca	39.31	20.88	8.86	8.38	10.17
Ti	0.09	0.04	0.04	-	0.04

Table D.3: EDS measurements of points in Fig. 4.19a.

Element	Point A wt%	Point B wt%	Point C wt%	Point D wt%	Point E wt%
O	2.66	1.36	0.94	1.82	2.51
Al	1.75	7.90	36.32	8.02	1.63
Si	26.61	44.99	34.08	44.59	26.58
Ca	0.14	0.17	28.18	0.18	0.22
Ti	68.83	45.57	0.49	45.39	69.94

Table D.4: EDS measurements of points in Fig. 4.19b.

Element	Point A wt%	Point B wt%	Point C wt%	Point D wt%
C	-	-	12.08	-
O	73.92	74.82	67.64	73.82
Al	23.92	24.73	19.17	23.31
Si	0.70	0.46	0.18	1.66
Ca	1.45	0.00	0.94	1.15
Ti	0.00	0.00	0.00	0.05

Appendix E

Calculation of the phases in the phase diagrams

The calculated contents of the oxides in the reacted slag and the elements in the reacted metal with respect to the area fractions are presented. The area fractions of the phases were calculated using ImageJ and the contents were calculated from the EPMA analyses.

E.1 Phases from the CaO-TiO_2 slag

Table E.1: Composition of the three phases in the reacted slag in wt% plotted in Fig. 5.6.

Exp.	**Oxide**	**TiO_2 phase** wt%	**TiO_2-CaO-Al_2O_3 phase** wt%	**CaO-Al_2O_3 phase** wt%
	Al_2O_3	1.31	0.14	37.43
	CaO	0.91	42.13	29.99
1	TiO_2	99.73	55.16	4.91
Possible phases		**TiO_2**	**$Ca_3Ti_2O_7$** or **$CaTiO_3$**	**$CaAl_2O_3$** or **$Ca_{12}Al_{14}O_{33}$**
Points in	Fig. 5.6a	Purple	Grey	Black
	Al_2O_3	9.25	34.36	56.42
	CaO	17.26	21.07	33.24
3	TiO_2	76.35	49.56	10.60
Possible phases		**$CaTiO_3$** or **TiO_2**	**$Ca_3Ti_8Al_{12}O_{37}$**	**$CaAl_2O_4$**
Points in	Fig. 5.6b	Purple	Grey	Black
	Al_2O_3	2.79	2.43	49.15
	CaO	1.27	42.49	33.08
4	TiO_2	104.30	52.15	22.87
Possible phases		**TiO_2**	**$Ca_3Ti_2O_7$** or **$CaTiO_3$**	**$CaAl_2O_4$** or **$Ca_{12}Al_{14}O_{33}$**
Points in	Fig. 5.6c	Purple	Grey	Black
	Al_2O_3	1.41	3.25	47.29
	CaO	0.99	42.84	33.87
6	TiO_2	108.46	50.58	23.14
Possible phases		**TiO_2**	**$Ca_3Ti_2O_7$** or **$CaTiO_3$**	**$CaAl_2O_4$** or **$Ca_{12}Al_{14}O_{33}$**
Points in	Fig. 5.6d	Purple	Grey	Black

E.2 Phases from the CaO-SiO_2-TiO_2 slag

Table E.2: Composition of the three phases in the reacted metal in mol% plotted in Fig. 5.12.

Exp.	**Element**	**White phase** mol%	**Grey phase** mol%	**Black phase** mol%
	Si	48.09	53.60	65.93
	Al	0.10	0.03	3.84
7	Ti	48.30	43.44	28.26
	Ca	0.02	0.01	0.05
Possible phases		**Ti_5Si_4**	**TiSi**	**$TiSi_2$**
Points in	Fig. 5.12a	Purple	Grey	Black
	Si	42.41	60.04	41.36
	Al	2.52	9.33	36.08
9	Ti	51.58	28.77	2.15
	Ca	0.02	0.01	18.35
Possible phases		**Ti_5Si_4**	**τ1 ($Ti_7Al_5Si_{12}$)**	**FCC-A1** or **CaSiAl**
Points in	Fig. 5.12b	Purple	Grey	Black
	Si	47.88	53.54	68.38
	Al	0.06	0.02	1.16
10	Ti	48.58	43.09	28.52
	Ca	0.01	0.00	0.01
Possible phases		**Ti_5Si_4**	**TiSi**	**$TiSi_2$**
Points in	Fig. 5.12c	Purple	Grey	Black
	Si	43.20	62.30	42.19
	Al	1.40	7.61	36.80
12	Ti	51.43	28.07	1.34
	Ca	0.05	0.03	18.29
Possible phases		**Ti_5Si_4**	**τ1 ($Ti_7Al_5Si_{12}$)**	**FCC-A1** or **CaSiAl**
Points in	Fig. 5.12d	Purple	Grey	Black

Table E.3: Composition of the phases in the reacted slag from EPMA analyses plotted in Fig. 5.13.

Experiment	**Al_2O_3** mol%	**CaO** mol%	**SiO_2** mol%	**TiO_2** mol%	**Point** Fig. 5.13	**Possible phases**
7	48.87	49.47	1.39	0.28	Circle, green	$CaAl_2O_4$
8	14.26	46.15	37.80	1.79	Cross, yellow	Ca_2SiO_4
9	43.78	55.52	0.70	0.01	Triangle-up, blue	$Ca_3Al_2O_6$
10	46.04	50.83	3.10	0.04	Triangle-down, green	$CaAl_2O_4$
11	20.86	50.33	28.14	0.67	Circle, yellow	$Ca_2Al_2SiO_7$
12	42.25	54.70	3.04	0.01	Cross, blue	$Ca_3Al_2O_6$

Appendix F

Phase transitions upon cooling

The modelled phase transitions from FactSage upon cooling the metal and slag phase during the aluminothermic reduction on slag 2 are presented. The modelled phase transitions from the reacted slag at 1550 °C are done with Scheil-Gulliver cooling while the three other cases are done with Equilibrium cooling.

F.1 Metal phase, 1650 °C

```
SUMMARY OF REACTIONS

Cooling
1650 to 1640.17 C      (DELTA H = -4.6055E+02 J)
Liquid cooling

Constituent 1
1640.17 to 1213.41 C   (DELTA H = -3.8918E+04 J)
Liquid -> Si4Ti5_prototype_Zr5S(s)

Constituent 2
1213.41 to 1081.58 C   (DELTA H = -9.7644E+03 J)
Liquid + Si4Ti5_prototype_Zr5S(s) -> B27

Constituent 2A
1081.58 to 964.52 C    (DELTA H = -4.8359E+03 J)
Liquid -> B27

Constituent 3
964.52 to 865.74 C     (DELTA H = -7.6578E+03 J)
Liquid + B27 -> Ti7Al5Si14_Tau1(s)

Constituent 4
865.74 to 827.41 C     (DELTA H = -4.7055E+03 J)
Liquid + B27 + Ti7Al5Si14_Tau1(s) -> hP3 + Ti3Al2Si5_tau2(s)

Constituent 4A
827.41 to 727.50 C     (DELTA H = -6.6827E+03 J)
Liquid + B27 -> hP3 + Ti3Al2Si5_tau2(s)

Constituent 5
727.50 C (isothermal)  (DELTA H = -1.0228E+03 J)
Liquid + B27 + hP3 -> C15 + Ti3Al2Si5_tau2(s)

Constituent 6
727.50 to 726.72 C     (DELTA H = -1.1120E+03 J)
Liquid + B27 -> C15 + Si4Ti5_prototype_Zr5S(s) + Ti3Al2Si5_tau2(s)

Constituent 6A
726.72 C (isothermal)  (DELTA H =  1.2275E-05 J)
C15 + Ti3Al2Si5_tau2(s) -> Liquid + Si4Ti5_prototype_Zr5S(s)

Constituent 7
726.72 to 702.82 C     (DELTA H = -1.3489E+03 J)
Liquid + Si4Ti5_prototype_Zr5S(s) -> C15 + Ti3Al2Si5_tau2(s)

Constituent 8
702.82 C (isothermal)  (DELTA H = -3.8532E+03 J)
Liquid + C15 + Si4Ti5_prototype_Zr5S(s) -> D13 + Ti3Al2Si5_tau2(s)

Constituent 8A
702.82 to 700.81 C     (DELTA H = -1.0117E+02 J)
Liquid + Si4Ti5_prototype_Zr5S(s) -> D13 + Ti3Al2Si5_tau2(s)T

Constituent 9
700.81 C (isothermal)  (DELTA H = -1.1231E+03 J)
Liquid + Si4Ti5_prototype_Zr5S(s) -> D022 + D13 + Ti3Al2Si5_tau2(s)
```

Figure F.1: Cooling of the metal from 1650 °C.

F.2 Slag phase, 1650 °C

```
SUMMARY OF REACTIONS

Cooling
1650 to 1650.00 C      (DELTA H = -1.4818E-04 J)
Slag-liq cooling

Constituent 1
1650.00 to 1647.00 C   (DELTA H = -3.6101E+02 J)
Slag-liq -> Liquid

Constituent 2
1647.00 to 1456.59 C   (DELTA H = -2.2822E+04 J)
Slag-liq -> Si4Ti5_prototype_Zr5Si(s)

Constituent 3
1456.59 to 1361.25 C   (DELTA H = -1.8126E+04 J)
Slag-liq -> Si4Ti5_prototype_Zr5Si(s) + CaAl2O4_solid(s)

Constituent 4
1361.25 to 1359.37 C   (DELTA H = -1.4291E+04 J)
Slag-liq -> Si4Ti5_prototype_Zr5Si(s) + CaAl2O4_solid(s) + Ca3Al2O6_solid(s)

Constituent 5
1359.37 to 1306.68 C   (DELTA H = -1.3049E+04 J)
Slag-liq -> Ca3Ti2O7-Ca3Ti2O6 + CaAl2O4_solid(s) + Ca3Al2O6_solid(s)

Constituent 6
1306.68 to 1282.19 C   (DELTA H = -2.9820E+03 J)
Slag-liq -> Ca3Ti2O7-Ca3Ti2O6 + CaAl2O4_solid(s) + Ca3Al2O6_solid(s) + Ca2SiO4_Alpha-prime(s2)

Constituent 7
1282.19 C (isothermal) (DELTA H = -3.5292E+00 J)
Slag-liq -> Ca3Ti2O7-Ca3Ti2O6 + CaAl2O4_solid(s) + Ca3Al2O6_solid(s) + Ca2SiO4_Alpha-prime(s2) + Ca3Ti2O7_solid(s)
```

Figure F.2: Cooling of the slag from 1650 °C.

F.3 Metal phase, 1550 °C

```
SUMMARY OF REACTIONS

Cooling
1650 to 1640.17 C      (DELTA H = -4.6055E+02 J)
Liquid cooling

Constituent 1
1640.17 to 1213.41 C   (DELTA H = -3.8918E+04 J)
Liquid -> Si4Ti5_prototype_Zr5S(s)

Constituent 2
1213.41 to 1081.58 C   (DELTA H = -9.7644E+03 J)
Liquid + Si4Ti5_prototype_Zr5S(s) -> B27

Constituent 2A
1081.58 to 964.52 C    (DELTA H = -4.8359E+03 J)
Liquid -> B27

Constituent 3
964.52 to 865.74 C     (DELTA H = -7.6578E+03 J)
Liquid + B27 -> Ti7Al5Si14_Tau1(s)

Constituent 4
865.74 to 827.41 C     (DELTA H = -4.7055E+03 J)
Liquid + B27 + Ti7Al5Si14_Tau1(s) -> hP3 + Ti3Al2Si5_tau2(s)

Constituent 4A
827.41 to 727.50 C     (DELTA H = -6.6827E+03 J)
Liquid + B27 -> hP3 + Ti3Al2Si5_tau2(s)

Constituent 5
727.50 C (isothermal)  (DELTA H = -1.0228E+03 J)
Liquid + B27 + hP3 -> C15 + Ti3Al2Si5_tau2(s)

Constituent 6
727.50 to 726.72 C     (DELTA H = -1.1120E+03 J)
Liquid + B27 -> C15 + Si4Ti5_prototype_Zr5S(s) + Ti3Al2Si5_tau2(s)

Constituent 6A
726.72 C (isothermal)  (DELTA H =  1.2275E-05 J)
C15 + Ti3Al2Si5_tau2(s) -> Liquid + Si4Ti5_prototype_Zr5S(s)

Constituent 7
726.72 to 702.82 C     (DELTA H = -1.3489E+03 J)
Liquid + Si4Ti5_prototype_Zr5S(s) -> C15 + Ti3Al2Si5_tau2(s)

Constituent 8
702.82 C (isothermal)  (DELTA H = -3.8532E+03 J)
Liquid + C15 + Si4Ti5_prototype_Zr5S(s) -> D13 + Ti3Al2Si5_tau2(s)

Constituent 8A
702.82 to 700.81 C     (DELTA H = -1.0117E+02 J)
Liquid + Si4Ti5_prototype_Zr5S(s) -> D13 + Ti3Al2Si5_tau2(s)

Constituent 9
700.81 C (isothermal)  (DELTA H = -1.1231E+03 J)
Liquid + Si4Ti5_prototype_Zr5S(s) -> D022 + D13 + Ti3Al2Si5_tau2(s)
```

Figure F.3: Cooling of the metal from 1550 °C.

F.4 Slag, phase, 1550 °C

```
SUMMARY OF REACTIONS

Cooling
1550 to 1550.00 C      (DELTA H =  1.3585E-06 J)
Slag-liq cooling

Constituent 1
1550.00 C (isothermal) (DELTA H =  1.3585E-06 J)
Slag-liq -> Si4Ti5_prototype_Zr5S(s)

Constituent 2
1550.00 to 1512.95 C   (DELTA H = -2.3573E+03 J)
Slag-liq -> Si4Ti5_prototype_Zr5S(s) + CaAl2O4_solid(s)

Constituent 3
1512.95 to 1361.66 C   (DELTA H = -5.2644E+03 J)
Slag-liq -> D88 + CaAl2O4_solid(s)

Constituent 4
1361.66 to 1360.29 C   (DELTA H = -1.7529E+03 J)
Slag-liq -> D88 + CaAl2O4_solid(s) + Ca3Al2O6_solid(s)

Constituent 5
1360.29 to 1282.22 C   (DELTA H = -2.4448E+03 J)
Slag-liq -> Ca3Ti2O7-Ca3Ti2O6 + CaAl2O4_solid(s) + Ca3Al2O6_solid(s)

Constituent 6
1282.22 to 1282.19 C   (DELTA H = -1.8869E+00 J)
Slag-liq -> Ca3Ti2O7-Ca3Ti2O6 + CaAl2O4_solid(s) + Ca3Al2O6_solid(s) + Ca2SiO4_Alpha-prime(s2)

Constituent 7
1282.19 C (isothermal) (DELTA H = -5.0562E+00 J)
Slag-liq -> Ca3Ti2O7-Ca3Ti2O6 + CaAl2O4_solid(s) + Ca3Al2O6_solid(s) + Ca2SiO4_Alpha-prime(s2) + Ca3Ti2O7_solid(s)
```

Figure F.4: Cooling of the slag from 1550 °C.

Inger Fygle

Production of Titanium alloys via aluminothermic reduction

NTNU
Norwegian University of
Science and Technology